Characterization and comparison of weaving printing patterns in wire arc additive manufacturing of austenitic stainless steel 316L

Master Thesis

by

Ho-Yu Cheung

Submitted in partial fulfilment of the requirements for the degree of

Master of Science in Materials Science and Engineering

at the Delft University of Technology

Student number:	5850509
Supervisors:	Associate Prof. Dr.ir. Marcel Hermans
	Dr. Amin Ebrahimi, postdoctoral researcher
Thesis committee:	Associate Prof. Dr.ir. Marcel Hermans
	Associate Prof. Dr. Vera Popovich
	Assistant Prof. Dr. T. (Trayana) Tankova
	Dr. Amin Ebrahimi, postdoctoral researcher

TU Delft Delft University of Technology

Acknowledgment

I would like to express my gratitude to my project supervisors Professor Marcel Hermans and Dr. Amin Ebrahimi for their guidance throughout the project. They have provided directions and insights whenever I encounter difficulties. Their feedback on planning, experimentation, documentation, writing, and presentation of the project has led to my improvement in research and academic writing.

I am also appreciative to Remko Seijffer for teaching me the operation of all the lab equipment, as well as being reliable by helping me whenever there is any problem during the experiments. Through his experience with processes and equipment, I have gained practical skills. I am also thankful to Arjun Sood for giving me advice and helping me with the characterization of my samples.

My sincere thanks to Professor Constantinos Goulas at the University of Twente for his time and effort in providing the processing of all my tensile samples. Thanks to Richard Huizenga for helping me conduct X-ray diffraction, and Kees Kwakernaak for helping me to conduct electron beam backscatter diffraction on my samples. Both experiments have provided significant information and played an integral role in this project. They have also provided great input to aid me with data analysis.

Also, a thank you to my colleagues who shared the WAAM lab with me. They have provided me with support and company throughout this project. Finally, I am grateful to my family and friends who showed trust in me and supported me through hardship.

Abstract

Printing patterns in additive manufacturing have been extensively studied regarding their effects on the microstructure and mechanical properties of the materials. However, weaving, a welding technique that produces good quality welds in large areas and ensures good weld penetration has not been applied in additive manufacturing. This study focuses on comparing four weaving patterns to two traditional line printing patterns in Wire arc additive manufacturing of austenitic stainless steel 316L. This thesis covers the groundwork of weaving pattern characterization, starting from optimization of printing parameters and printing path, followed by pattern characterization through measurements of voltage, current, thermal history, and thermal profile, and investigation of surface quality of the samples. Microstructure characterization was then conducted by optical microscopy, electron backscatter diffraction, and X-ray diffraction; and mechanical properties were obtained through microhardness and tensile testing. The weaving patterns showed an improved deposition rate and avoided lack-of-fusion defects compared to the line printing patterns. Two out of four weaving patterns achieved superior surface quality over the line printing patterns and are free of macro-defects such as side wall collapse and spattering. The weaving patterns have excessive heat accumulation and lower cooling rates compared to line printing patterns, which led to coarser microstructures and inferior microhardness and tensile properties. The thermal gradient is also more uniformed and aligned to the build direction, increasing the degree of grain alignment and texture of the weaving patterns across the samples.

Contents

List of figures

List of tables

1 Introduction

Additive manufacturing of metal has been under development for over 30 years since the first selective laser sintering system was developed in 1992 [1,2]. The importance of additive manufacturing in the industry has evolved from a tool for rapid prototyping to a favorable manufacturing method of highly complex parts across a wide range of sizes. Additive manufacturing also offers numerous advantages over conventional materials processing techniques. It facilitates the production of components with complex designs that cannot be manufactured by conventional methods. It also offers design flexibility, which can, for instance, lead to minimizing joining elements and reducing weight, stress concentration, and assembly time. Its principle of material deposition results in little material waste compared to conventional subtractive manufacturing methods. Additionally, additive manufacturing apparatuses generally function as universal systems, making them particularly suited for rapid prototyping and repair applications.

Wire-arc additive manufacturing (WAAM) especially excels at deposition rate, typically ranging from 5–6 kg/h, while other techniques such as selective laser melting (SLM) only have a deposition rate of about 0.1 kg/h [3]. WAAM combines arc welding with a wire feed system to continuously melt and deposit material. Materials commonly used in WAAM are titanium alloys, nickel-based superalloys, aluminum alloys, and steels [1]. Steel, specifically austenitic stainless steel 316L is the most accessible engineering material, making its cost relatively low [1], which is suitable for the large deposition rate of WAAM.

Additive manufacturing processes often have many processing parameters to be adjusted to influence the microstructure and mechanical properties of the material, such as heat input, travel speed, dwell time, and printing pattern. Changing one or combinations of these processing parameters would affect the thermal history experienced by the material, resulting in different microstructures and mechanical properties [4]. Among the array of process parameters, the alteration of printing patterns is particularly attracting as it does not directly impact the heat input from the power source. Nonetheless, it significantly influences the material's microstructure and mechanical properties by modulating the thermal profile [5].

Weaving is a welding technique that produces good quality welds in large areas and ensures good weld penetration throughout the weld bead, and the same principle can be applied to WAAM as printing patterns. This technique complements the high deposition rate in WAAM, depositing weld beads in a large area continuously, unlike in traditional line printing where printing pauses between each line. Large coverage and uniform penetration can also potentially avoid typical lack-of-fusion defects in WAAM. However, studies regarding weaving patterns are limited, and the effect of the complex printing paths of weaving patterns on the microstructure and mechanical properties of the materials requires further study before it is implemented into WAAM.

This thesis aims to investigate the weaving patterns in WAAM. The characteristics of weaving patterns and the effects of weaving patterns on microstructure and mechanical properties of WAAM of 316L are studied. The structure of this thesis is as follows: In Chapter 2 literature review on the general characteristics of materials processed by WAAM and the effect of various printing patterns on microstructure and mechanical properties is conducted, to identify the research gap in current research and formulate research questions and goals for this thesis. Chapter 3 then discusses the optimization of the weaving patterns, the printing process of the WAAM blocks, and sample preparation for characterization. This is followed by a discussion on characteristics of the weaving patterns through in-situ measurements and evaluation of surface quality and substrate distortion through 3D scanning in Chapter 4. Chapter 5 discusses microstructural characterization of the WAAM blocks through optical microscopy, electron backscatter diffraction (EBSD), and X-ray diffraction (XRD), and Chapter 6 discusses mechanical properties through results obtained from hardness and tensile testing. Finally, all the results from previous Chapters are evaluated and discussed in Chapter 7, followed by a conclusion in Chapter 8 and recommendations for future research in Chapter 9.

2 Literature review

To better understand the effect of printing patterns in WAAM and to identify the current research gap, a literature review is conducted on state-of-the-art research regarding the characteristics of the WAAM process and the effect of printing patterns on microstructure and mechanical properties. After the literature review, a clear direction and methodology for conducting research is obtained.

2.1 Wire arc additive manufacturing (WAAM)

WAAM is an additive manufacturing technique in direct energy deposition (DED), based on arc welding techniques where parts are fabricated from CAD data in a layer-by-layer fashion. Arc welding technique, typically in the form of gas tungsten arc welding (GTAW), gas metal arc welding (GMAW), or plasma arc welding (PAW) is applied onto a metal wire feeding through the nozzle. The material is then fused and deposited onto the substrate, forming a melt pool, then solidifies. This process excels in deposition rate but lacks dimension accuracy, features that are too small cannot be printed properly and the surface roughness of the part is relatively poor, which eventually needs post-process machining [6]. Figure 1 depicts the working principle of WAAM, and

Table 1 shows the processing parameters of WAAM.

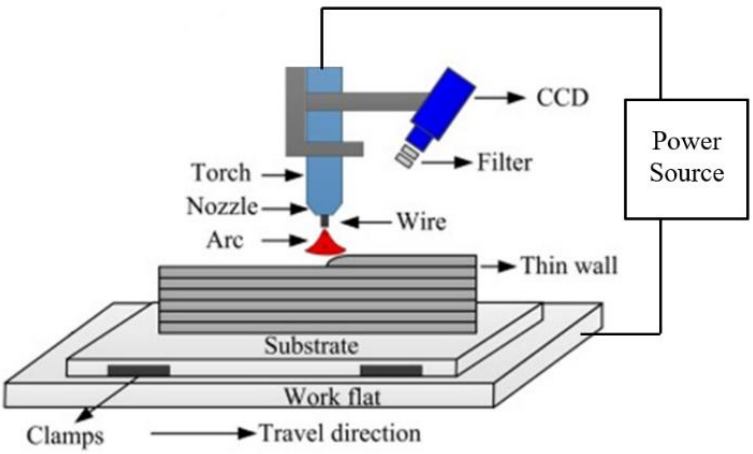

Figure 1. Schematic diagram of WAAM, modified from [4].

WAAM excels in large structural components due to its deposition rate (up to 10 kg/h for steel [7]) and relatively low cost. WAAM is used to create a preliminary shape to be machined to the final part, which reduces material usage, material waste, and lead time compared to machining a large

block of material directly. Currently, WAAM of stainless steel is used in high-temperature applications that also require corrosion resistance, such as in chemical and nuclear plants [5]. RAMLAB has also used WAAM to print the ship's propellers and water bushings for Total's EIG Elgin-Franklin rig with WAAM, as well as for repair applications [8].

Same as arc welding, WAAM has techniques that vary in energy source. GTAW, GMAW, and PAW-based WAAM vary slightly in terms of components, stability, and deposition rate. PAW and GMAW-based WAAM are about twice the deposition rate of GTAW-based WAAM, and GMAW can double the deposition rate by adding an additional electrode. However, GMAW has relatively poorer arc stability compared to GTAW and PAW [9]. Table 2 summarizes the features and benefits of different WAAM energy sources.

WAAM has good energy efficiency when compared to other techniques in the DED category that employ different energy sources. An arc-based power source has about 90% energy efficiency, an electron beam has a lower energy efficiency, while a laser-based power source has the lowest energy efficiency at around 30% to 50% [3,10].

Without proper configuration of process parameters, defects including distortion, hot and cold cracking, delamination, and porosity can occur [9]. These defects cause a decrease in mechanical performance. Common causes of defects are improper printing patterns, inappropriate process parameters, gas contamination, and an uncontrolled thermal cycle [9].

Table 1. Process overview of WAAM, modified from [4].

Process	**WAAM**
Feedstock	Wire
Heat source	Electric arc
Nomenclature	DED-PA/DED-GMA/DED-GTA
Power (W)	1000–3000
Speed (mm/s)	5–15
Max. feed rate (g/s)	0.2–2.8
Max. build size (mm x mm x mm)	5000 x 3000 x 1000
Production time	Low
Dimensional accuracy	Intricate features are not possible
Surface roughness	Needs machining
Post-processing	Machining is essential to producing the final parts
References	[7,11–13]

Table 2. Features and energy sources of different WAAM techniques [9].

WAAM	Energy source	Features	Ref.
GTAW-based	GTAW	Non-consumable electrode; Separate wire feed process; Typical deposition rate: 1-2 kg/hour; Wire and torch rotation are needed;	[14]
GMAW-based	GMAW	Consumable wire electrode; Typical deposition rate 3-4 kg/hour; Poor arc stability, spatter;	
	CMT	Reciprocating consumable wire electrode; Typical deposition rate: 2-3 kg/hour;	
	CMT	Low heat input process with zero spatter, high process tolerance;	[12]
	Tandem GMAW	Two consumable wires electrodes; Typical deposition: 6-8 kg/hour; Easy mixing to control composition for intermetallic materials manufacturing;	
PAW-based	Plasma	Non-consumable electrode; Separate wire feed process; Typical deposition rate 2-4 kg/hour; Wire and torch rotation are needed;	[15]

Similar to welding, WAAM suffers thermal distortion due to residual stress from the localized expansion and contraction due to the material's coefficient of thermal expansion under thermal cycles [9]. Due to the clamping of the part and the substrate, residual stress accumulates and is redistributed in the form of thermal distortion after unclamping, leading to shrinkage and bending of the part [16]. Aside from distortion, residual stress also affects the mechanical properties and fatigue performance of the part [16]. Steels are susceptible to thermal distortion and process parameters should be carefully considered [9]. Process parameters that affect thermal distortion and residual stress are arc current and voltage, wire feeding speed, ambient temperature, and supply of shielding gas [9]. Heat treatment after printing can reduce residual stresses, to facilitate redistribution of residual stress by thermal activation [9]. Interpass cold rolling, a technique to plastically deform each deposition layer by rolling also reduces and redistributes residual stress in a tensile direction by inducing recrystallization, reducing thermal distortion and anisotropy, and enhancing the yield strength and ultimate tensile strength of the material [17].

Porosity is usually more common in aluminum alloys than steels and is caused by gas or surface contamination, and low solubility of hydrogen after solidification [9]. This defect causes a decrease in mechanical performance by acting as a site for microcrack initiation [9]. Preventions for this defect are cleaning the substrate surface, using high quality and quantity of shielding gas, and interpass cold rolling, which increases dislocation density and provides a diffusion path for entrapped hydrogen [18].

Hot cracking, or solidification cracking in WAAM occurs during the last stage of solidification [19]. It occurs when shrinkage is present and occurs when shrinkage is present and the internal stresses exceed the strength of the material, which is lowered at higher temperatures [9]. This is caused by insufficient weld penetration due to high strain in the melt pool, low supply of liquid metal, and low melting point impurities, and can be prevented by reducing cooling rate, heat input, and residual stress [19]. This issue is detrimental since steel is susceptible to it and cracks cannot be repaired by post-processing [9].

Delamination is the lack-of-fusion of material in each deposition layer. This is caused by low heat input, resulting in insufficient melting and remelting of material between layers. Residual stress and impurities also affect delamination [20]. The most effective way to reduce the risk of delamination is to reduce residual stress and increase heat input. Although steel has a relatively lower risk of delamination compared to other materials [16], this issue should not be underestimated since it also cannot be repaired by post-processing [9].

Balling and humping are defects that reduce surface quality. The balling defect is when a droplet of molten material cannot join the melt pool, but forms its spherical bead on the deposition surface [21]. This happens when the heat input is too low, which reduces the melt pool size and increases the difficulty for the droplet of molten material to combine with the melt pool. Conversely, high travel speed can cause a humping phenomenon, which is the periodic undulation of the weld bead, reducing surface quality and affecting the stability of the subsequent depositions [22]. The high vapor recoil pressure vertical to the melt pool thins the melt pool and increases its free surface, causing a periodic shrinking effect [23]. Balling and humping phenomena are caused by melt pool instability and their range of travel speed and power, and appearance are shown in Figure 2. Note that the travel speed and power are associated with SLM, but the same principle with different

values can be applied to WAAM. A thorough understanding of the effects of heat input, melt pool dynamics, and printing patterns is required to prevent these defects.

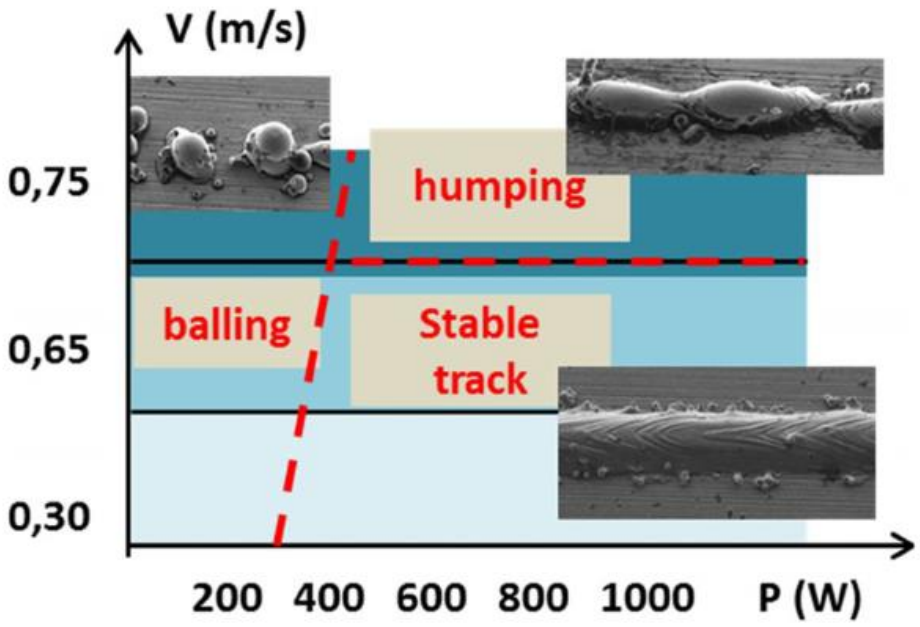

Figure 2. Balling and humping phenomenon and their zones of instability in SLM [23].

2.2 Austenitic stainless steel

To understand the effect of process parameters and printing patterns on the material, it is important to first understand the material and its interactions with the process. This section discusses the chemical composition, solidification mechanism, grain structure and texture in additive manufacturing, and the resulting mechanical properties from the microstructural features.

The most commonly applied austenitic stainless steels are 316L or 304L [24], which have a high chromium and nickel content and offer excellent corrosion resistance. This review focuses on the more commonly studied 316L [24]. 316L produced by DED consists of an austenite matrix and a small amount of fine δ-ferrite films at the solidification cells [25], which agrees with the Schaeffler diagram in Figure 3. The austenite matrix is due to the presence of austenite stabilizing elements namely nickel and manganese, while the fine δ-ferrite films are due to micro-segregation of ferrite stabilizing elements in particular chromium and molybdenum during solidification [24]. A sufficiently slow cooling rate allows these elements to segregate to sub-grain boundaries in austenite grains, forming ferrite films locally [25].

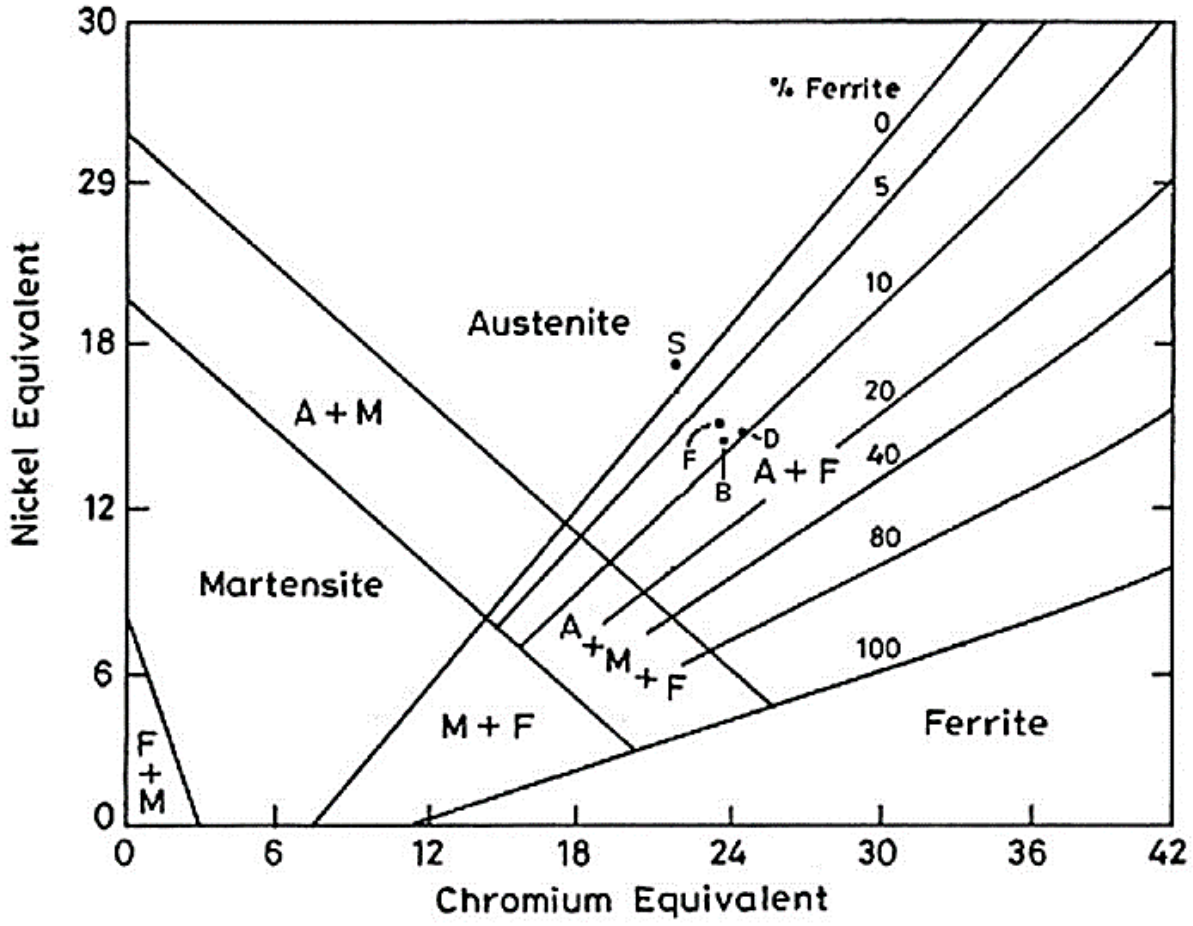

Figure 3. Schaeffler diagram of steel [25,26].

2.2.1 Solidification and thermal history

As mentioned above austenitic stainless steels usually have an austenite matrix with fine ferrite films. The volume fraction of ferrite in weld impacts the quality of the weld, which would be important in WAAM as well. More than 10 vol% of fine δ-ferrite films reduce ductility, toughness, and corrosion resistance, whereas less than 5 vol% would result in solidification cracking[27]. The solidification morphology and post-solidification phase transformation depend on the nickel and chromium content and can be predicted in Figure 4. For 316L, the composition intercepts the left side of the three-phase eutectic triangle, where the austenite matrix first solidifies and interdendritic ferrite is formed at the end of solidification.

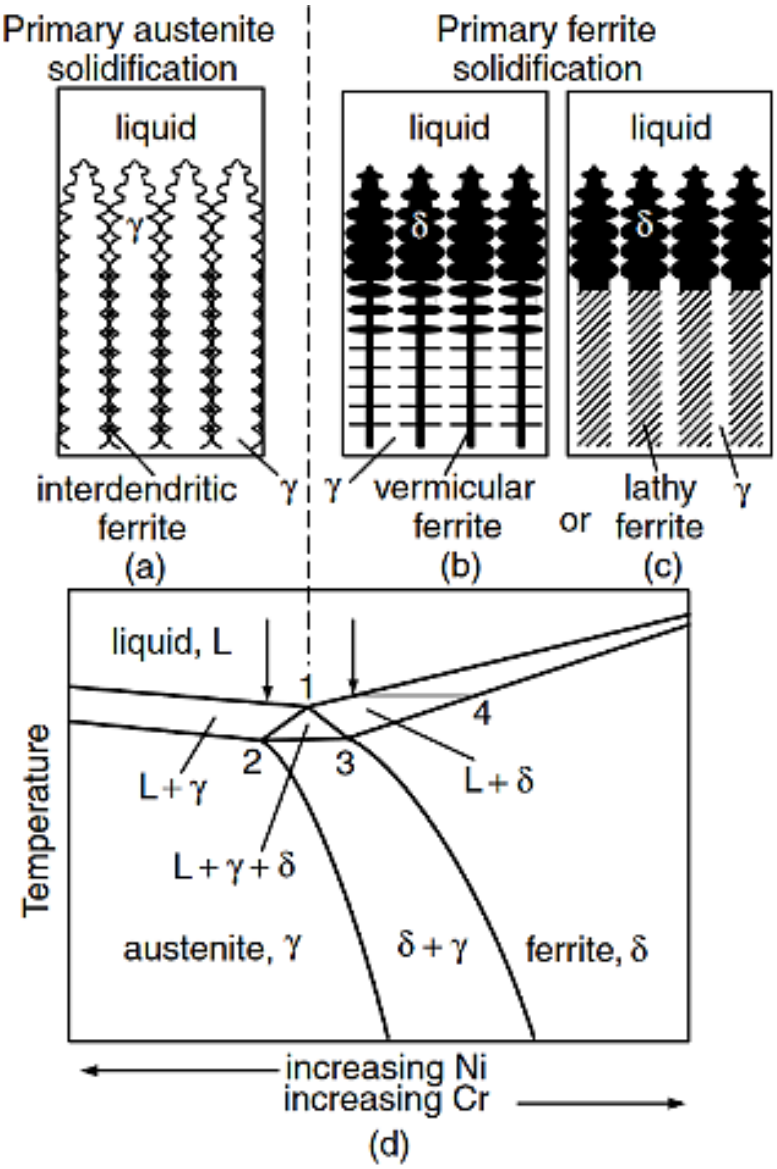

Figure 4. Pseudo-binary phase diagram of austenitic stainless steel depicting solidification morphology based on Ni and Cr composition; (a) primary austenite solidification with interdendritic ferrite, which is the case for 316L; (b) primary ferrite solidification as vermicular ferrite; (c) primary ferrite solidification as lathy ferrite [27].

The morphology of the austenite matrix depends on the temperature gradient and growth rate. Due to heat accumulation when each layer is deposited, there is anisotropy in microstructure across the deposition layers [28]. The cooling rate is reduced when more layers are deposited, and more heat accumulates from the previous layers. The thermal history also affects previous layers, where the lower layers are repeatedly heated by the newly deposited layer, inducing recrystallization and diffusion of alloying elements [4]. A typical thermal history of a single point during WAAM is shown in Figure 5. For other materials such as high strength low alloy steel (HSLA), the reheated

effect from thermal history can even induce repeated phase transformation from austenite to ferrite, bainite, and martensite [28]. For 316L, the effect of thermal history on solidification in deposition layers is discussed below.

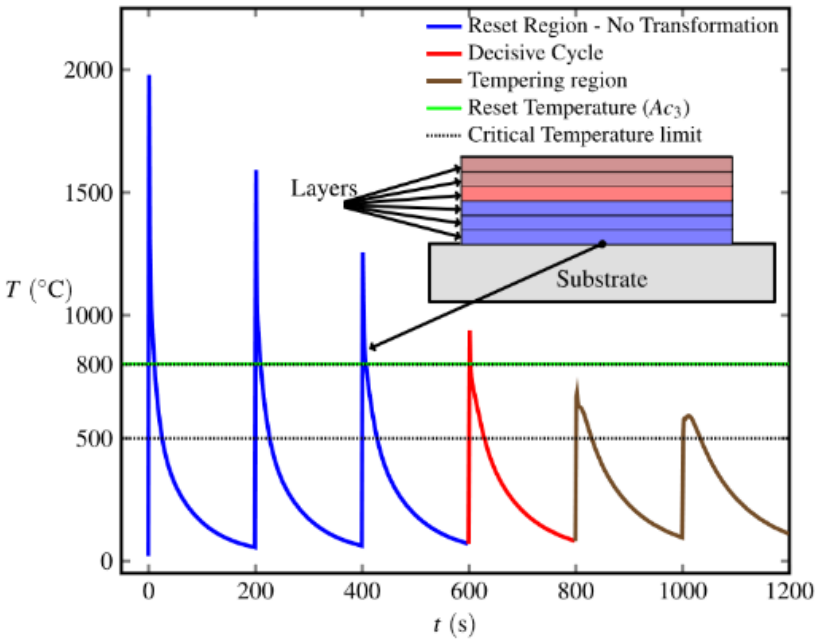

Figure 5. Thermal history of the first deposition layer when it is reheated repeatedly by subsequent deposition layers [28].

Park *et al*. [29] modeled the solidification morphology of cold metal transfer (CMT) based WAAM and investigated the relation between temperature gradient (G) and growth rate (R). They verified the model with an experiment of measuring the temperature profile of a 10-layer rectangular sample. For the first 5 layers, the austenite matrix is columnar dendritic and the fine ferrite films are in the form of lathy ferrite and skeletal ferrite. In the first deposition layer, G and R are the highest, due to the layer being directly deposited onto the cold substrate. The relatively high cooling rate (G × R) results in columnar dendrites. When the next layer is deposited, on the surface of the melt pool G is low and R is high, which would result in equiaxed dendrites. However, the equiaxed dendrites are remelted by the subsequent deposition layer and the columnar dendrite from the first layer continues to grow epitaxially. This explains why only the 10^{th} layer is in the form of equiaxed dendrite, since it has a low G and a high R, and experiences no remelting. The microstructure and solidification map of the layers are shown in Figure 6. The authors also explained the prediction of microstructure size in relation to G × R. A fine microstructure is formed

with high G × R, which becomes coarser as G × R decreases, hence a reduction in mechanical properties. The size of the microstructure was estimated by the secondary dendrite arm spacing (SDAS), which increased from the 1st to the 9th layer. Other literature has found similar results [30–32].

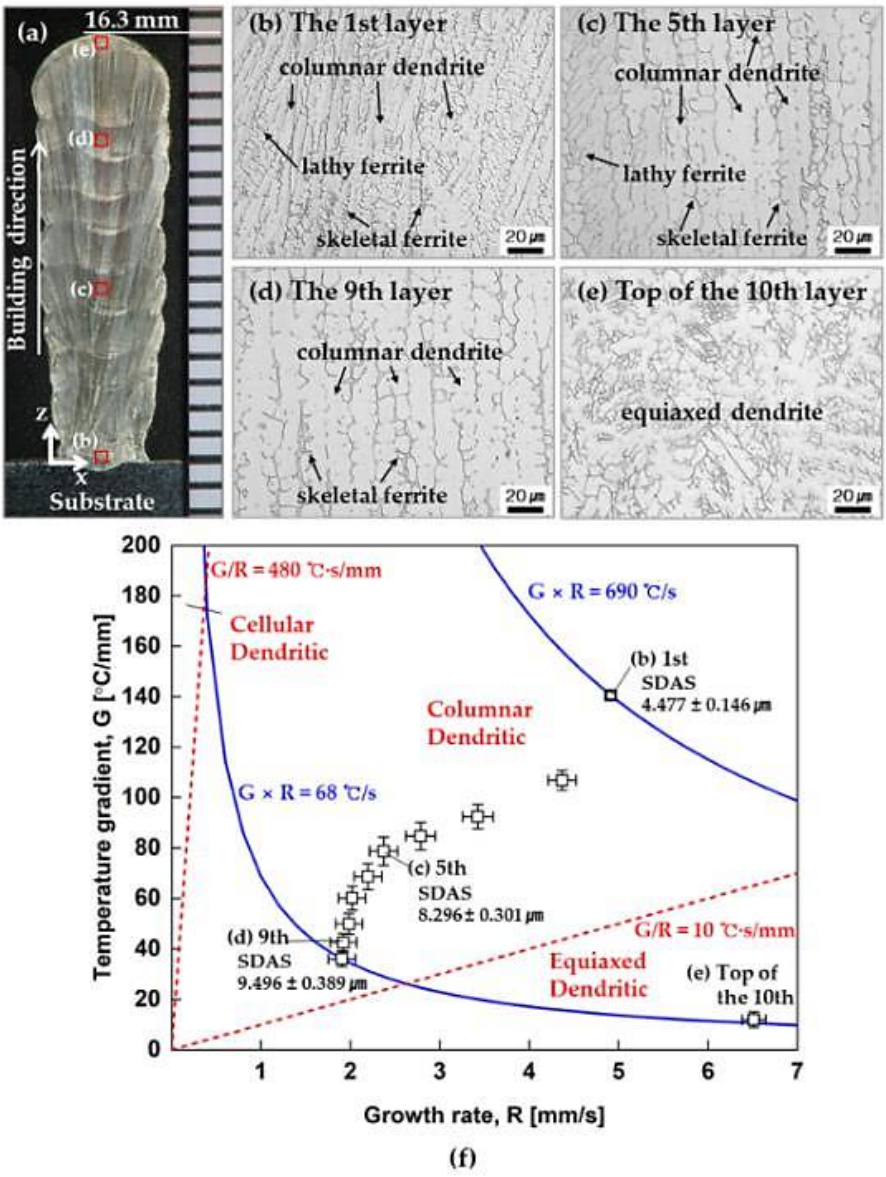

(f)

Figure 6. Solidification map of 316L produced by CMT-WAAM and optical microscopy images of deposition layers; (a) cross-section of the sample; (b) cross-section of 1st layer with morphology labeled; (c) 5th layer (d) 9th layer (e) 10th layer (f) solidification map [29].

The G and R values greatly depend on the process. A combined solidification map of WAAM, DED, and SLM in Figure 7 shows that WAAM's G and R are the lowest out of the three processes, while for SLM the G and R are in a much higher order of magnitude.

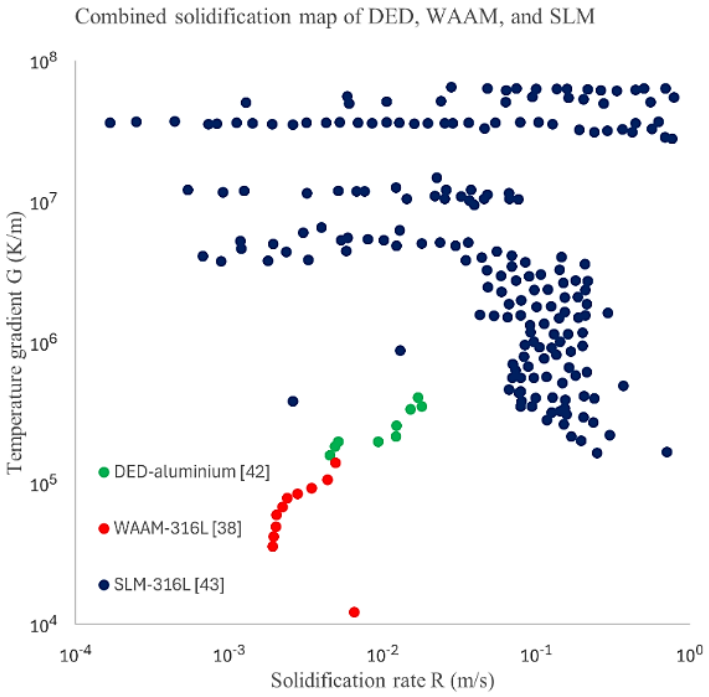

Figure 7. Solidification map of WAAM of 316L [29], DED of aluminum [33], and SLM of 316L [34].

2.2.2 Grain structure and texture

The grain growth direction of 316L in WAAM is highly oriented. Belotti *et al*. [35] investigated the microstructure of thick-walled WAAM manufactured parts, and they found large columnar grains are elongated in the build direction due to the preferential growth direction in the direction of highest heat extraction to the substrate and the surface. Figure 8 shows a cross-section of a WAAM-produced part showing columnar grains aligned perpendicular to the fusion boundaries, indicated with dashed lines. These fusion zones are crescent-shaped, indicating penetration of the fusion zone into previous layers due to remelting.

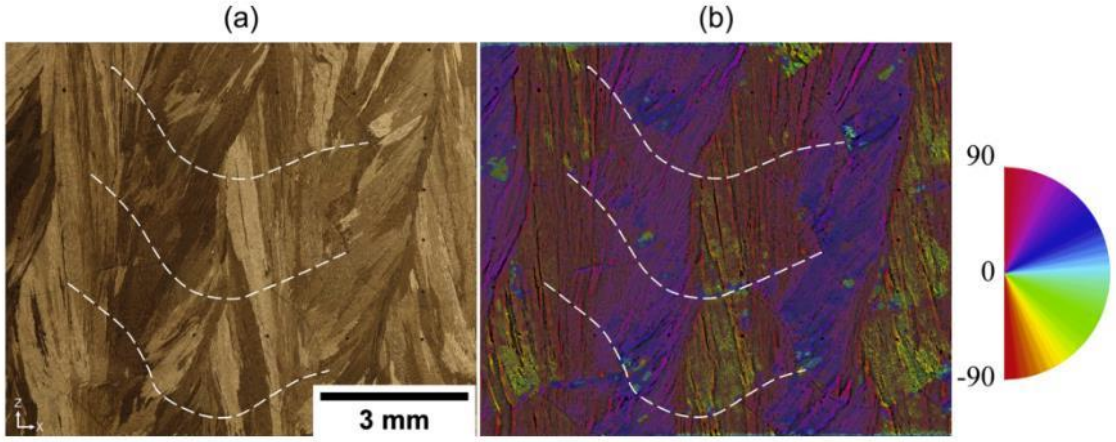

Figure 8. Cross section of WAAM produced 316L showing highly aligned elongated columnar grains and fusion zone boundaries: (a) optical micrograph of cross-section; (b) local angular map showing grain growth directions. [35]

In terms of texture, 316L has a strong texture of <100> in the build direction [24,36–38]. Solidification of face-centered cubic (FCC) structure has a preferred direction of <100> due to anisotropy of surface energy in the nucleation interface and atomic bond energy in specific crystallographic planes, leading to the formation of dendrites with dendrite trunks growing in any equivalent <100> directions and dendrite arms growing in the conjugate <100> directions [36]. Belotti *et al*. [35] also studied the texture of the thick-walled part, and strong <100> texture is found in both YZ (deposition-building direction) and XZ (traverse-building cross-section), which is due to the preferred growth direction aligning with the direction of the highest temperature gradient [24,31,35,39]. The YZ plane showed the strongest <100> texture, especially in overlapping fusion zones, while in the center of the fusion zone, the texture is not as prominent, and the grains are not as elongated. The <100> direction is also rotated by about 30° at the edges due to the rotation of temperature gradient direction, further supporting the correlation of temperature gradient direction and grain growth and texture direction.

2.2.3 Mechanical properties

316L produced by additive manufacturing shows a wide range of tensile properties depending on process parameters and has comparable yield strength and ultimate tensile strength compared to those produced by traditional processes, as shown in Table 3. Wang *et al*. [40] suggested that the increased strength originates from the hierarchical structure of the material, with various microstructural features ranging 6 orders of magnitude in length scale all contributing to strength.

The combined effect of grain refinement, solidification structure, high angle grain boundaries (HAGB), intercellular segregation of nanoprecipitates, and dislocations all contribute to the increased strength. They also showed that the Hall-Petch relation applies to the subgrain length scale. In terms of elongation, the authors showed that the laser powder bed fusion produced samples have a higher uniform elongation (36% and 59% engineering strain to failure) compared to their traditionally processed counterparts (30% and 43% engineering strain to failure), due to the steady and progressive work hardening mechanism from the hierarchically heterogeneous microstructure, and twinning mechanism from segregation of alloying element to intercellular regions and low-angle grain boundaries.

Other literature also explains the effect of grain refinement through the Hall-Petch relation, which shows that yield strength is inversely related to grain size and finer microstructures leading to increased tensile strength [40–44]. For DED however, elongation to failure tends to be worse than the parts produced by traditional processes, due to grain refinement and solidification structure causing dislocations to pile up, as well as the presence of stress concentrations at sharp-edged lack-of-fusion defects[4,45]. Table 3 summarizes the yield strength, ultimate tensile strength, and elongation to failure from the literature. Note that transversal indicates that the tensile sample is made parallel to the building direction, while longitudinal indicates that the tensile sample is made parallel to the printing direction.

In DED, yield strength and ultimate tensile strength are a function of linear heat input, reducing linear heat input reduces melt pool size and increases thermal gradient and cooling rate, producing a finer microstructure [5,47]. In terms of anisotropy, due to the alignment of grain growth direction and solidification substructures, 316L has on average 18% higher yield strength and 9.4% higher ultimate tensile strength in the longitudinal direction than the transverse direction in Table 3. Figure 9 shows the yield strength, ultimate tensile strength, and elongation in the longitudinal and transverse directions.

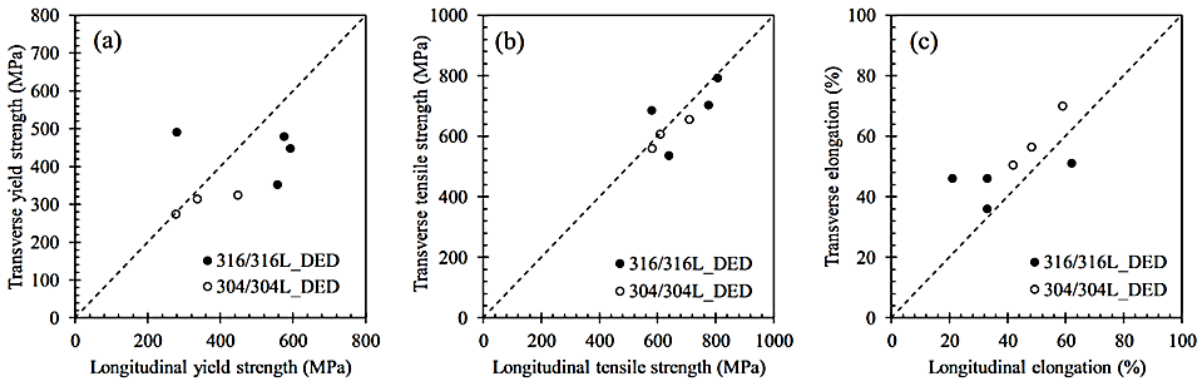

Figure 9. Mechanical properties of austenitic stainless steels produced by DED: (a) yield strength; (b) ultimate tensile strength; (c) elongation [4].

Table 3. Tensile properties of austenitic stainless steel in various additive manufacturing processes compared to wrought material.

Process	Material	Laser power (W)	Travel speed (mm/s)	Direction*	Yield strength (MPa)	Tensile strength (MPa)	Young's modulus (GPa)	Elongation to failure (%)	Reference
SLM	316L	300	1000	T	-	590	-	21.1	[31]
SLM	316L	275	700	T	346 ± 17	639 ± 4	-	94 ± 2	[46]
SLM	316L	90	1000	L	511.6 ± 14	621.7 ± 12	-	20.4 ± 3	[39]
				T	430.4 ± 11	509 ± 3	-	12.4 ± 1	
SLM	316L	-	-	L	609 ± 43	681 ± 7	167 ± 12	-	[47]
				T	490 ± 2	612 ± 2	152 ± 7	-	
WLAM	316L	-	-	L	438 ± 40	629 ± 7	172 ± 12	-	
				T	322 ± 2	564 ± 9	170 ± 10	-	
WLAM	304L	2300	8.5	L	337 ± 29	609 ± 18	-	48.2 ± 2.5	[45]
				T	314 ± 6	606 ± 13	-	56.4 ± 5.8	
		4000	10.6	L	277 ± 27	581 ± 20	-	41.8 ± 3.5	

				T	274 ± 7	560 ± 12	-	50.5 ± 6.7	
WAAM	316L	800	220	T	373 ± 20	630 ± 30	-	52 ± 3	[46]
SpeedPulse WAAM	316L	2984	10	T	418.0	550 ± 6	-	-	[43]
SpeedArc WAAM	316L	2730	10	T	417.9	553 ± 2	-	-	
Hot/cold rolled	316L	-	-	R	313 ± 24	584 ± 14	-	71 ± 5	[46]

* T, L, and R indicate Transversal, Longitudinal, and Rolling directions, respectively.

2.2.4 Fracture toughness

Additive manufacturing processed 316L has comparable fatigue strength to wrought processed 316L. Kumar *et al*. [46] investigated the mechanisms behind the difference in fracture toughness between WAAM, SLM, and wrought processed 316L. It was found that SLM produced a sample with the highest fracture toughness J_{IC} (202 Nmm^{-2}), while the WAAM sample has a fracture toughness of 160 Nmm^{-2} and the wrought sample has a fracture toughness of 153 Nmm^{-2}. The authors explained that SLM's increased fracture toughness is due to the high amount of deformation twins, and SLM has the highest twinning probability out of the three samples. These deformation twins are formed around the crack tip, hindering crack propagation. The presence of twins instead of martensite also contributed to an increase in fracture toughness, since the preferred crack nucleation sites at the phase boundaries are avoided [48]. WAAM however has a lower fracture toughness, and cracks are formed at the austenite/δ-ferrite interphase. These phases along the crack are also highly distorted, suggesting crack propagation due to the decohesion of phase boundaries [46].

Anisotropy is present in WAAM-processed 316L. When the load is in the grain growth direction, the crack propagates perpendicular to the grain growth direction, which has a finer microstructure due to the direction of the grain elongation. Combined with the fine cellular solidification substructure, the crack path becomes convoluted, and the crack growth is slowed [39]. When the load direction is perpendicular to the grain growth direction, however, the crack can propagate along the elongated grain boundaries, without much hindrance [39]. Figure 10 shows the difference in the crack path when loaded parallel and perpendicular to the grain growth direction.

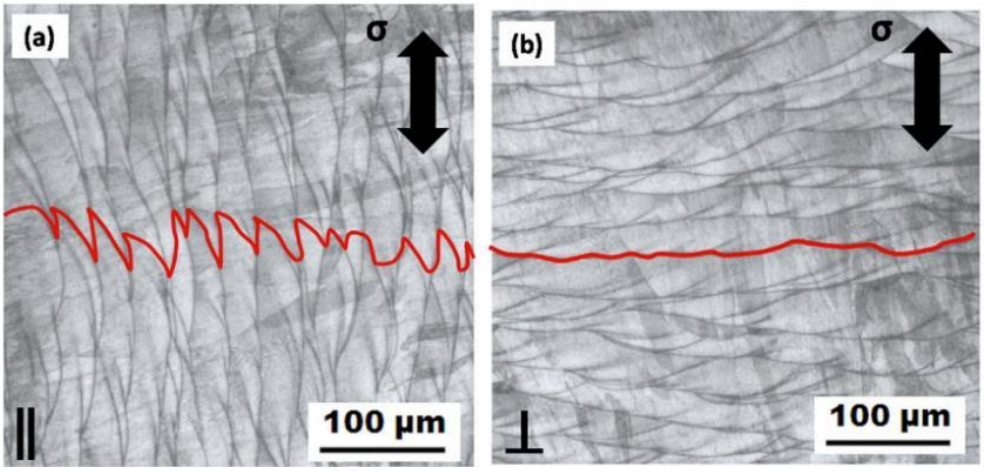

Figure 10. Difference in crack path; (a) loaded parallel to grain growth direction; (b) loaded perpendicular to grain growth direction [39].

The metastable austenitic matrix transforms through twinning or slip into ferromagnetic and body-centered tetragonal (BCT) α′-martensite, and paramagnetic and hexagonal close-packing (HCP) ε martensite under monotonic or cyclic deformation, increasing the strength and hardness of the material [47,49,50]. Blinn *et al*. [47] showed an improved fatigue life at a low-stress amplitude of laser deposition welded 316L due to α′-martensite formation, detected by an increase in ferromagnetic fraction. Austenite to α′-martensite transformation induces local compressive residual stress, which helps prevent crack tip opening [51].

2.3 Printing pattern

This section reviews the different printing patterns employed in the additive manufacturing of metal. Printing pattern has a great impact on thermal profile, hence affecting solidification behavior, microstructure, and mechanical properties [1,2,4,52]. Printing pattern as a process parameter does not require a change of material or additional equipment but still offers the opportunity to tailor the microstructure and mechanical properties of the material. This section discusses the effect of the following printing patterns: weaving patterns [53,54], unidirectional and bidirectional combined with reducing energy input [38], wiggle deposition strategy [55], and printing direction rotation [56,57].

2.3.1 Weaving patterns

The weaving pattern is used in welding to achieve good weld quality by ensuring uniform weld penetration and to increase efficiency by increasing the width of the weld bead [53], and the same principle has been applied in WAAM. Various weaving patterns are shown in Figure 11.

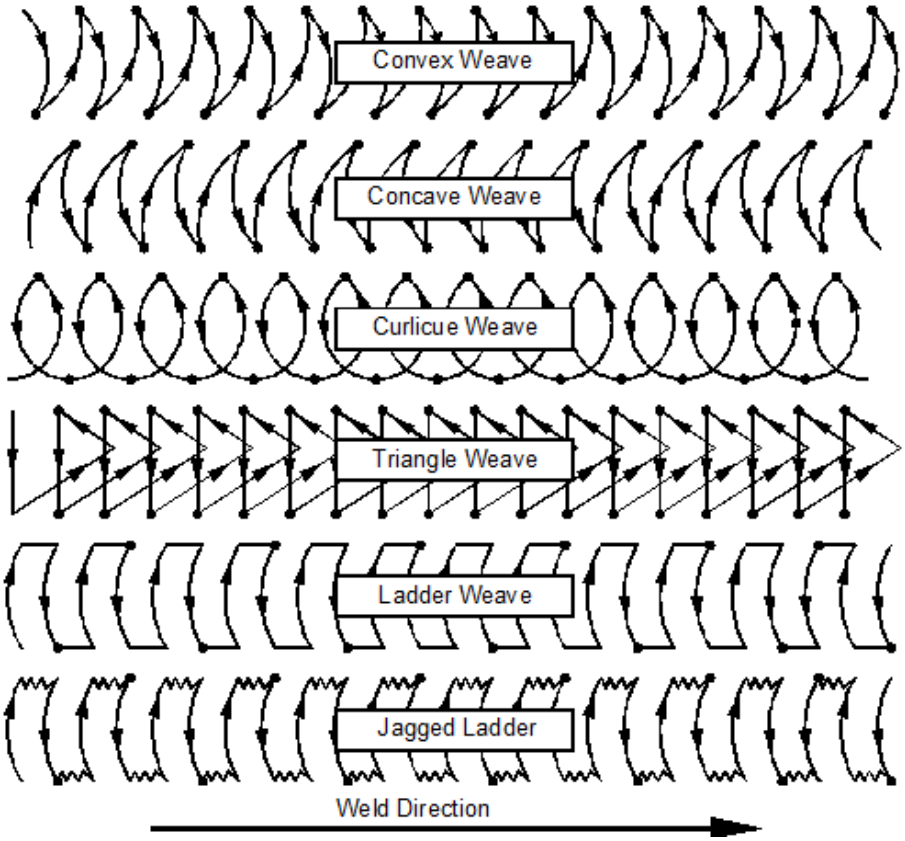

Figure 11. Different weaving patterns in welding [59].

Chen *et al*. [53] investigated the effect of weave frequency and amplitude on the temperature field in welding. Weave amplitude is defined as the width of the weaving pattern, while weave frequency is defined as the velocity in the printing direction divided by the distance in the printing direction between each loop of weave. Figure 12 shows the definition of parameters in the weaving pattern. First, in terms of weaving amplitude, the authors increased the weaving amplitude from 2 mm to 8 mm and kept the weaving frequency constant. The peak temperature in the center of the weld is 1885 °C and 1761 °C for 2 mm and 8 mm of weave amplitude respectively. This is because while increasing the weave amplitude, the welding speed v_x also has to increase to keep the weaving

amplitude constant, which resulted in a less localized heat source and less heat accumulation. Similarly, increasing the weave amplitude from 2 mm to 8 mm reduced the average temperature from 1843 °C to 1574 °C.

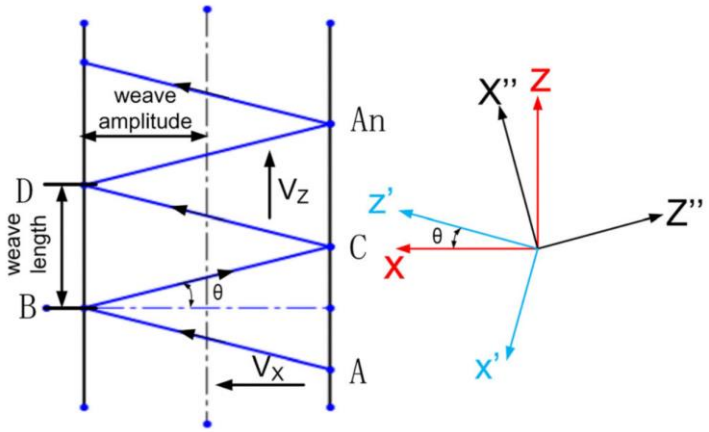

Figure 12. Schematic diagram of the weaving pattern [53].

The authors then investigated the effect of weave frequency while keeping the weave amplitude constant. Since weave frequency is the velocity in the printing direction divided by the weave length, reducing the weave length increases the weave frequency. By increasing the weave frequency from 0.25 Hz to 2 Hz, the peak temperature reduced from 1793 °C to 1665 °C, and the average temperature only reduced from 1578 °C and 1572 °C, which is much less of a reduction than increasing the weave amplitude. When the weave frequency is increased, the weave length decreases and the welding speed v_x needed to maintain a constant weave amplitude also decreases, resulting in more heat accumulation and a higher peak temperature.

This study showed that the temperature field can be controlled by changing weave amplitude and weave frequency to achieve different degrees of heat accumulation. However, the authors did not investigate the effect on microstructure and mechanical properties, which requires further study.

Akash *et al.* [54] compared circular weaving against multi-bead unidirectional printing in WAAM of Inconel 625 in terms of microstructure and mechanical properties. Both patterns showed columnar grains aligned in the build direction, with mostly equiaxed dendrites and a small number of cellular dendrites. The sample made by the circular weaving pattern has a finer subgrain structure than the sample made by unidirectional scanning, although the difference was not

quantified. The authors suggested that the finer microstructure is promoted by the weaving pattern, although the reason behind was not mentioned. Unidirectional printing however has the deposited bead reheated by the next weld bead, resulting in more heat accumulation [33].

The finer subgrain structure causes the sample made by circular weaving pattern to have a higher yield strength and ultimate tensile strength in both printing and build direction than the sample made by unidirectional scanning. Anisotropy in samples made by circular weaving pattern and by unidirectional printing is 5.3% and 5.8% respectively. Table 4 shows the mechanical properties of the samples.

Table 4. Mechanical properties of samples made by circular weaving and unidirectional printing [54].

Welding Pattern	Orientation	Yield Strength (MPa)	Ultimate Tensile Strength (MPa)	Elongation (%)
Circular Weaving	Longitudinal	568.4	762.2	52.9
	Transversal	534.3	721.8	51.2
Unidirectional printing	Longitudinal	514.6	670.9	49.8
	Transversal	490.8	632.5	48.3

2.3.2 Printing direction and heat input reduction

Moradi *et al*. [38] studied the effect of printing patterns and reducing laser power in direct laser deposition (DLD) of stellite 6 superalloy. Four samples of 5 layers wall were printed: unidirectional (D1) and bidirectional (D2) samples were printed with constant laser power of 250 W, and unidirectional (P1) and bidirectional (P2) samples were printed with decreasing laser power, from 300 W for the first layer to 100 W for the 5th layer, reducing laser power by 50 W per layer. Figure 13 shows schematically four samples with different printing patterns and laser power. The unidirectional samples have 50 s of cooling time between each layer, while the bidirectional samples have 35 s. The authors first compared the results between the constant laser power samples and between power-reducing samples to investigate the effect of the printing pattern, then investigated the effect of reducing laser power.

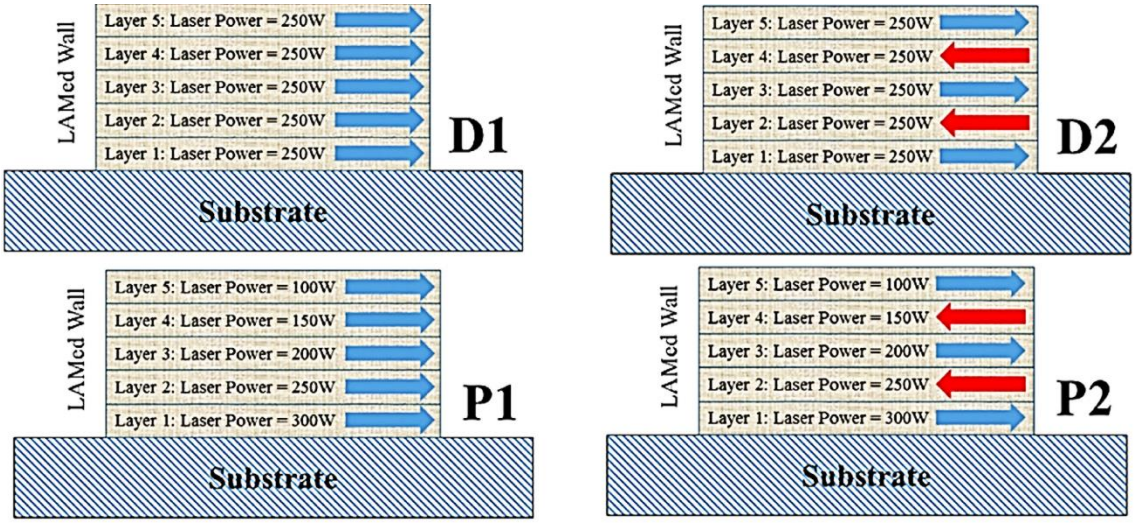

Figure 13. Deposition strategies for four samples [38].

First, the constant laser power samples D1 and D2 are compared, so the only difference is unidirectional and bidirectional scanning. The samples both have a large grain size at the first layer, decreasing to the smallest grain size in the middle and increasing again till the surface, as shown in Figure 14. The authors explained that the large grain size at the first layer is due to the substrate acting as a heat source. A steel substrate with a higher thermal conductivity than stellite 6 superalloy is used, and it absorbs the heat from irradiation of the laser, transferring heat to the first layer and causing grain growth. As more layers are deposited, the distance to the substrate increases, less heat is absorbed by the substrate, and grain size decreases. For the 5th layer, the large grain size is due to the shielding gas with low heat conductivity, causing less heat to be conducted away, and the heat is then accumulated and causes grain growth at the top of the sample. Figure 14 shows the grain size measurement across the samples with increasing distance to the substrate.

Although D1 and D2 have the same trend in grain size, D1 has a smaller grain size across all the layers. This is due to unidirectional printing allowing a more uniform cooling, while bidirectional printing has more heat accumulation during a change of direction. The unidirectional sample also has a longer cooling time since the print head has to travel back to the starting point while the bidirectional sample can continue printing the next layer at the same spot. Overall, the unidirectional sample has a smaller grain size due to less heat accumulation and longer cooling time. The suggestion is that the cooling time for both strategies should be 50 s instead of 50 s and

35 s, to eliminate the variable of cooling time to better focus the comparison between printing patterns.

After comparing samples D1 and D2, samples P1 and P2 are compared with D1 and D2 respectively to investigate the effect of reducing laser power. Both samples have decreasing grain size across layers. In the beginning, these samples have similar grain sizes to their constant laser power counterpart, due to the substrate acting as a heat source, but instead of the increasing grain size from the middle to the surface of the samples observed in D1 and D2, the grain size of P1 and P2 continues to decrease up to the surface, since the laser power is also continuously reduced. Reducing laser power reduces the heat for grain growth and causes grain size to decrease [60,61]. The P1 with unidirectional printing path again has a smaller grain size than the P2 with bidirectional printing path, due to more uniform cooling and longer cooling time. For all samples, the microhardness measurement agrees with the grain size measurement, where decreasing grain size shows increasing microhardness as also indicated by the Hall-Petch relation [40–44].

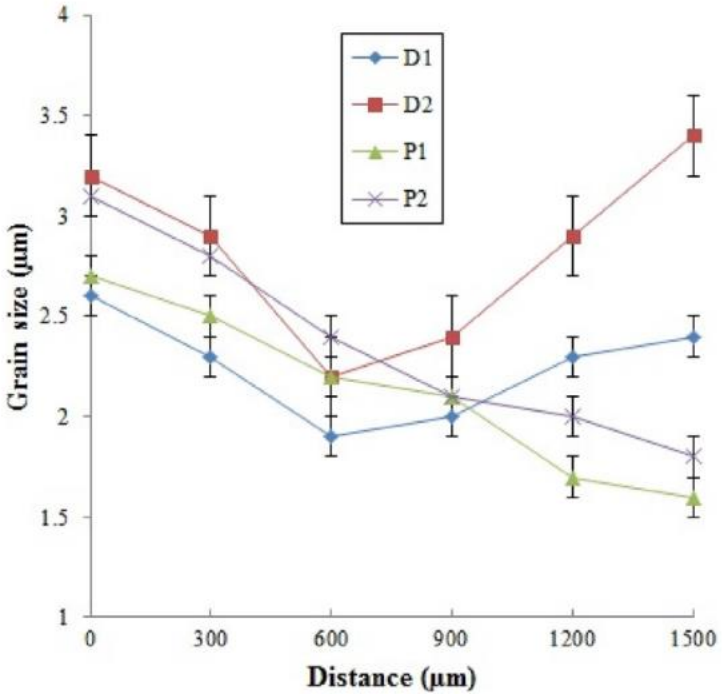

Figure 14. Grain size across samples in building direction [38].

This studied showed the possibility of controlling microstructure and mechanical properties through changing heat input across deposition layers, and instead of reducing heat input across

layers, further study of other strategies of varying heat input to induce or minimize anisotropy can be conducted. The effect of substrate and shielding gas in heat conduction can also be exploited in WAAM.

2.3.3 Wiggle printing pattern

Gao *et al*. [55] investigated the effect of the wiggle printing pattern in wire-laser DED of 316L. The wiggle printing pattern aims to induce instabilities in the melt pool and oscillation of thermal gradient by changing the printing direction by 90° every 1 mm, as depicted in Figure 15. The results are compared to the sample processed by bidirectional scanning. The resulting microstructure of both samples is the same as typical WAAM-produced 316L, having large, elongated grains aligned in the building direction and a fine solidification substructure, as discussed before. The samples have very similar microstructure including grain size, porosity, and density, except the shape of lack-of-fusion defects are different. The bidirectional sample has irregularly shaped lack-of-fusion defects while the wiggle sample has spherical lack-of-fusion defects. In terms of mechanical properties, the wiggle sample has a higher ultimate tensile strength and elongation than the bidirectional sample in the building direction, but lower ultimate tensile strength and elongation in the printing and transverse direction.

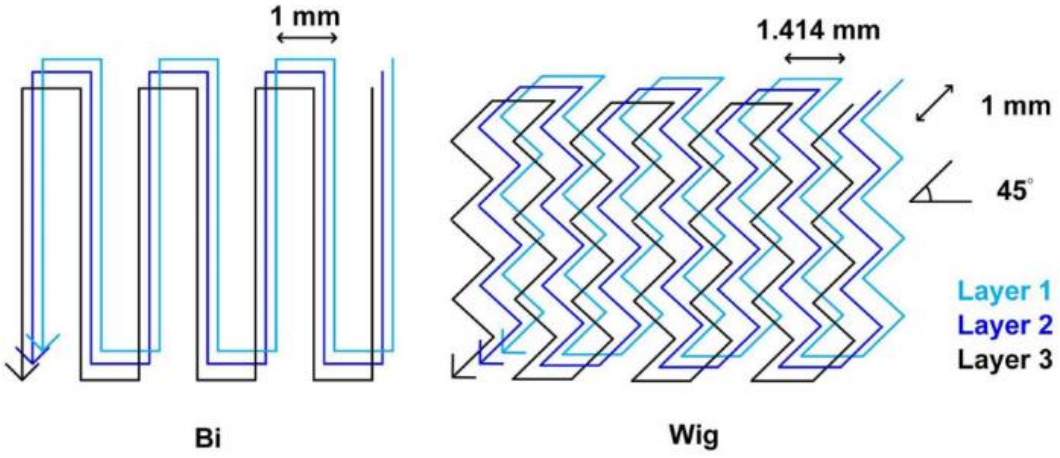

Figure 15. Bidirectional (left) and wiggle (right) printing patterns [55].

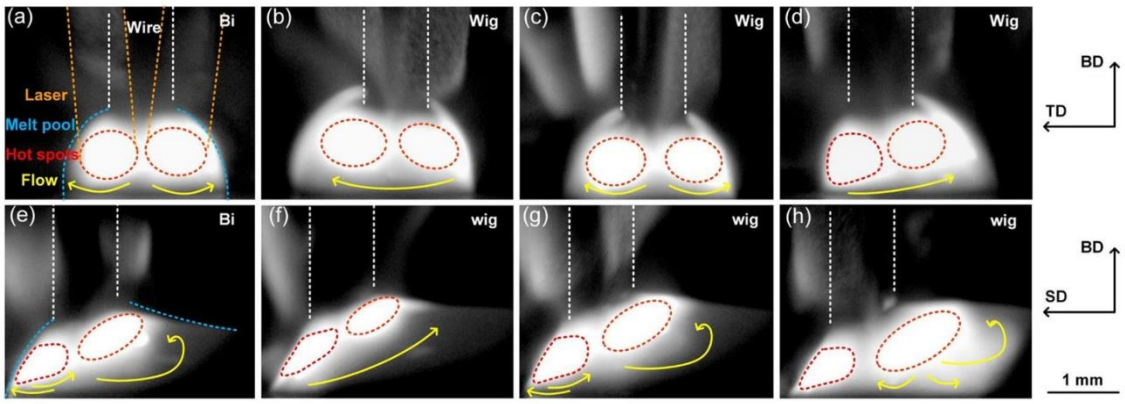

Figure 16. Melt pool dynamics observed by high-speed near-infrared imaging; (a) view of bidirectional printing in printing direction; (b)-(d) view of wiggle printing in printing direction; (e) view of bidirectional printing in the transverse direction; (f)-(h) view of wiggle printing in the transverse direction, showing three stages of melt pool oscillation [55].

The major difference between these samples is the texture, where the bidirectional sample features a strong <100> texture parallel to the building direction, due to the preferential growth direction of FCC metal to the largest heat extraction [24,31,35,39], discussed in Section 2.2.2. The wiggle sample however has a <110> texture parallel to the building direction, and the authors had to explain by observing the melt pool dynamic through high-speed near-infrared imaging and simulation of the thermal gradient in the melt pool. Bidirectional printing has a stable melt pool, while the wiggle strategy has an oscillating melt pool due to rapid transverse movements, as shown in Figure 16. The oscillation changes the incident angle of the melt pool to the lasers and affects laser absorption since laser reflectance is a function of incident angle. This resulted in three melt pool stages: at the weak laser absorption side where the melt surface flows from front to back, a non-affected stage that resembles the traditional printing pattern where the melt pool is not deflected, and at the strong laser absorption side, where melt surface flows radially outward from location with highest temperature. This oscillation of the melt pool induces high thermal fluctuation, which is confirmed by the simulation shown in Figure 17. The continuous change in the thermal gradient direction at the solidification front affects the preferred growth direction. The authors suggested that the system would grow in two perpendicular <100> directions by turn, in the form of [100] and [010] in opposite direction. The resulting vector is [110] parallel to the building direction, illustrated in Figure 17 schematically. The columnar grains are still present despite the oscillation of thermal gradient, due to the constraint of precursor solidified grains.

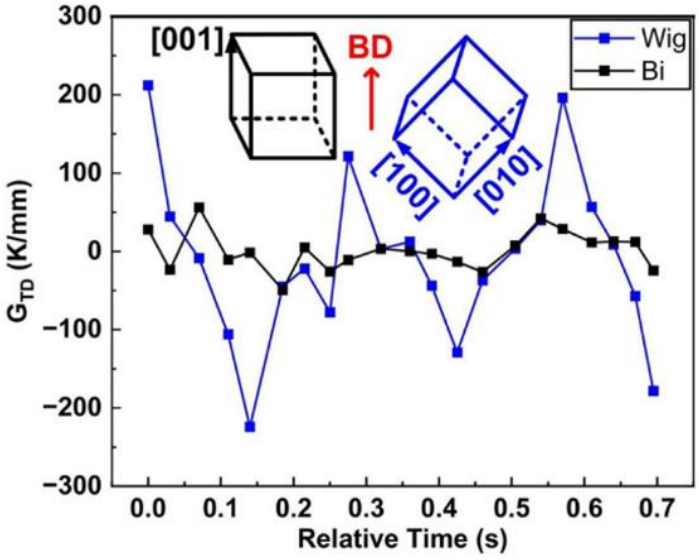

Figure 17. Thermal gradient history of wiggle and bidirectional printing obtained from simulation, and schematic illustration of texture alignment in build direction due to fluctuation of thermal gradient [55].

Due to the similarity of the microstructure of the samples, aside from different textures, the authors concluded that the increased mechanical performance in the building direction is due to modification of texture. The spherical shape of lack-of-fusion defects in wiggle samples should reduce stress concentration and potentially improve fatigue properties, which should be investigated in future studies. Overall, this novel printing pattern offers a promising solution to tailor mechanical performance through texture control.

2.3.4 Printing direction rotation

Another strategy is to rotate the printing direction in every deposition layer to avoid overlapping of scan paths and heat acumination. Leicht *et al*. [56] investigated the effect of rotating printing direction by 90°, 45°, and 67° of 316L in SLM. 90° and 45° are chosen since the temperature gradient only aligns every two and four layers respectively. For a 67° rotation, it is commonly used in SLM for a maximum number of deposition layers before overlapping, due to 67° being an irregular prime number and not being an exact multiple of 360 [62].

For the sample with no scan rotation, the microstructure has the typical elongated columnar grains, and the texture is <100> cells in the center of the melt pool and cells inclined by ±45° at the sides. The texture at the sides of the melt pool is also rotated by 45°, hence a strong <110> texture, shown in Figure 18. By rotating the printing direction by 90° the <100> band at the center of the melt

pool disappeared but the strong <110> texture is still present. Due to the limited alignment and change in temperature gradient, the formation of the <100> bands is prevented. A higher fraction of HAGB is also observed. The melt pool boundaries can be observed, and they are rotated by 90° every other layer as well. By reducing the rotation angle to 45°, the fraction of HAGB increases, the <110> texture is weakened, and the melt pool boundaries become even more complex. The 67° sample has a similar microstructure to the 45° sample.

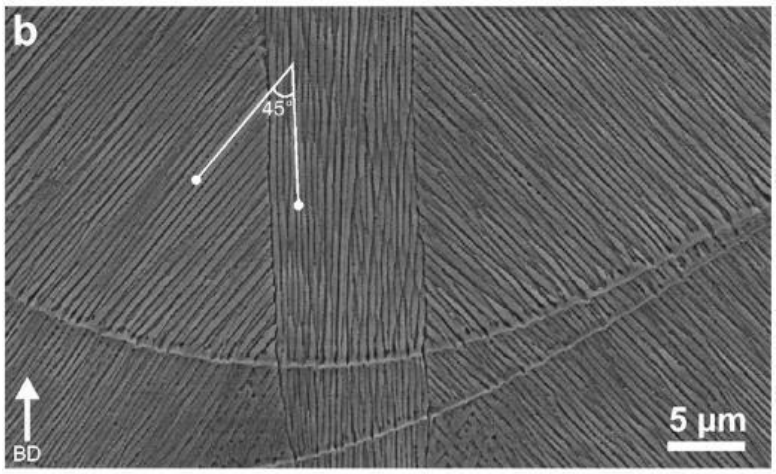

Figure 18. Microstructure of sample with no scan rotation: <100> band at the center of the melt pool, and 45° inclined cells at the sides [56].

In terms of mechanical properties, the sample with no scan rotation has the highest yield strength and ultimate tensile strength, but the lowest hardness value. The authors explained the difference in tensile and hardness properties is due to anisotropy, and high anisotropy is the reason behind the good tensile properties when compared to the other samples. For other samples, the tensile properties decreased with reduced rotation angle. The sample with no scan rotation also has the highest ductility, which is due to the strong alignment of grain, and also a strong <110> texture. A <110> texture has a higher Taylor factor than a <100> texture and is more favorable for deformation twinning [63], and reducing rotation angle weakens <110> texture, reducing ductility.

This study demonstrated a reduction of anisotropy through a rotating printing direction, with the tradeoff of reduced tensile properties. Although the authors interpreted the presence of anisotropy through the difference in tensile and hardness values, as well as mentioning that the sample with no scan rotation would have the lowest yield strength and ultimate tensile strength in the building direction, including tensile tests in the building direction would better support the statements of

strong grain alignment being the cause of high yield strength, ultimate tensile strength, and elongation.

Contradictory, Song *et al*. [57] have found that reducing the rotation angle, hence increasing the number of layers before overlapping affects grain refinement and strengthening. The effects of scan rotation angle on grain size and grain boundaries are shown in Table 5. Samples with no scan rotation are compared to scan rotation of 90° and 47° between deposition layers. The sample with no scan rotation has columnar grains aligned in the build direction, while the 90° and 47° samples have less aligned growth direction. This is because the direction of the heat transfer of the melt pool is different from the previous layer and the thermal gradient direction is modified by the scan rotation. The 90° and 47° samples have 8% and 15% reduced grain size respectively. The sample with 47° has the highest yield strength and ultimate tensile strength due to its finer grain size, but the sample with 90° has lower tensile properties than the sample with no rotation despite its lower grain size. The authors explained that this is due to similar grain size, and the higher fraction of HAGB in the 90° sample, which has higher mobility and is less effective as a dislocation barrier. This explanation agrees with the results of a study by Leicht *et al*. [56], that reducing the rotation angle increases the HAGB fraction and reduces tensile properties.

Table 5. Effects of scan rotation angle to grain size and grain boundaries, tensile properties extracted from figures, and table modified from [57].

	No rotation	90°	47°
Grain size (μm)	24.7	22.8	21.4
Fraction of HAGBs	12.4%	16.2%	17.2%
Fraction of LAGBs	27.9%	25.5%	24.6%
Fraction of grain boundary area	26.9%	27.1%	35.6%
Yield strength (MPa)	554	545	561
Ultimate tensile strength (MPa)	638	628	661
Elongation to failure (%)	44.2	41.5	48.7
Hardness ($HV_{0.2}$)	233	232	228

2.4 Literature review summary

Additive manufacturing provides various methods to affect the microstructure and mechanical properties of the material, from varying heat input and travel speed to employing complicated printing patterns like island deposition strategies. Due to the nature of the process, anisotropy in microstructure and mechanical properties is inherent. The strategies in the reviewed studies all either induce or reduce anisotropy. These studies also showed that printing patterns have a great effect on the thermal gradient of the samples, which influences the microstructure and texture, hence the mechanical properties of the material. The following points summarize the main result of the printing patterns discussed.

1. Weave amplitude and weave frequency can be controlled to achieve different degrees of heat accumulation and peak temperature, influencing microstructure and mechanical properties. A study compared circular weaving against uni-direction printing, and circular weaving resulted in a finer microstructure, which leads to higher yield strength and ultimate tensile strength.
2. A study investigated the effect of unidirectional and bidirectional printing patterns, as well as the effect of reducing energy input across the deposition layer. Firstly, the authors suggested that the increased grain size at the surface and near the substrate is due to shielding gas lowering heat conduction and the substrate acting as a heat source after accumulating heat. In terms of the printing patterns, unidirectional printing gives more time for each layer to cool down before the next deposition layer which results in a smaller grain size, while bidirectional printing gives less time and results in a larger grain size. In terms of the effect of reducing the laser power, grain size reduces since less heat is available for grain growth.
3. The wiggle deposition strategy alters the typical <100> texture to <110> texture by inducing fluctuation in the thermal gradient. The fluctuation of the thermal gradient is due to the oscillating melt pool from the rapid movement of the print head, which contacts the laser at different angles. Since laser reflectance is a function of incident angle, laser absorption hence heat input is different at each stage of the oscillation. This creates a fluctuation of thermal gradient and changes the direction of the largest heat extraction, which affects texture. The resulting <110> texture is then formed from the combination of <100> vectors in different directions from thermal gradient fluctuation.

4. Printing direction rotation limits the alignment of the thermal gradient. Increasing the rotation angle increases the number of layers before the alignment of the printing direction, reducing heat accumulation hence the grain size, and increasing the fraction of HAGB. This also rotates the melt pool and the direction of the largest heat extraction, which induces the <110> texture. The finer grain size should result in higher strength, but the higher fraction of HAGB reduces strength. A combination of these two effects causes the sample with 90° rotation to have lower yield strength and ultimate tensile strength than the sample with no rotation.

2.5 Research questions

The reviewed studies show a few important aspects to be further studied. Firstly, there have been limited studies in weaving patterns, especially regarding comparison between different weaving patterns. Secondly, most research focuses on printing patterns' effect on microstructure and mechanical properties, but not the feasibility of using the printing patterns. For instance, a rotating layer would cause waviness in the side walls and side wall collapse could occur. Therefore, surface quality and macro-defects need to be evaluated when considering the implementation of printing patterns. Finally, three studies showed strengthening or weakening of the material through reducing or increasing the intensity of the <100> texture [55,60,61], which would impact mechanical properties greatly. Therefore, texture analysis is important when characterizing new printing patterns. Based on these research gaps, the following research questions are formulated:

1. What is the effect of different weaving patterns on the microstructure and mechanical properties of the material? Comparison between weaving patterns and normal line printing is required to show the distinct characteristics of the unique weaving patterns.
2. What is the effect of weaving patterns and processing parameters on the surface quality of the part? Good surface quality can reduce the time for machining and material waste, surface quality between different printing patterns and process parameters can be measured with a 3D scanner to investigate how to improve surface quality.
3. How do the weaving patterns influence grain growth and grain alignment, as well as texture? These factors greatly influence mechanical properties, and proper characterization of grain structure and texture is required to explain the characteristics of their mechanical properties.

3 Printing process

This Chapter discusses the process of printing six WAAM blocks through six different printing patterns. First, preliminary testing is conducted to select suitable printing parameters. Then, six printing patterns are optimized to yield a stable and good-quality print. Finally, the process of printing the six WAAM blocks and extracting the samples for characterization is discussed.

3.1 Process and Material

Gas metal arc welding (GMAW) is used to manufacture thick-walled WAAM samples. In total, six blocks are made by different scanning patterns. Two different WAAM setups are used to accommodate path programming of the scanning patterns: Fronius TransPulsSynergic 5000 with 3-axis motion control system, and Fronius TransPulsSynergic Cold Metal Transfer with 6-axis robot. Figure 19 shows the 3-axis motion control and 6-axis robot setups. Both setups utilize a GMAW power source to control parameters for material deposition, and a motion control system for controlling the motion of the welding torch. Through programming of the scanning path, different scanning patterns are realized. The scanning parameters are determined through preliminary testing, which is discussed below, and the default gas flow parameters in Fronius TransPulsSynergic are used. For shielding gas, 98%-Ar 2%-O_2 is used, commonly used for austenitic stainless steels. It improves the mechanical properties and corrosion resistance of the weld [64].

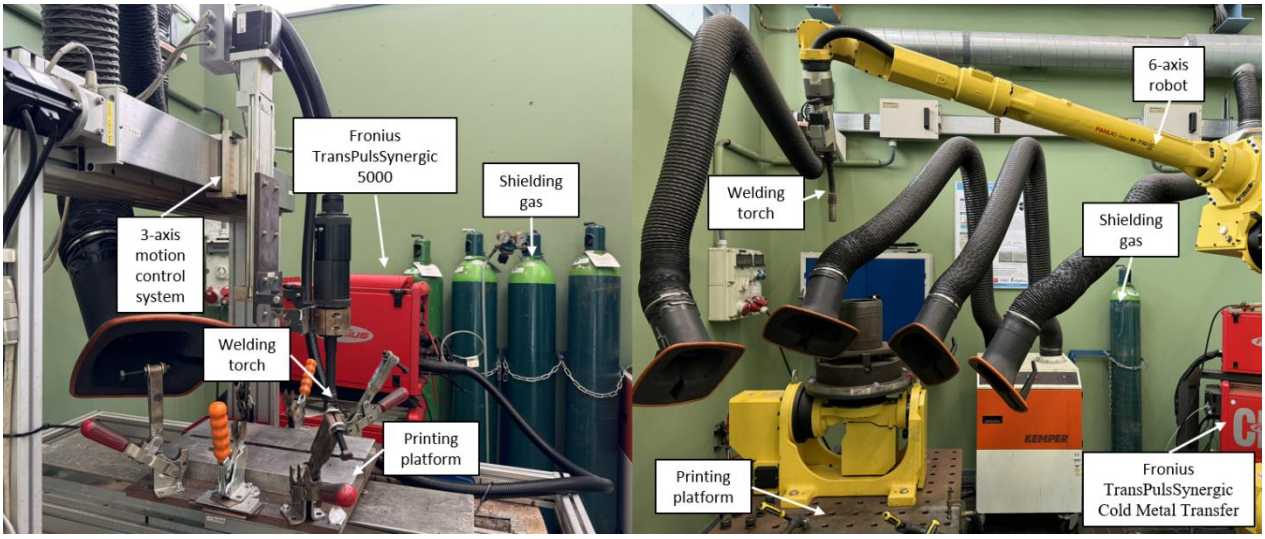

Figure 19 3-axis motion control system (right) and 6-axis robot (left)t WAAM setups.

The deposited material is 316L, an austenitic stainless steel with excellent corrosion resistance. Welding wire from Thermanit with a 1 mm wire diameter is used for both WAAM setups. The composition of the wire is shown in Table 6.

Table 6 Composition of the wire, compositions are given in weight (wt%).

Fe	**C**	**Si**	**Mn**	**P**	**S**	**Cr**	**Mo**	**Ni**	**Cu**
Bal.	<0.01	0.97	1.6	0.022	0.007	18.2	2.6	11.7	0.2

3.2 Preliminary testing

Preliminary testing is conducted to determine the printing parameters including current, voltage, wire feed rate (WFR), and travel speed (TS). Synergy welding setting is used for the setup to automatically determine the current, and voltage required for a specified WFR and material. Single lines of welds are printed onto a thin rectangular plate with varied combinations of WFR and TS. WFR from 3 m/min up to 6 m/min are tested, with increments of 1 m/min. At each increment of WFR, TS of 3 mm/s, 6 mm/s, 9 mm/s, and 12 mm/s are tested. Different combinations of wire feed rate and travel speed are tested to find a combination that gives a wide weld bead with a good ratio between width and height since the ratio determines the wetting angle of the sides of the weld bead to the substrate. This angle influences the quality of the overlap of the next weld bead. The goal is to find a combination of WFR and TS that gives a wide weld bead to improve the deposition rate and avoid steep wetting angles to avoid a lack-of-fusion defects when the next weld bead is deposited.

Figure 20 Lines printed with different combinations of WFR and TS. The numbers indicate WFR : TS in m/min and mm/s, respectively.

Figure 20 shows the influence of WFR and TS on the weld bead geometry. With increased WFR, the deposition rate increases, and heat input also increases as the program adjusts the current and voltage automatically. Increasing TS reduces heat input and the deposition rate per unit length, narrowing the weld bead. Since the cooling rate also increases, the weld bead becomes narrower, and it would be difficult for the subsequent weld bead to have a good overlap to ensure good weld penetration. Therefore, a high TS is avoided.

The spacing between two welds is needed for a sufficient overlap to have a flat surface and good weld penetration. Sets of two welds with different spacing are printed for a few selected combinations of WFR and TS to optimize the spacing, shown in Figure 21. An initial spacing of 0.7 multiplied by the width of the weld bead is used, and the spacing is adjusted according to the overlap of the weld beads. The spacing is reduced if the overlap is insufficient to achieve a flat surface and increased if the weld beads are too close to each other. It was found that for lower WFRs, it is still difficult to create a flat surface between the welds even by finely adjusting the spacing.

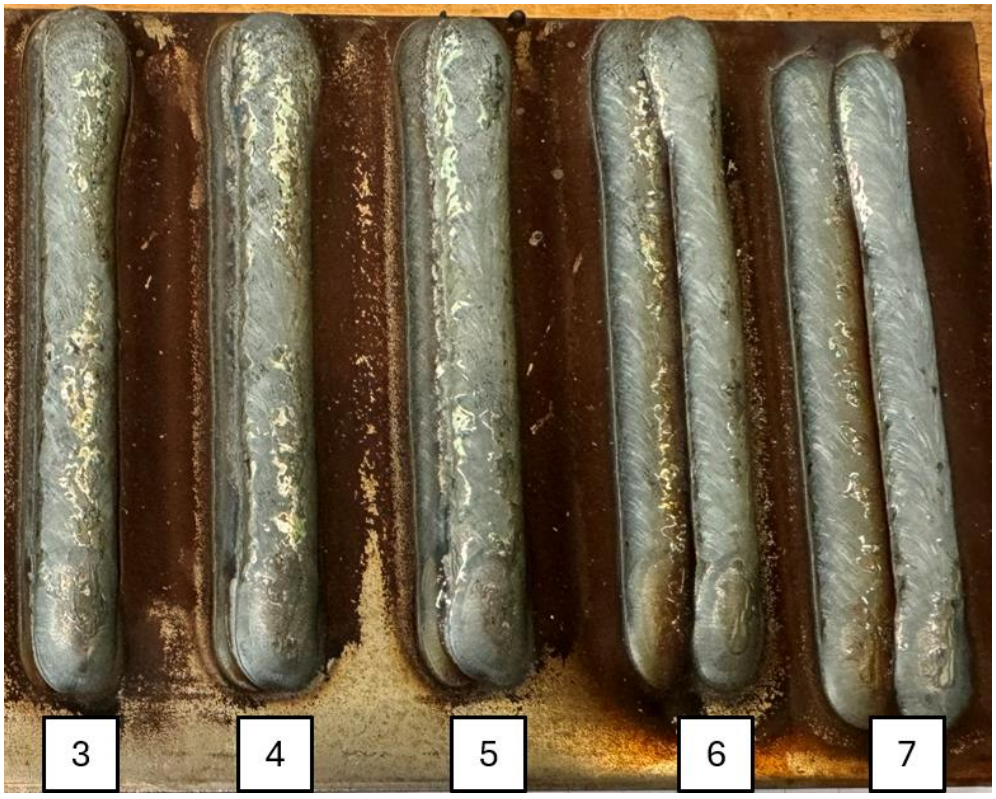

Figure 21 Two welds printed with WFR of 6 m/min and TS of 3 mm/s next to each other. The number denotes the spacing in mm.

A combination of WFR of 6.5 m/min and TS of 5 mm/s is chosen after the preliminary testing based on the weld bead width, to give a high deposition rate, and to have a gradual side angle and sufficient weld beads overlap. The printing parameters are listed in Table 7. The heat input of the process is calculated by the following equation:

$$HI = \frac{\eta UI}{TS}$$

The η is the thermal efficiency, which is assumed to be 0.8 for GMAW [65]. The resulting heat input is 0.417 kJ/mm.

Table 7 Printing parameters of WAAM.

Heat input (J/mm^2)	417.1
Current (A)	131
Voltage (V)	19.9
Wire feed rate (m/min)	6.5
Travel speed (mm/s)	5
Thermal efficiency η	0.8
Shielding gas	98%-Ar 2%-O_2
Gas flow rate (l/min)	20
Gas pre-flow time (s)	1.5
Gas post-flow time (s)	2.0

3.3 Printing patterns

In total six printing patterns are used to investigate the effect of printing patterns on microstructure and mechanical properties. The first two patterns are unidirectional and bidirectional printing, which consist of overlapping of single welds next to each other. These printing strategies are conventional and widely used in research and commercial use of WAAM [4]. In this thesis, these two patterns are used to compare the effect of the other four different weaving patterns and are together referred to as line printing patterns.

The other four printing patterns are considered weaving patterns, used in welding to achieve good weld quality by ensuring good and uniform weld penetration and to increase efficiency by increasing the width of the weld bead [53]. These four patterns consist of rectangular, zigzag,

triangular, and circular weaving, as shown in Figure 22. These four patterns can be categorized into two sub-groups, with the rectangular and zigzag pattern being more similar in terms of their printing paths having minimal overlap; and triangular and circular weaving both having direct overlap of printing path. This will affect layer thickness, thermal profile, heat accumulation, microstructure, and mechanical properties.

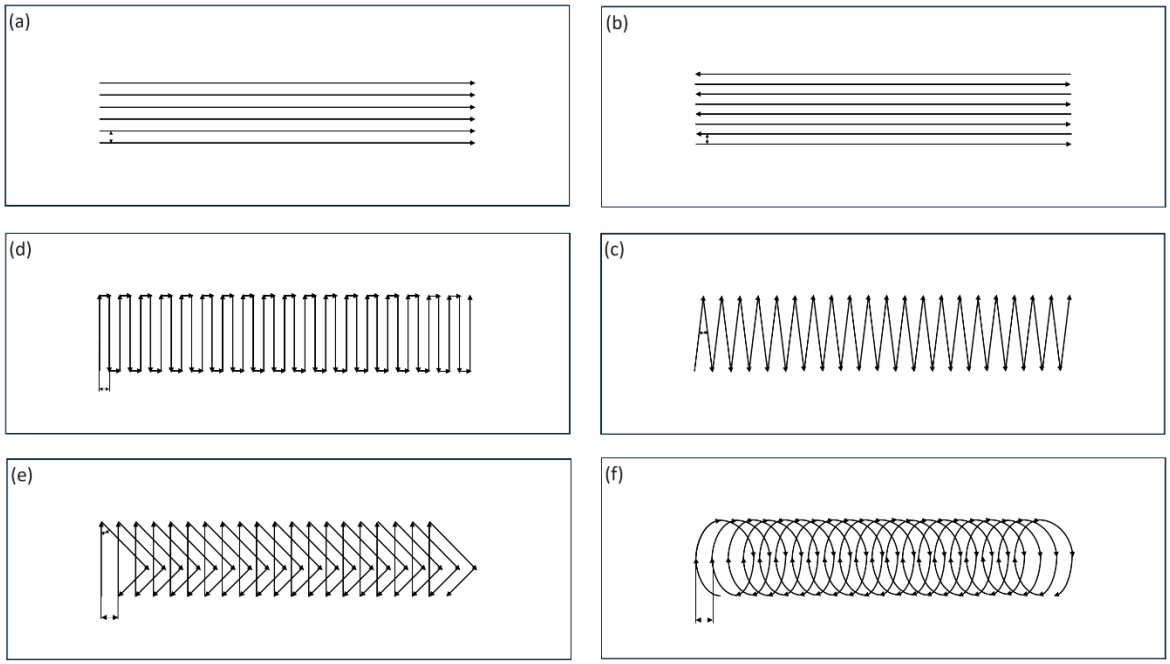

Figure 22 Six different investigated printing patterns and their variables: (a) unidirectional printing, (b) bidirectional printing;(c) rectangular weaving; (d) zigzag weaving; (e) triangular weaving; and (f) circular weaving.

These six printing patterns all have dimensional variables to be adjusted according to the printing parameters selected to have the proper overlap of weld beads. A proper printing path is important to avoid large gaps that lead to lack-of-fusion defects, or excessive overlap that leads to sagging. Optimization of all six printing patterns is conducted to determine the proper value for these dimension variables. For each printing pattern, a starting variable is estimated from the initial spacing discussed previously, which is 0.7 multiplied by the width of the weld bead. The degree of overlapping is then adjusted gradually to achieve a printing path with a flat surface and a low degree of waviness in the side profiles.

80 mm × 80 mm × 10 mm 316L thin plates are used as substrates, clamped securely on four corners to limit distortion during printing. An area of 30 mm × 60 mm is deposited by each printing pattern

in the center of the plates. For unidirectional printing, bidirectional printing, rectangular weaving, zigzag weaving, and triangular weaving, Fronius TransPulsSynergic 5000 with a 3-axis motion control system is used. For circular weaving, Fronius TransPulsSynergic Cold Metal Transfer with a 6-axis robot is used instead due to the limitation of printing path programing in the 3-axis motion control system. Optimization of each of the printing patterns is discussed below.

3.3.1 Unidirectional printing

The variable of unidirectional printing is the distance between each weld. Figure 23 shows the effect of increasing the distance from 4.4 mm to 4.8 mm. With smaller line spacings, namely 4.4 mm and 4.6 mm, sufficient weld bead overlap is achieved, and a flat surface is created. For a line spacing of 4.8 mm, the gap between two welds is too large and the next weld has insufficient material to overlap and penetrate the previous weld. This leads to regions with concave-shaped crevices, which would create lack-of-fusion defects as more layers are deposited on top of it. Therefore, a distance of 4.6 mm was initially chosen.

However, for unidirectional printing, the optimal printing path is sensitive to the size of the substrate. For making the thick-walled WAAM blocks, a much larger and thicker substrate is used, leading to a much larger heat sink for heat extraction. Each weld is also significantly longer (from 60 mm to 150 mm), leading to significantly more time for the initial part of the weld to cool during printing. The time it takes for the welding torch to return to the starting position also increases with longer welds, further allowing more time for the last weld to cool down. This means that there is less heat accumulation and less issue with sagging for the subsequent welds. Therefore, for a larger substrate, larger spacing can be used without defects, and a distance of 4.8 mm is chosen after further testing with the large substrate.

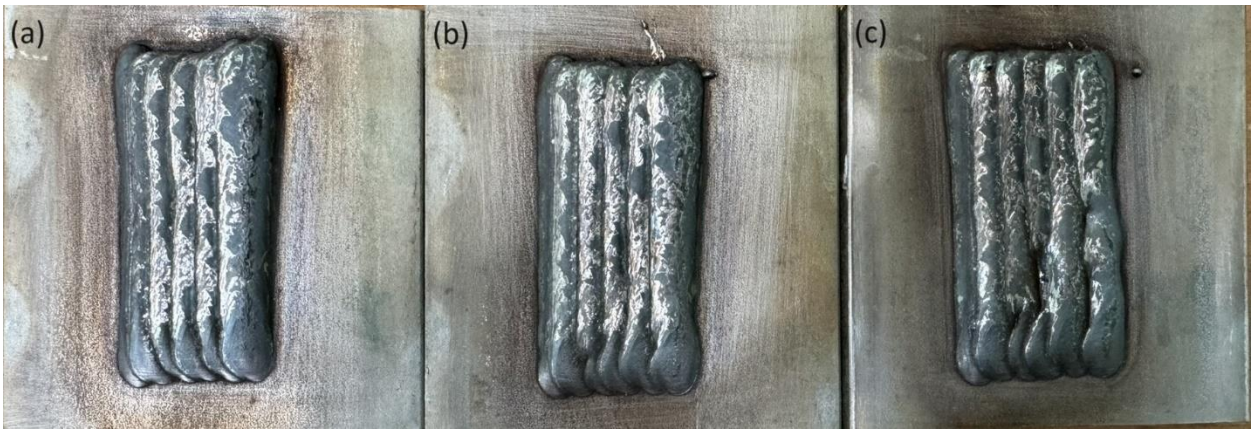

Figure 23 Unidirectional printing with different line spacing: (a) 4.4 mm; (b) 4.6 mm; (c) 4.8 mm.

3.3.2 Bidirectional printing

Similar to unidirectional printing, the variable is also the distance between the welds. Figure 24 shows the effect of increasing the distance from 3.5 mm to 5 mm. The effect is similar to unidirectional printing, with defects observed at large spacing. The optimal spacing however is smaller than the optimal spacing of unidirectional printing. This is because unlike in unidirectional printing, the next line begins immediately at the end of the previous weld, without taking time for the weld torch to return to the other end. This leads to more heat accumulation and higher mobility of the molten material during solidification. Therefore, a smaller distance is required, and a spacing of 4 mm is chosen.

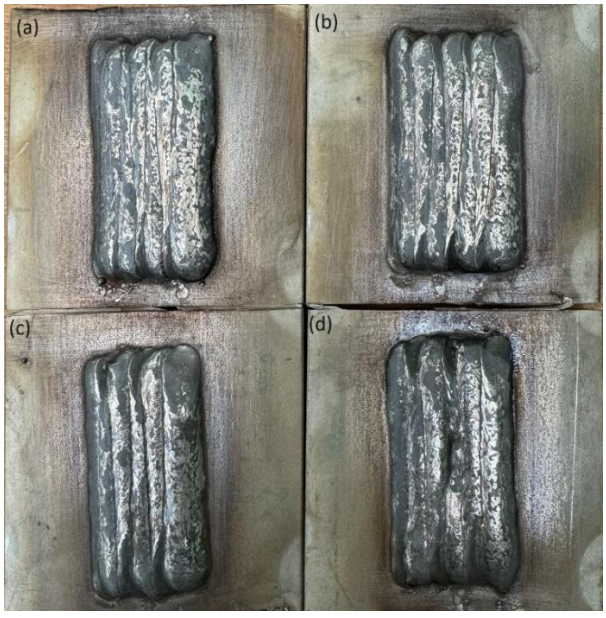

Figure 24 Bidirectional printing with different line spacing: (a) 3.5 mm; (b) 4 mm; (c) 4.5 mm; (d) 5 mm.

3.3.3 Rectangular weaving

The variable for rectangular weaving is the length of the short lines parallel to the printing direction. Figure 25 shows the effect of changing the length of the short lines. Changing the length of the short lines affects the degree of overlap of the long lines perpendicular to the printing direction, which is important to ensure flatness and avoid lack-of-fusion defects for the subsequent layers. The length of the short line also affects the waviness of the side profile, which is important to minimize waviness to have a large and stable surface for the next layer to be deposited, and to reduce time and material wastage in postprocessing machining. A length of 4 mm for the short lines is chosen after testing.

Figure 25 Rectangular weaving with different lengths of the short lines parallel to the printing direction: (a) 4 mm; (b) 4.5 mm; (c) 5 mm; (d) 5.5 mm.

3.3.4 Zigzag weaving pattern

The variable in the zigzag weaving pattern is the angle between the straight lines, which determines the degree of overlap. Because the width of the layer is constrained at 30 mm, changing the angle also changes the length of the line. The overlap is large close to the angle and reduces as the lines diverge. The zigzag weaving pattern is similar to the rectangular weaving pattern geometrically, both comprise straight lines close to the transverse direction going in alternating directions. They are also similar in appearance. Therefore, it also has similar behavior when the angle is increased: the surface becomes less flat and the side profile's waviness increases. Figure 26 shows the effect of increasing the angle between the lines from 7° to 10°. Due to its flatness and limited side profile waviness, 7° is chosen.

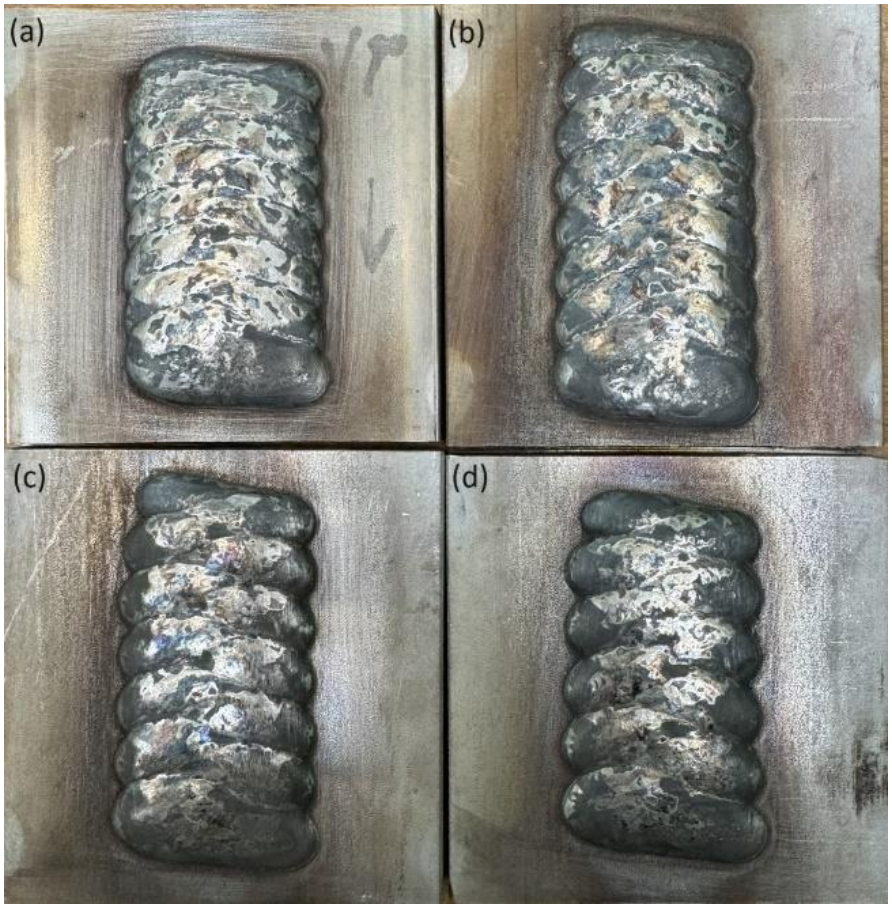

Figure 26 Zigzag weaving with different angles between the lines: (a) 7°; (b) 8°; (c) 9°; (d) 10°.

3.3.5 Triangular weaving pattern

The variables in triangular weaving patterns are the distance between the base of the triangles and the angle between the base and the sides of the triangle. Due to the higher complexity of this weaving pattern, the CAD program Autodesk Fusion is used to visualize the triangular weaving patterns since it allows adding geometrical constraints between lines and quick modification of the two variables. Initially, after visualization from CAD drawings, the distance between the base of the triangles is chosen to be 7 mm. This is larger than the spacings in other printing patterns, but this is to accommodate the direct overlapping of printing paths in this pattern.

After constraining the distance between the base of the triangles, the angles between the sides and the base of the triangle can be modified to change the degree of overlap between the sides of the triangles. Figure 27 shows the effect of changing the angle between the base and the sides of the triangle. Based on the visualization of CAD drawings, a starting angle of 50° is chosen for the tests.

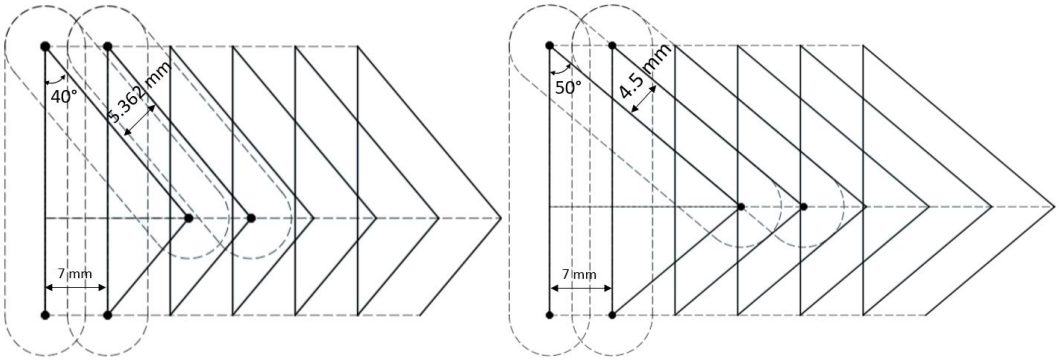

Figure 27 Effect of changing the angle between the base and the sides of the triangles on the degree of overlap between the sides of the triangle, with slots in dotted lines representing the weld bead; Left: 40° with 5.362 mm between the sides of the triangles; Left: 50° with 4.5 mm between the sides of the triangles.

Figure 28 shows the effect of increasing the angle between the base and sides of triangles from 40° to 55°. Increasing the angle reduces the flatness of the weld. It also makes the triangular shape at the end of the weld more acute, which would be problematic for the next layer as a flat surface for support is preferred to be deposited onto to prevent sagging. The angle does not affect the waviness of the side profiles, since this is determined by the distance between the base of the triangles, which has been fixed at 7 mm. All the samples have an issue with the surface not being flat but bulging at one side due to the asymmetrical printing path of this weaving pattern. 45° is chosen since it gives a relatively flat surface, and further reducing the angle would result in excessive overlap in the sides of the triangles, making the issue with the bulged surface more severe.

Figure 28 Triangular weaving patterns with different angle between the base and the sides of the triangles: (a) 40°; (b) 45°; (c) 50°; (d) 55°.

3.3.6 Circular weaving pattern

The circular weaving pattern is a spiral projected in a tilted plane, which can be described as translating ellipses. The variables in the circular weaving pattern are the ratio between the major and minor axes of the ellipse and the displacement distance of the ellipse. Initially, the ratio between the axes is set at 3:2 arbitrarily, and CAD drawings are used to visualize the effect of the different displacements. Figure 29 shows schematically the effect of changing the spacing between the ellipses. Note that the circular weaving pattern is not multiple displacing ellipses, but a continuous path, with an endpoint of the ellipse connect to the starting point of the next ellipse by modifying the curvature of the last quarter of the ellipses. The simplification made in Figure 29 is for better visualization of the weld bead overlaps.

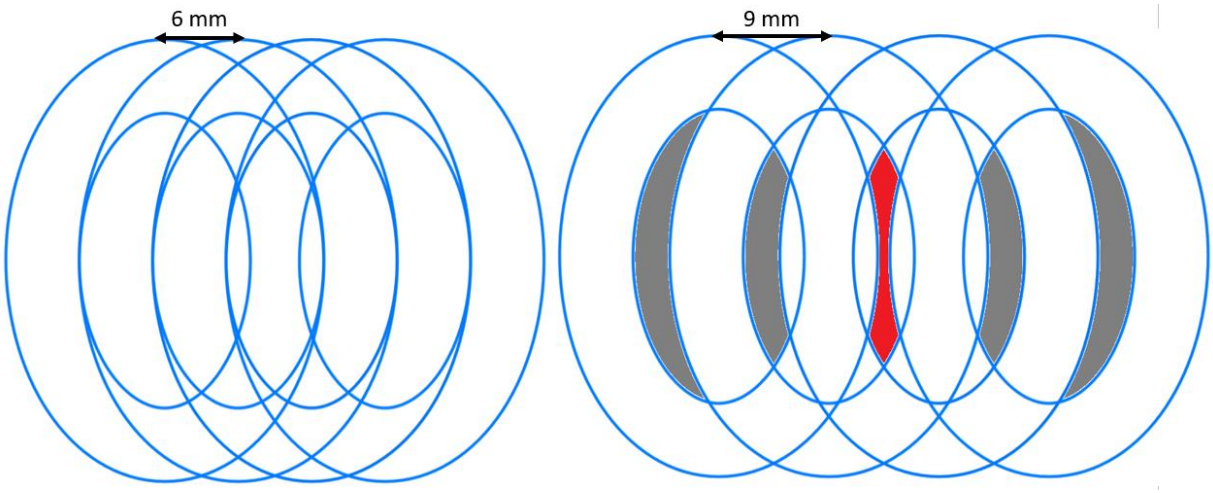

Figure 29 Effect of changing the displacement distance between ellipses; Left: Displacement of 6 mm. Right: Displacement of 9 mm, with unfilled gaps (in grey) for the first and last ellipses, and unfilled gaps (in red) for ellipses when equilibrium has been reached.

At 6 mm displacement, the first two ellipses' gap is only filled by the first half of the next two ellipses, and there is not sufficient overlap. For the third ellipse, the gap is filled by the second half of the first ellipse, and the first half of the subsequent ellipse. Therefore, it would take three ellipses to reach equilibrium at this displacement. At 9 mm displacement, the gaps of the first and the last ellipses are not completely filled. Even when equilibrium is reached, the gap is not completely filled by the previous and subsequent ellipses. Therefore, 9 mm displacement is too large for ellipses with an axis ratio of 3:2.

The issue of having insufficient overlap at the beginning and the end of the printing path can be solved by adding smaller ellipses with a 5 mm offset from the first and last ellipses and replacing them as the next starting point. Figure 30 shows the modified circular weaving pattern to accommodate this issue. The gaps are filled by the small ellipses and a flatter surface is provided for the next layer to be deposited onto.

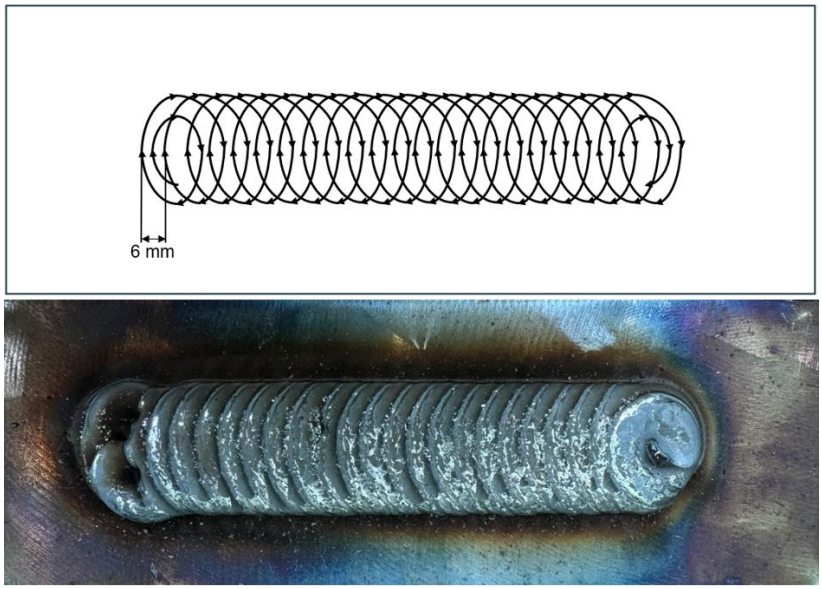

Figure 30 Circular weaving pattern with modified ends.

3.4 Printing WAAM blocks and sample preparation

Each printing pattern is used to make WAAM blocks that are used to produce the samples used in microstructural characterization and mechanical testing. The dimensions of the WAAM blocks are 60 mm×30 mm×150 mm. The size of the WAAM blocks is determined by the number and size of the required tensile samples. The WAAM blocks are large enough for five tensile samples to be extracted in the printing direction and five in the building direction.

The substrate used is 150 mm × 80 mm × 25 mm S690 high-strength steel plates, which are much thicker than the 316L plates used in the preliminary testing. The increased thickness of the substrate is to prevent large residual stress distortion from the repeated thermal cycles and the large area of deposition. The distortion is constrained by clamping at four corners of the substrate.

For printing the WAAM blocks, the welding torch is first moved to the starting position on the substrate. The tip of the wire is 13 mm away from the surface of the substrate. This is followed by the execution of the printing path program. When the layer has been printed, it is air-cooled to an interpass temperature of 120 ºC, measured by a handheld thermocouple. The hottest part of the layer, which is the last part of the deposition, is ensured to be under 120 ºC. The welding torch is raised to be 13 mm away from the surface of the layer and the next layer is deposited. Layers are deposited until the height of the block reaches at least 60 mm. Figure 31 shows the WAAM blocks from different printing patterns.

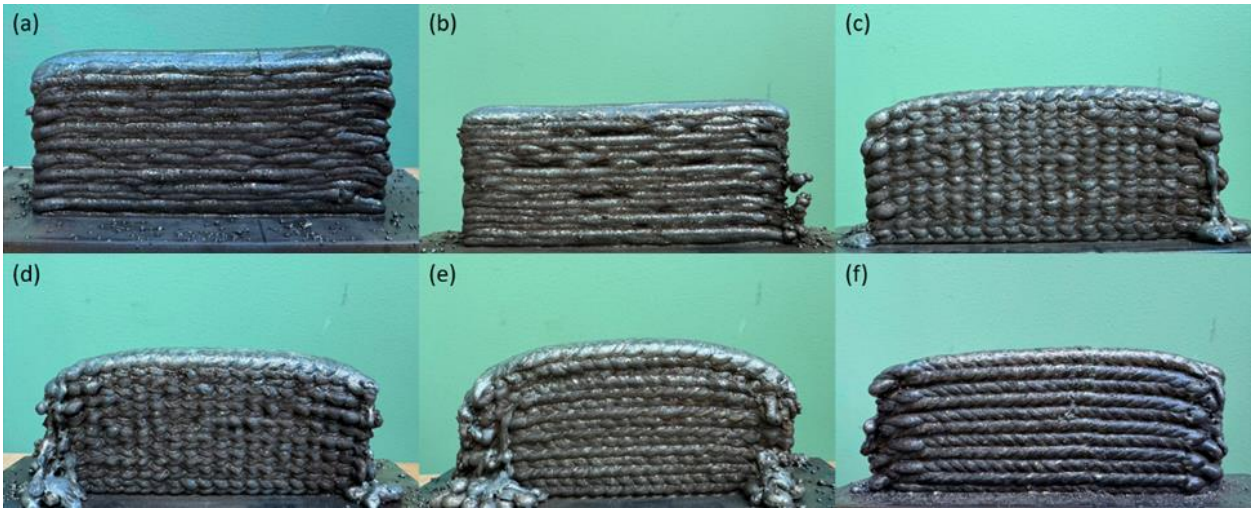

Figure 31 All WAAM blocks printed by the six printing patterns: (a) Unidirectional printing; (b) Bidirectional printing; (c) Rectangular weaving; (d) Zigzag weaving; (e) Triangular weaving; (f) Circular weaving.

During printing, several in-situ measurements are made. Welding monitor Weldmon AMV 3500 is used to measure the current and voltage with a 5000 Hz sampling rate during printing, which is useful for estimating the heat input and monitoring printing stability. The thermal profile is recorded by a thermal camera VarioCAM HD, which can be used to derive the cooling rate and compare the thermal profile of the different printing patterns. The thermal cycle of the substrate is also measured by attaching a thermocouple to the surface of the substrate, 10 mm from the edge of the printing path. The results of these in-situ measurements are discussed in Chapter 4.

3.5 Sample preparation

From the WAAM blocks, tensile samples and samples for microstructural characterization are extracted. Figure 32 shows the dimensions of the WAAM blocks and the locations of the tensile samples. The tensile samples are based on the work of Sood *et al.* and Tan *et al.* [66,67], and the dimensions comply with ISO 6892-1 [68], a standard for tensile testing of metallic material at room temperature. The tensile samples are cut from the WAAM blocks with electrical discharge machining (EDM), followed by computer numerical control (CNC) machining to produce the required grip geometry. For each WAAM block, five samples parallel to the building direction are extracted. The samples are located across the transverse direction with equal spacing. They are named according to the first letters of their printing pattern, followed by their orientation with respect to the WAAM block. Additionally, a number indicates its position relative to the transverse direction, from left to right indicated by number 1 to number 5, with 1 and 5 for samples at the

outer edges close to the side walls, 2 and 4 closer to the center, and 3 right in the center. For example, UNI-BD3 refers to the sample parallel to the building direction, extracted from the center of the block.

Because the material of the substrate is different from the wire, the location of the tensile samples avoids the first three layers to ensure the results are not influenced by the interface of the two materials. The tensile samples are taken from the locations of the WAAM blocks that are considered to be in equilibrium, which means the ends of the printing path are avoided. This is because at these locations the thermal profile and direction of the largest heat extraction is different than in the bulk, and the microstructure would be influenced. The top layer is also avoided, because it experiences no remelting, and its residual stress and microstructure could be more different from the middle layers [69].

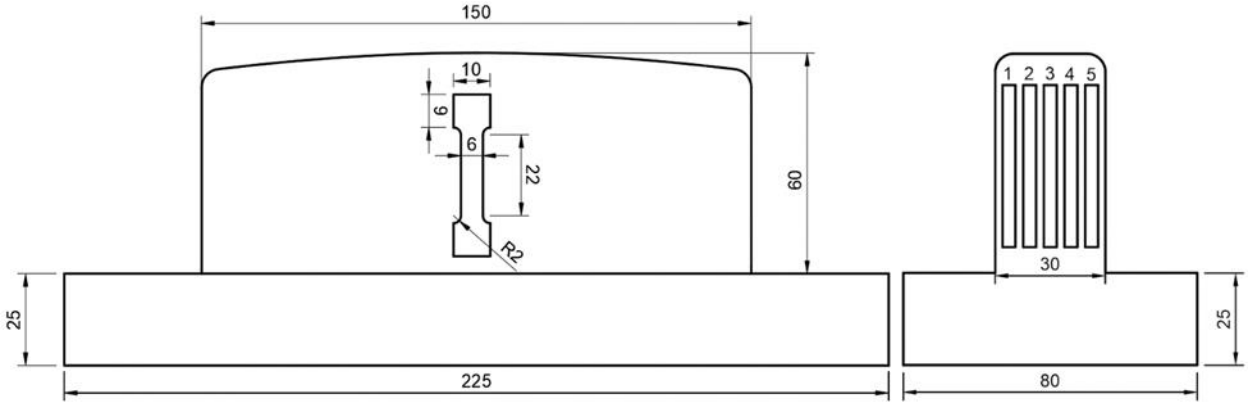

Figure 32 Dimensions of the WAAM blocks and the tensile samples. The location of the tensile samples is offset to reserve a part of the sample for microstructural characterization.

One side of the WAAM blocks is reserved for making samples for optical microscopy, microhardness testing, x-ray diffraction (XRD), and electron beam backscatter diffraction (EBSD). Samples from three cross sections are cut from all six WAAM blocks. After cutting, the samples are embedded in conductive cold embedding resin Demotec 70. The embedded samples are prepared with automatic sanding and polishing machine Tegramin-30, sanded from 160 to 2000 grit with SiC sandpaper, and polished with polishing cloth with polishing paste from 3 μm up to 1 μm. This is followed by 30 s of etching with an etchant consisting of 300 mL H_2O, 60 mL HCl fuming 37%, and 3 g $K_2O_5S_2$, an etchant used by Palmeira *et al.* [35,37] on 316 L samples printed by WAAM to effectively reveal the microstructure. This etchant has a modified composition of a tint etchant developed by Beraha for color etching of austenitic stainless steel [70].

Figure 33 shows the locations of the samples in relation to the WAAM blocks and the coordinate system for labeling the samples. The X axis is the transverse direction, the Y axis is the printing direction, and the Z axis is the building direction. The samples are named according to the first three letters of their printing pattern, followed by their orientation. For example, UNI-XY refers to the sample printed by unidirectional printing, with its surface normal to the building direction.

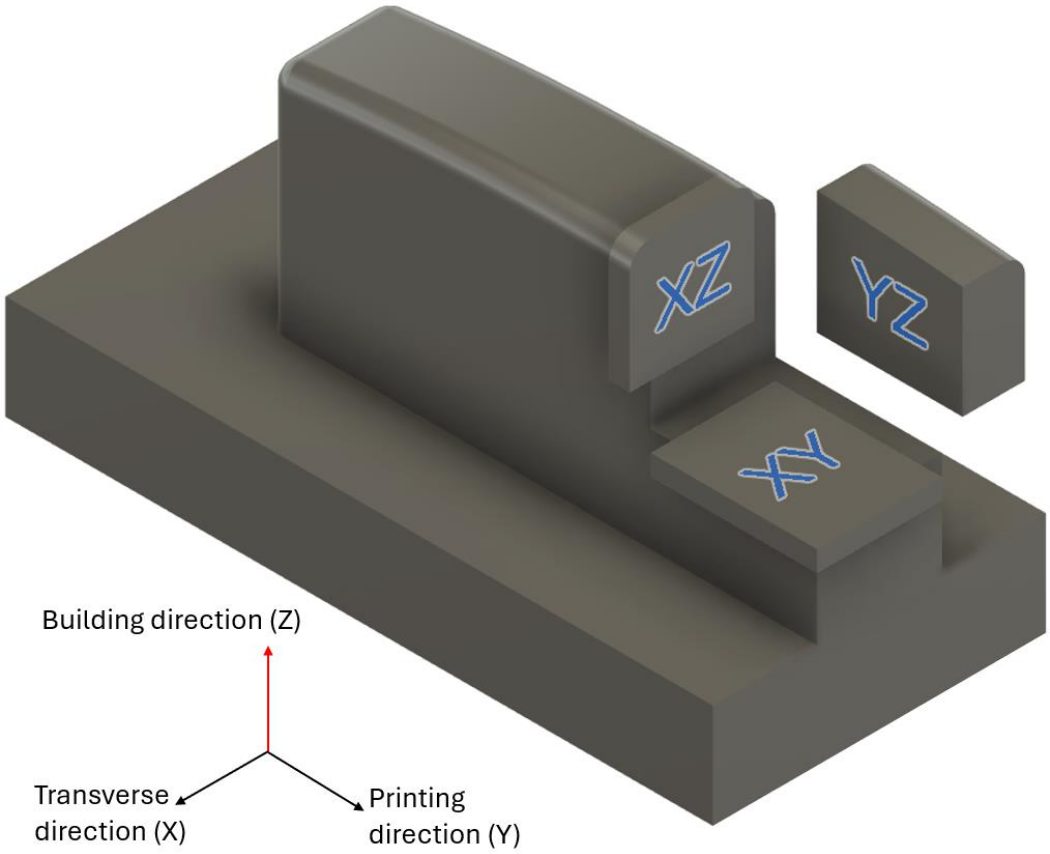

Figure 33 Three microscopy samples cut from WAAM blocks, orientation, and labeling of the samples relate to the defined coordinate system.

4 Pattern Characteristics

This Chapter discusses the results from in-situ measurements during printing, including thermal profile and current and voltage, and the characteristics of the printing pattern through average layer thickness, substrate distortion, and surface quality.

4.1 Thermal Profile

The thermal profile experienced by the substrate and by the layers is measured with a K-type thermocouple and thermal camera VarioCAM HD, respectively. The thermal profile and thermal cycles during WAAM affect residual stress, solidification, and the microstructure evolution, and could provide information to explain results found in microstructural characterization and mechanical testing.

The thermal profile of the substrate is measured as the substrate surface's temperature at the middle of the printing path. Figure 34 shows the thermal profile of the substrates during the first two hours of printing. Note that the temperature spikes induced by the welding process with the arc traveling directly next to the thermocouple, and these peaks should not be interpreted as the temperature experienced by the bulk of the substrate. The measurement by the thermocouple is also localized and cannot represent the bulk of the substrate. Each peak represents the temperature change during the printing and cooling of a single layer. Due to the difference in the required cooling time, some printing patterns have more peaks, hence more layers printed during the first two hours than the others.

As mentioned before, the six printing patterns exhibit similar thermal profiles in groups of two, with unidirectional and bidirectional printing, rectangular and zigzag weaving, and triangular and circular weaving having similarities in printing path. The simple line printing patterns both have lines going from one side to the other side of the substrate, with the first line directly next to the thermocouple and the last line furthest away from the thermocouple, and vice versa for the subsequent layer since the printing path is rotated by 180°. Therefore, the peaks repeat every two layers, and temperature spikes are measured when the line is closest to the thermocouple. They also have a similar deposition rate and average layer thickness, discussed later in Chapter 4.3.

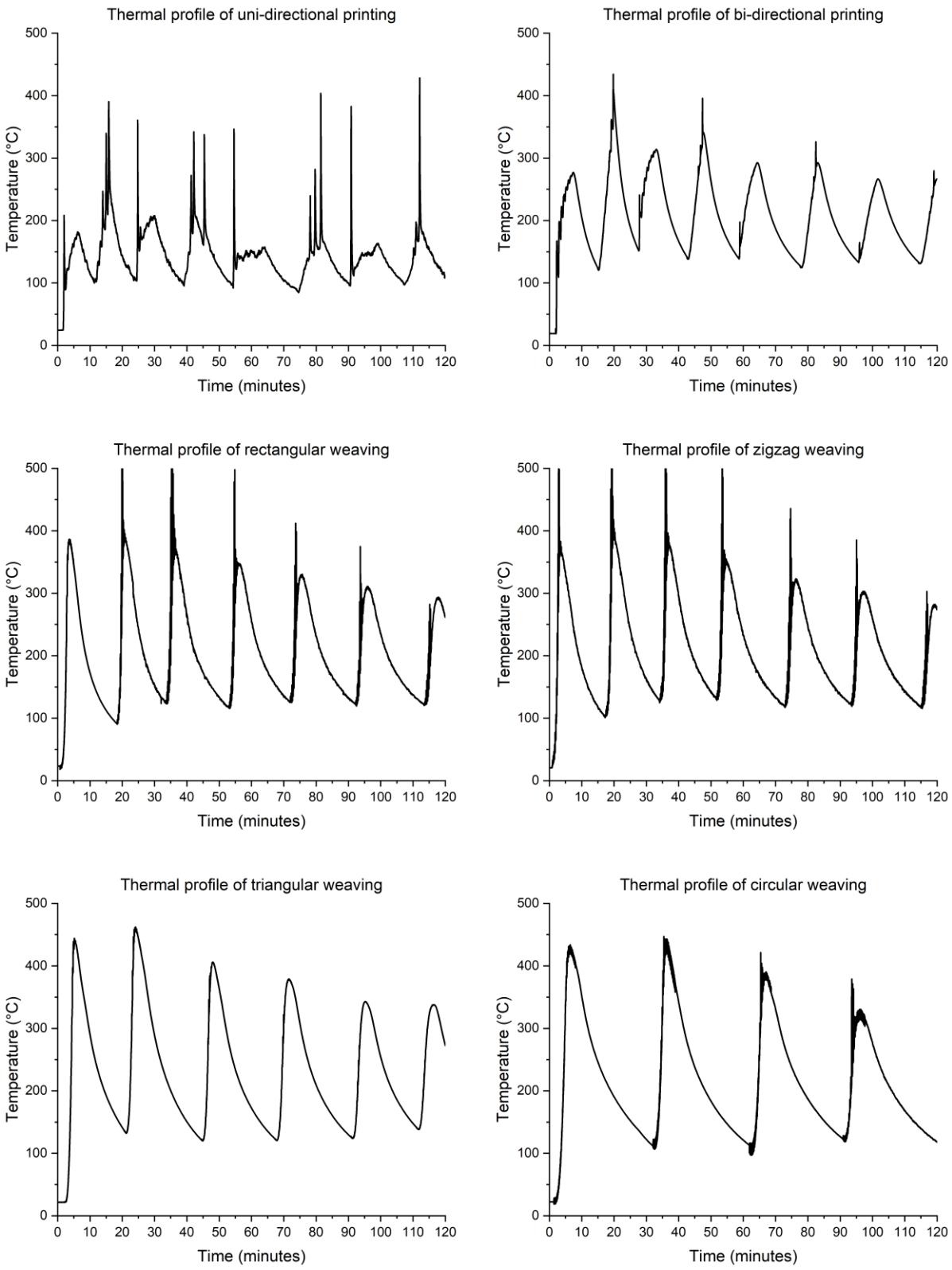

Figure 34 Thermal profile at the substrate surface of the six printing patterns: (a) Unidirectional printing; (b) Bidirectional printing; (c) Rectangular weaving; (d) Zigzag weaving; (e) Triangular weaving; (f) Circular weaving.

The thermal profile of rectangular and zigzag weaving is similar in terms of maximum temperature in each layer and cooling time. Triangular and circular weaving however have higher maximum temperatures and much longer cooling times, due to their high degree of printing path overlap causing excessive heat accumulation. All weaving patterns have an oscillating thermal profile due to the welding torch repeatedly approaching and receding from the thermocouple.

Figure 35 shows an enlarged view of the first layer's thermal profile. Each small peak represents the temperature change induced by one repeating unit of the weaving pattern. Unidirectional and bidirectional both show much lower and delayed maximum temperatures compared to the weaving patterns, peaking when the last line is printed. All the weaving patterns have a much more rapid increase in temperature, peaking halfway through the layer when the printing path is closest to the thermocouple.

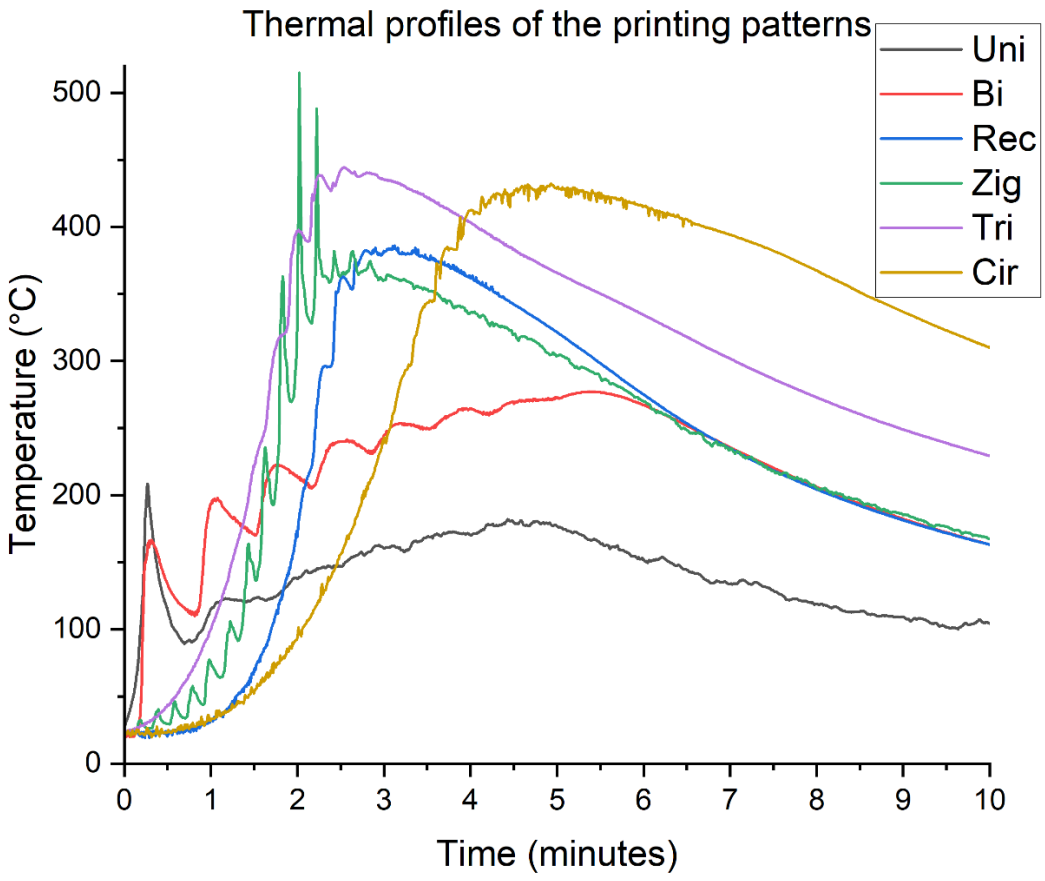

Figure 35 First layer's thermal profile of the six printing patterns.

The thermal camera is used to measure the thermal profile of the 10th layer's surface during printing. The emissivity of 1 is used after comparing temperature measurement at the substrate with thermocouple measurement. Note that the measurement depends on the emissivity setting and could vary across different locations of the WAAM block. The measurement is especially distorted by the arc. The top and bottom half of Figure 36 show the thermal profile halfway along the layer and at the end of the layer, respectively. Note that the temperature profiles at the location of the arc indicated by the arrows are inaccurate since their temperature exceeds the thermal camera's calibration.

The thermal profile of the layer surface shows similar trends to thermocouple measurements of the substrate. For unidirectional and bidirectional printing, there is a small area of high-temperature thermal gradient around and trailing the welding torch. For the weaving patterns, their thermal profiles are similar, with a high-temperature thermal gradient trailing the welding torch and permeating through the WAAM block, extracting the heat towards the aluminum printing platform. There is no major difference between the sides and the center of the printing path.

The cooling rates of the printing patterns are estimated by the time difference between 850 °C and 700 °C, and 700 °C and 500 °C at the center of the layer, as shown in Table 8. An upper-temperature range of 850 °C is chosen because a higher temperature would be within the arc region, and the measurement would be inaccurate. The cooling rates are divided into two temperature ranges because the cooling rate is significantly different between these two ranges. Unidirectional and bidirectional printing both have the highest cooling rate between 850 °C and 700 °C at 112.5 °C/s, and the weaving patterns have significantly lower cooling rates due to excessive heat accumulation. Circular weaving has an exceptionally low cooling rate, due to its printing path repeatedly overlapping the previously deposited material.

Table 8 Cooling rates (°C/s) of the six printing patterns.

Temperature range	Unidirectional printing	Bidirectional printing	Rectangular weaving	Zigzag weaving	Triangular weaving	Circular weaving
850-700	112.5	112.5	13.0	13.8	9.3	3.3
700-500	33.3	24.0	6.1	4.6	3.9	0.9

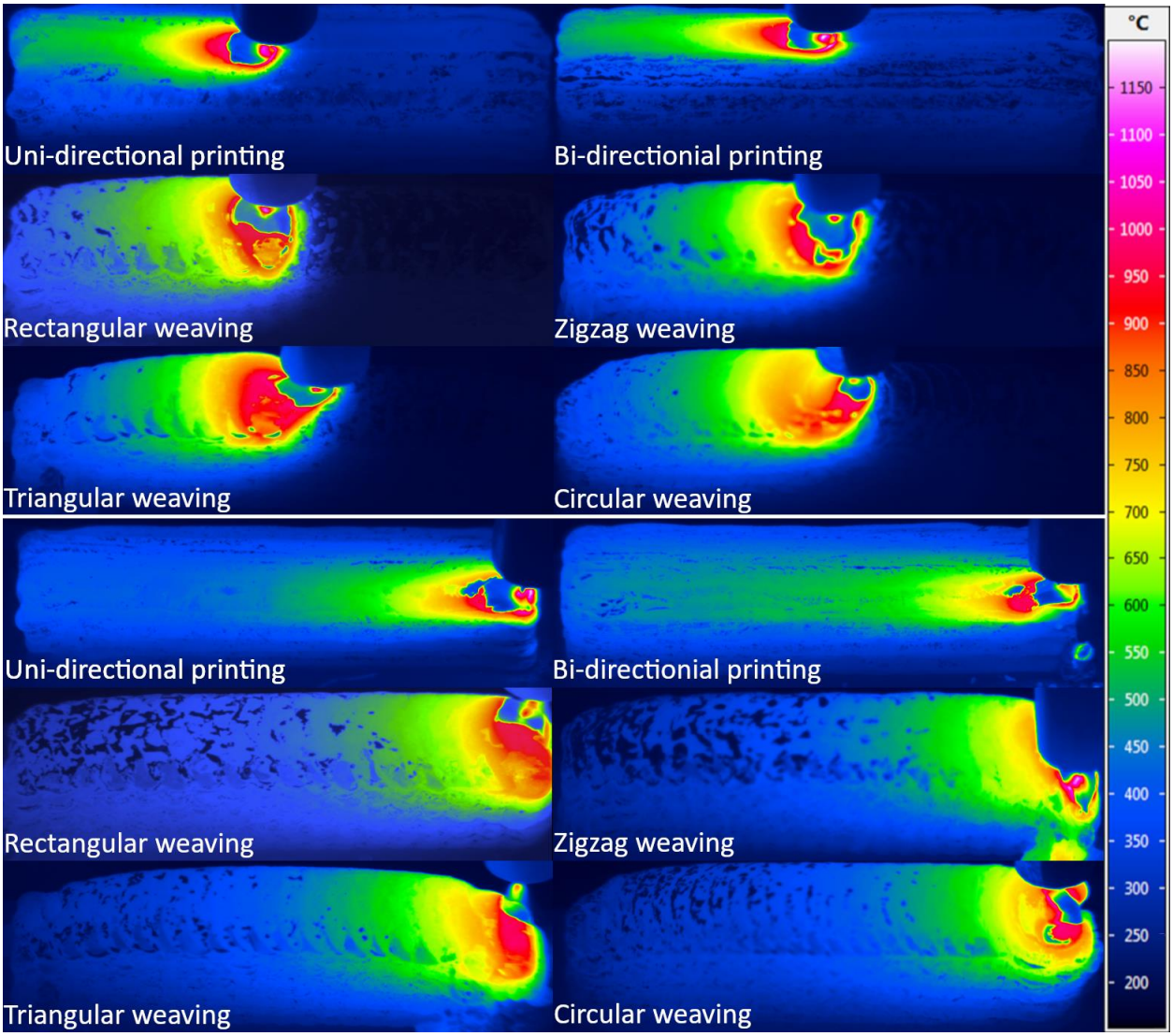

Figure 36 Thermal camera measurement with temperature scale on the right. The top six images show the thermal profile halfway through the layer, and the bottom six images show the thermal profile at the end of the layer. The location of the arc is depicted by the arrows.

Thermal camera images are also used to extract line thermal profiles in the transverse direction across the layer. Line measurements are placed to intersect with a part of the layer with a maximum temperature of 700 °C at the center of the layer. Figure 37 shows the thermal profiles of the six printing patterns from the edge to the center of the layer in the transverse direction. The weaving patterns show a much more uniform transverse thermal profile than line printing patterns, due to their higher degree of heat accumulation. Their temperature at the side also remains much higher.

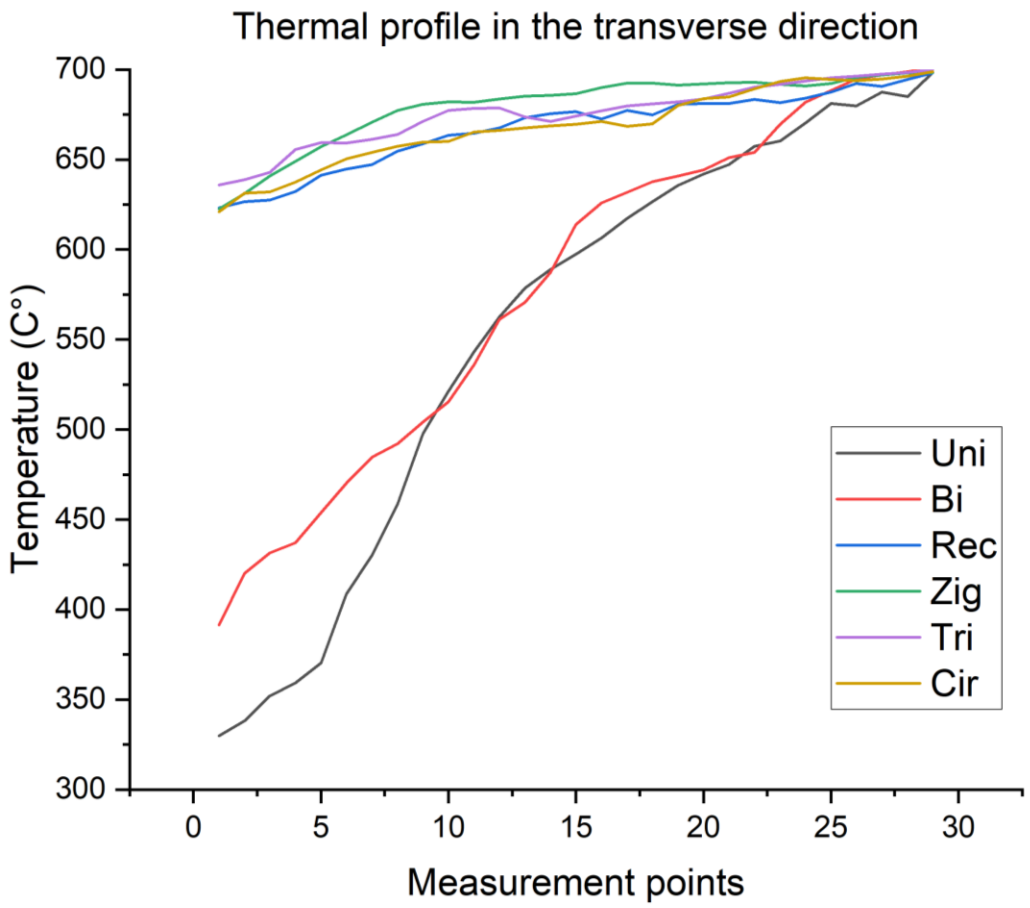

Figure 37 Transverse thermal profile of the six printing patterns.

4.2 Current and voltage

The average current and voltage are measured during printing. Figure 38 shows the average current and voltage during printing measured every 5 layers. The deviation of current and voltage is within the typical range compared to the ranges mentioned in the literature [71]. Overall, the deviation of current and voltage shows no correlation with surface quality. However, a decreasing current is observed in triangular weaving and circular weaving, which could be related to an increasing distance between the welding torch and the surface.

For triangular weaving, the effect of collapse accumulates and the distance between the welding torch and the surface at the beginning and the end increases across the layers. This increases the arc length, which reduces current. For circular weaving, the 6-axis robot is used, and the distance that the welding torch is raised after each layer is pre-programmed and not adjusted per layer manually. The value set from initial testing might be slightly larger than the layer thickness, making

the distance between the welding torch and the surface larger at higher layers. This also causes the arc length to increase, subsequently reducing the current. The two different welding systems used in these two printing patterns might then adjust the voltage differently.

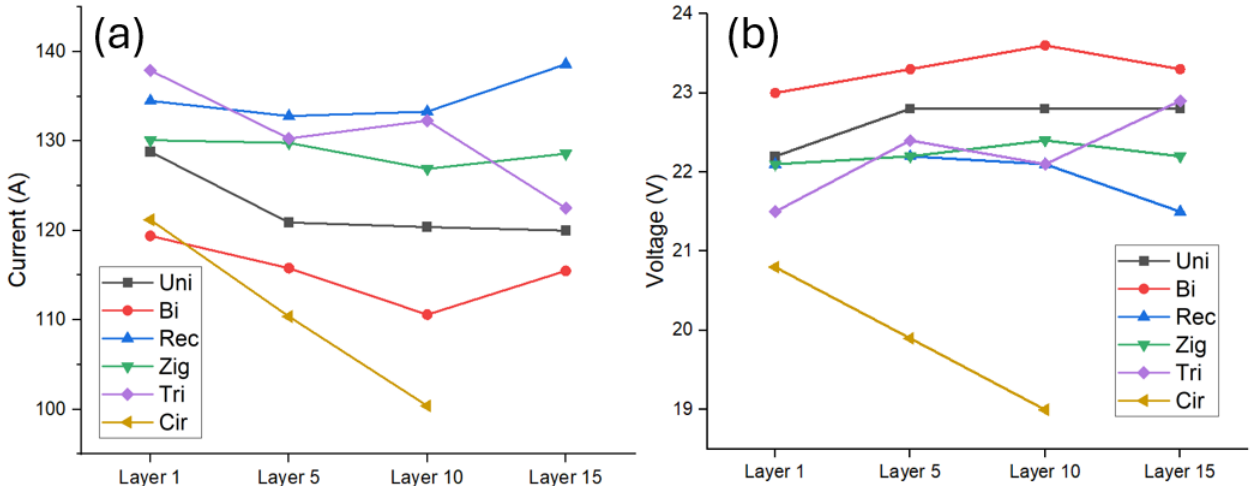

Figure 38 Average current (a) and voltage (b) during printing across layers for different printing patterns.

4.3 Deposition rate

The deposition rate of each printing pattern is shown in Table 9. It is calculated by measuring the effective volume of the WAAM blocks, which excludes the side wall collapse and macro-defects, divided by the average time from start to finish of a layer. This time interval does not take air cooling time into account, because when used in manufacturing active cooling can be employed at lower temperature ranges without affecting microstructure and mechanical properties. Unidirectional printing has the lowest deposition rate since between each weld the welding torch needs to return to the starting position. It also takes time for the arc to be reignited and the shielding gas to pre-flow. Bidirectional printing also has similar issues but with shorter welding torch travel between each weld. Weaving patterns all have similar deposition rates that are superior to line printing patterns. Triangular weaving has the lowest deposition rate out of all weaving patterns since it has the highest amount of side wall defects, which reduces the effective volume.

Table 9 also shows the average layer thickness of each printing pattern, which indicates the degree of printing path overlap. Printing patterns such as triangular weaving and circular weaving have the highest average layer thickness, due to their high degree of direct printing path overlap, lowering their cooling rates and increasing their natural cooling time.

Table 9 Average layer thickness of the six printing patterns.

Printing pattern	Deposition rate (kg/h)	Average layer thickness (mm)
Unidirectional printing	1.88	3.2
Bidirectional printing	1.97	3.8
Rectangular weaving	2.28	3.8
Zigzag weaving	2.28	3.9
Triangular weaving	2.21	4.1
Circular weaving	2.32	6

4.4 Substrate distortion

Residual stress from non-uniform thermal cycling during printing is partially released in the form of distortion. Substrate distortion is measured by the height difference in building direction between the sides and the middle at the bottom of the substrate, shown in Table 10. Overall, the degree of distortion between the printing patterns is similar. The degree of distortion is also relatively low, due to the high stiffness of the thick plates used as substrate.

Table 10 Degree of substrate distortion of the six printing patterns.

Printing pattern	Substrate distortion (mm)
Unidirectional printing	1.77
Bidirectional printing	1.60
Rectangular weaving	1.45
Zigzag weaving	1.71
Triangular weaving	1.59
Circular weaving	1.43

4.5 Surface quality

Surface quality is an important factor in additive manufacturing since it affects the usable volume of the print. A rough and wavy surface requires more time and effort for postprocessing and machining and increases the waste of material. To evaluate the surface quality of different printing patterns, CAD models of the six WAAM blocks are made with the 3D scanner Artec Space Spider, which is used for the distance mapping function in software Artec Studio 17, a software for

processing and evaluation of 3D scanning data. Distance mapping calculates the distance between a pre-defined plane and every point on the side wall of the WAAM blocks, with the pre-defined plane representing the lowest point of the side wall profile, set to intersect with the majority of the concave spots in the side walls. Figure 54 shows the distance maps of the WAAM blocks. Note that some gaps are present in the distance maps because the reference plane is set to accommodate the majority of points on the side walls, and the few outliers that are significantly concave are neglected.

Unidirectional printing has the least average side wall distance and a small distance deviation out of all six WAAM blocks, indicating good surface quality. This is due to the long periods of cooling in between each line reducing heat accumulation and mobility of the molten material. Contrary, bidirectional printing has more heat accumulation, leading to higher mobility of the deposited material during solidification, which results in a less uniform side profile and higher average distance. Defects like spatter and collapse at the end of the lines are also captured in the 3D scans, which are typical macro defects caused by low heat dissipation [5].

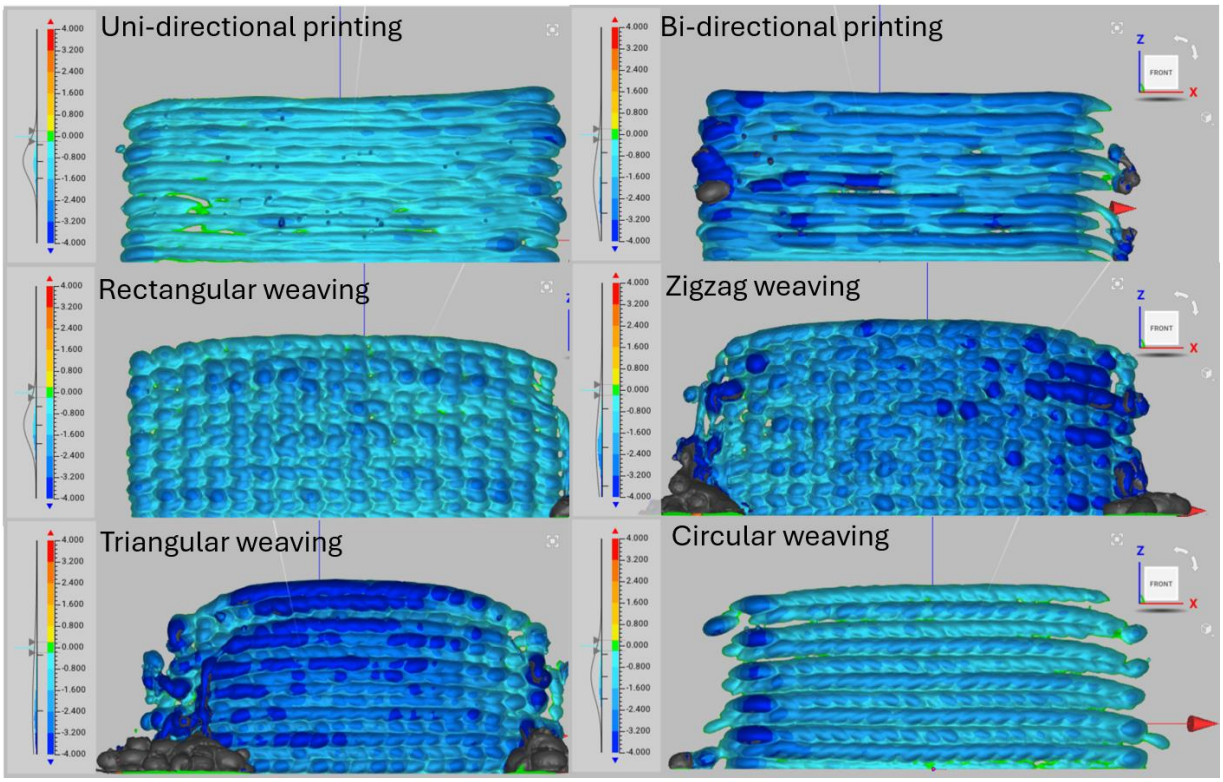

Figure 39 Distance mapping of the six WAAM blocks' side profiles.

For the weaving patterns, rectangular weaving demonstrated the least wavy side profile, followed by circular weaving, with a smoother surface at the center of the side wall than rectangular weaving, but worse at the ends due to the irregularity of ellipse overlap at the beginning and the end. The small ellipse added to compensate for the gap at the beginning causes the beginning of each layer to protrude.

Zigzag weaving has similar surface quality to rectangular weaving in the center but is significantly worse at the ends due to collapse. This is because the printing pattern is rotated by 180° each layer, and the printing path between layers does not overlap completely. The V-shaped angled lines at the beginning and the end of the layers cannot provide a flat stable surface for the next layer to be deposited on. Triangular weaving has a similar issue, with severe collapses due to the triangular shape of the ends, shown in Figure 40. Collapsing at the end of a layer also affects the next layer, worsening the surface quality continuously. It also has a more direct overlapping of the printing path, leading to more heat accumulation and worse surface quality. Further optimization of the end of the printing path of zigzag weaving and triangular weaving is required to prevent collapse and improve surface quality.

Figure 40 Collapse at the end of a layer due to the triangular shape in triangular weaving.

5 Microstructural characterization

The microstructure of the samples is investigated through optical microscopy, electron backscatter diffraction (EBSD), and x-ray diffraction (XRD). Optical microscopy is used to show the general grain structure and grain alignment, as well as fusion zone boundaries, while EBSD is used to further accurately characterize microstructure and texture more locally. XRD is used to investigate texture in a larger area at different locations of the samples.

5.1 Optical Microscopy

The effect of the six printing patterns on the microstructure is evaluated through optical microscopy. Micrographs of the prepared samples in three cross sections are taken with a digital microscope Keyance VHX 7000N. Macro shots are taken by using the stitching function of the digital microscope. Smaller micrographs taken with a magnification of 50× are stitched together to obtain a high-resolution image of the whole sample. To increase the visibility of the micrographs and minimize the effect of glare from stitching, their color curve, brightness, and contrast have been adjusted.

The micrographs of the transverse cross-section XZ are shown in Figure 41. The boundaries of the fusion zones can be observed. UNI-XZ and BI-XZ have the typical U-shaped fusion zones from individual weld beads, and the weaving patterns have horizontal lines across the samples from their unique printing paths. Notably, TRI-XZ shows a combination of both horizontal and U-shaped fusion zone boundaries, with the horizontal part from the base of the triangle and the U-shaped part from intersections of the printing path. In terms of lack-of-fusion defects, UNI-XZ has lack-of-fusion defects at the outer welds with poor side wall surface quality, and BI-XZ has lack-of-fusion defects at the last weld of each layer. This is because the uneven and curved surface makes it difficult for the weld to fully penetrate. The weaving patterns show no lack-of-fusion defects due to their printing path with high coverage.

In terms of grain structure, all samples have large and elongated columnar grains. For the grains in the center of the samples, UNI-XZ has some grains aligned in the build direction and some that are rotated. BI-XZ has an abundance of grains with a large degree of rotation in alternating directions across the layers. The rotation of the grains is due to the heat accumulation from the previous deposited lines changing the direction of the thermal gradient, and the alternating grain

rotation is because the sequence of lines printed is reversing each layer from the 180º printing path rotation.

The weaving patterns on the other hand show a high degree of grain alignment with the building direction across a wide range of the sample. This suggests that the weaving patterns induce a more uniform thermal gradient across the transverse direction. The grain rotation at the sides of the samples is also more limited for the weaving patterns compared to the line printing patterns.

The micrographs of the longitudinal cross-section YZ are shown in Figure 42. The shape of the fusion zone boundaries is reversed for the line printing patterns and weaving patterns. Outlines of fusion zones are observed in UNI-YZ and BI-YZ, while the typical U-shaped fusion zones are present in the YZ cross-sections of the weaving patterns, due to their unique printing paths that intersect with the YZ plane. An inclusion at the fusion zone boundaries is observed in CIR-YZ, indicated by the arrow. In this cross-section, the grains of UNI-YZ are in alignment with the building direction, while grains in BI-YZ are slightly rotated in alternating directions between layers. The weaving patterns all have grains that fan out between fusion zones. This pattern is also typical in the mentioned literature where grains tend to be perpendicular to the fusion zone boundaries [35].

The top view cross sections XY, shown in Figure 43 show fusion zone boundaries that resemble the top view of the printing patterns. For the line printing patterns, straight lines of fusion zone boundaries are observed. The fusion zone boundaries of ZIG-XY are especially apparent, in repeating V shapes. REC-XY's fusion zones are not apparent but resemble ZIG-XY's due to their similarity in printing path. For TRI-XY, parts of the sides and base of the triangles can be seen. Fusion zone boundaries in circular shapes are also shown in CIR-XY.

In terms of grain size and grain orientation, most XY cross-sections show finer and more equiaxed grains, because this is the transverse cross-section of the columnar grains. BI-XY has more elongated grains due to its high degree of rotation of columnar grains, resulting in a more tilted cross-section.

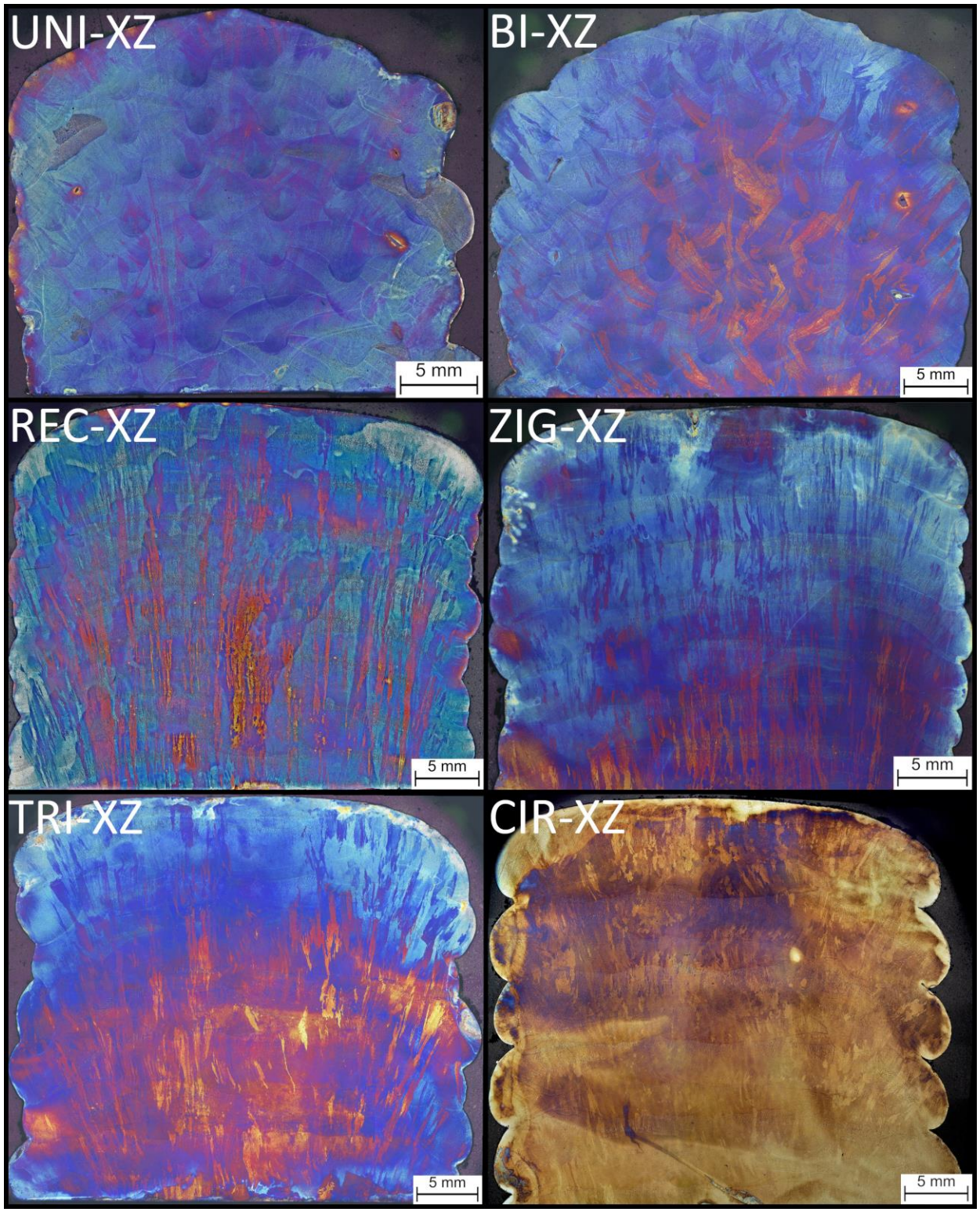

Figure 41 Micrographs of the XZ cross-section of the six WAAM blocks.

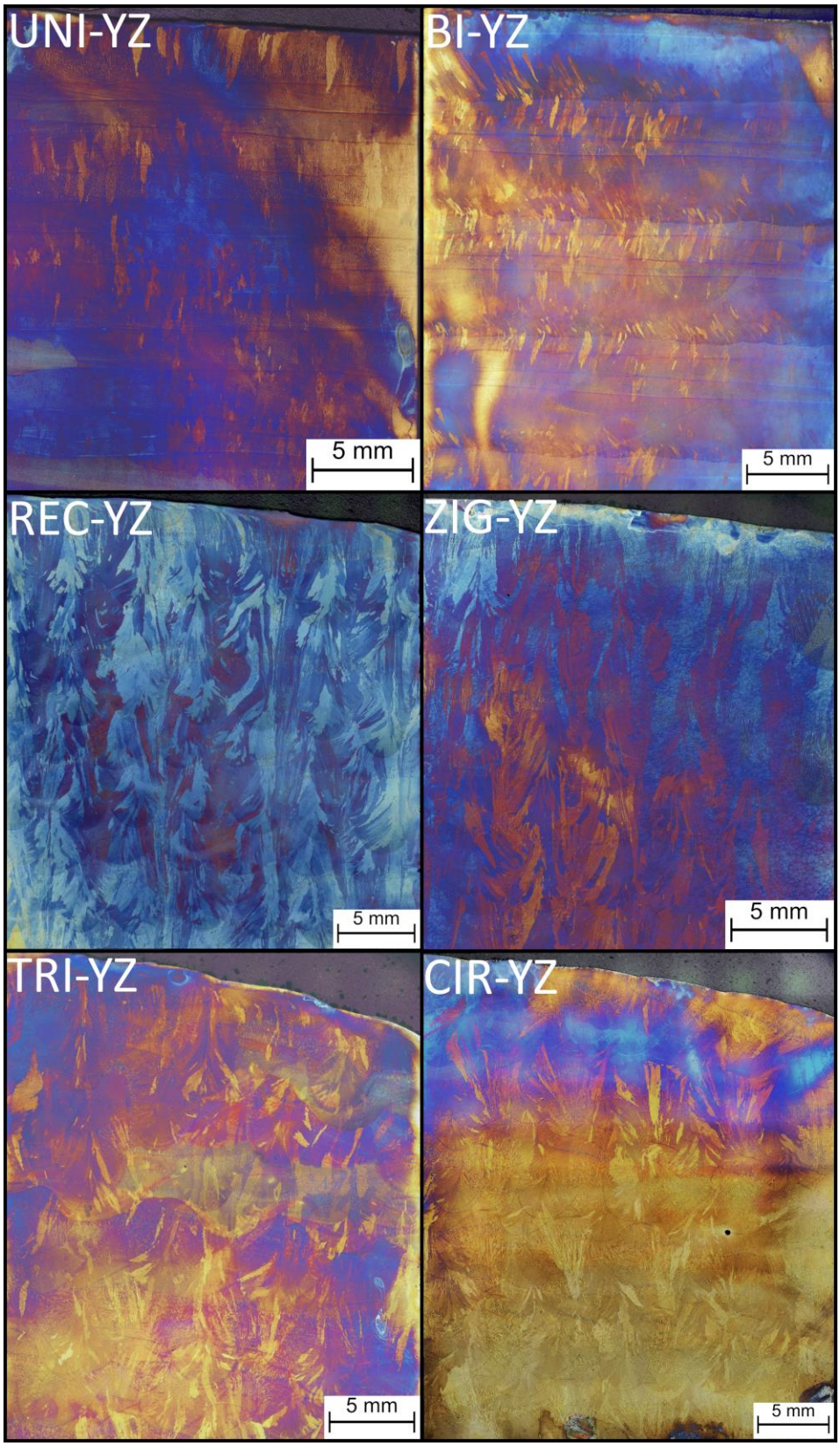

Figure 42 Micrographs of the YZ cross-section of the six WAAM blocks.

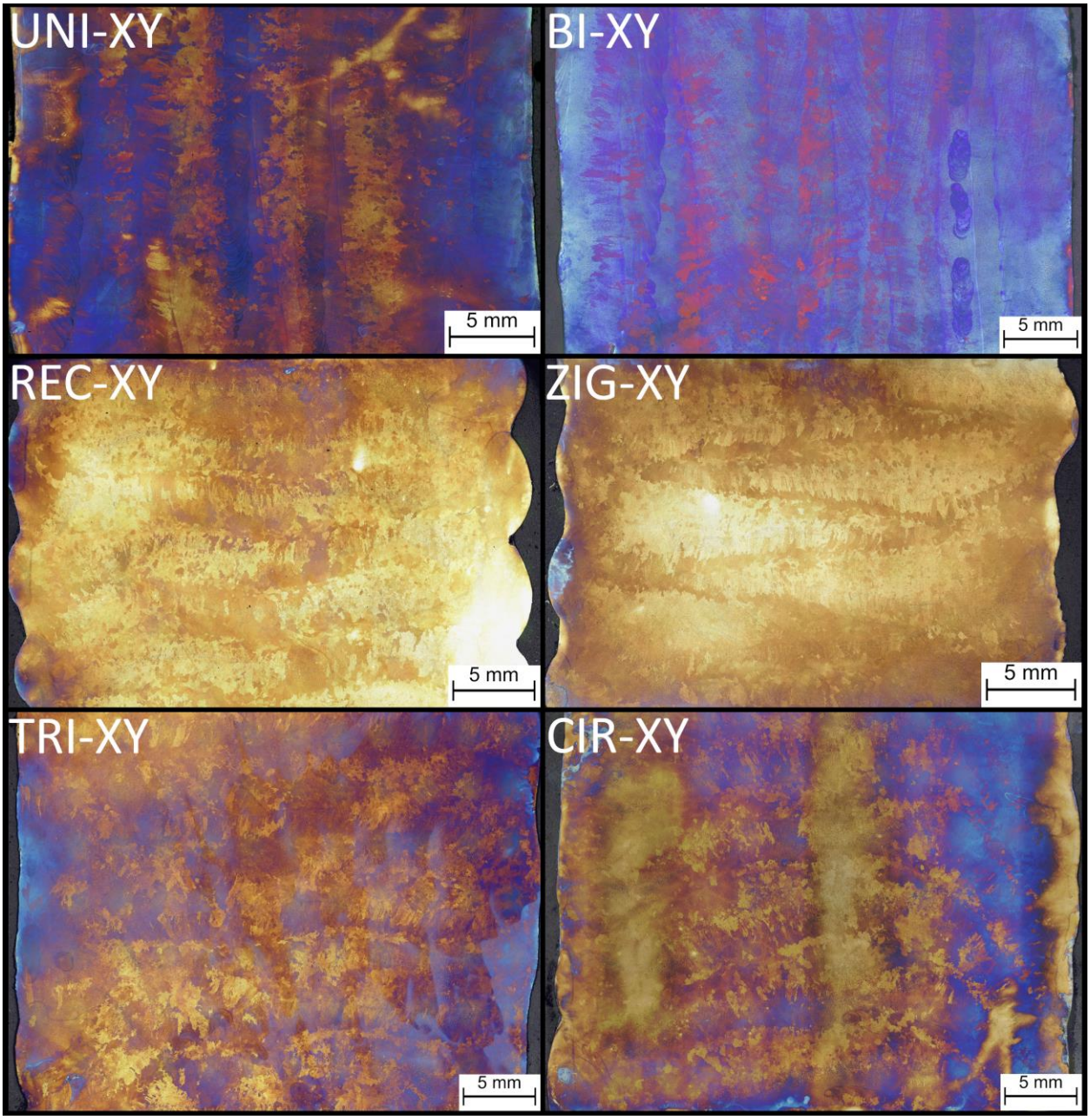

Figure 43 Micrographs of the XY cross-section of the six WAAM blocks.

5.2 Electron backscatter diffraction

The grain structure and crystal orientation in the samples are analyzed by obtaining inverse pole figure (IPF) maps through electron backscatter diffraction (EBSD). UNI-XZ and TRI-XZ are selected for comparison since they have the highest and lowest average hardness respectively, discussed later in Chapter 6.1. The IPF maps are obtained by stitching multiple 2 mm × 1 mm scans together with MIST, a stitching plugin for ImageJ [72,73]. Note that due to the limitations of EBSD, distortion at the sides of the scans causes imperfections and seams in the stitched image. For each sample, an IPF map at the center and the side of the cross-section is obtained. The orientation of the grains is indicated with respect to the building direction.

Figure 44 shows the IPF map of UNI-XZ, containing both the center and the side of the sample. It can be seen that even at the center of the sample, there are grains that are not entirely aligned with the building direction but rotated outwards due to the non-uniform thermal gradient across the transverse direction. This is also observed in X-ray diffraction (XRD), later discussed in Chapter 5.3. A part of the zigzag-shaped layers of grains, previously seen in optical microscopy can be seen at the left edge of the IPF map. There are also regions of fine and less elongated grains, likely to be the fusion zone boundaries. On average, the grains have a grain size of 89.9 ± 134.7 μm and an aspect ratio of 0.428 ± 0.184. The large standard deviation of the grain size is due to the mix of coarse columnar grains and regions of fine grains in fusion zone boundaries. A larger scan area, especially in the building direction is required to include enough different regions of grains to obtain a certain grain size.

Figure 44 IPF maps of UNI-XZ with respect to the building direction. The diagrams on the left show the location of the scans on the TRI-XZ sample and the color scale of the IPF map with respect to the building direction.

Figure 45 shows the IPF maps of TRI-XZ, containing both the center and the side of the sample at the top and bottom maps, respectively. At the center of the sample, the grains are highly aligned to the building direction, with a strong <1 0 0> texture. Towards the side of the sample, the grains start to rotate outward with the thermal gradient, but the rotation is limited compared to the grains at the side of UNI-XZ. The strong grain alignment to the thermal gradient throughout the sample suggests that the thermal gradient is more uniform in the transverse direction, as seen in Figure 37. The fusion zone boundary can be seen with a band of less elongated and finer grains across the center and the side of the sample. In terms of grain size and aspect ratio, TRI-XZ has a grain size of 91.3 ± 129.2 μm and an aspect ratio of 0.454 ± 0.172, which is comparable to UNI-XZ. The grain size also has a large standard deviation due to the same aforementioned issue in UNI-XZ, none the less they have a similar distribution of fine grains and coarse columnar grains. The grain size distribution of UNI-XZ and TRI-XZ is shown in Figure 46, and a bimodal distribution can be seen.

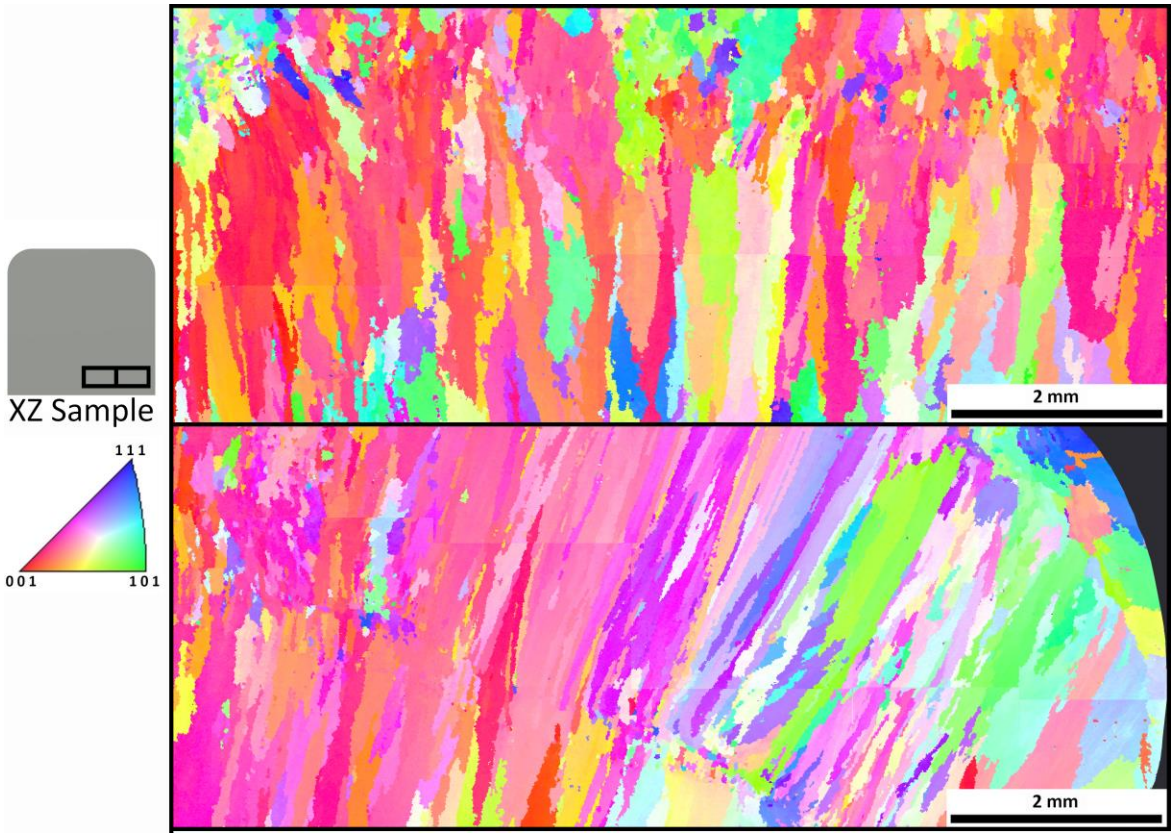

Figure 45 Center (top) and side (bottom) IPF maps of TRI-XZ with respect to the building direction. The diagrams on the left show the location of the scans on the TRI-XZ sample and the color scale of the IPF map with respect to the building direction.

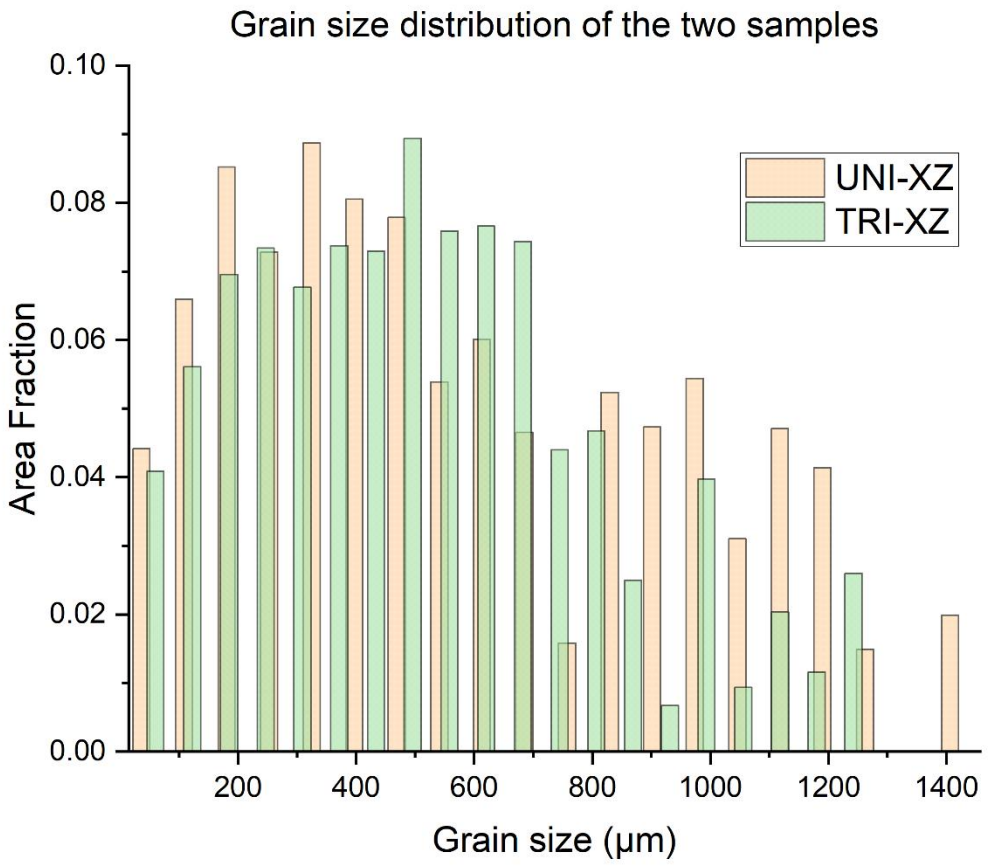

Figure 46 Grain size distribution of UNI-XZ and TRI-XZ in area fraction.

5.3 X-ray diffraction

The printing pattern's effect on modifying texture through changing the direction of heat extraction is shown by measuring pole figures utilizing X-ray diffraction (XRD) with a Bruker D8 Advance. Three pole figures representing (1 1 1), (2 0 0), and (2 2 0) planes are measured on the top view cross-section XY sample. Since the XY plane is normal to the direction of grain elongation, it is the cross-section containing most grains. The samples are scanned at different angles by a rotating rectangular beam. For each sample, the center and the side of the sample are scanned with a large 4 mm × 3 mm beam with a maximum irradiated length of 28 mm, and a small 2 mm × 1 mm beam with a maximum irradiated length of 11 mm size, respectively. A large beam size is preferred to increase the number of grains covered, but to investigate the texture of the side walls a smaller area is needed. Figure 47 shows the pole figure for the center of the XY samples, with the pole figure orientation with respect to the samples shown in the bottom left.

As expected, all samples show similarity in terms of the orientation of the (2 0 0) plane, with different degrees of scattering and misalignment. As discussed, <1 0 0> is the preferred growth direction of FCC crystal structure to minimize energy, and this direction is aligned with the direction of the largest heat extraction, as discussed in Chapter 2. Therefore, in the center of the sample, it is expected for this direction to be aligned with the build direction. There are high intensities clustered and scattered throughout the pole figures, indicating the presence of highly oriented grains.

For unidirectional and bidirectional printing, there are intensities aligned to the center of the (2 0 0) pole figure, and related intensities on the (1 1 1) and (2 2 0) pole figures located according to crystallographic relationships. In (2 0 0) of unidirectional printing, there are also intensities above and below the center, due to the rotated grains from the steep thermal gradient in the transverse direction, shown in Figure 37. This can also be seen in bidirectional printing, which shows some scattered intensities in the transverse direction. Both printing patterns have intensities in the form of an incomplete ring found in the (1 1 1) and (2 2 0) pole figures, slightly resembling a fiber texture. This indicates that there are more preferred growth directions than only in the build direction, and the direction of the thermal gradient is not perfectly aligned with the build direction.

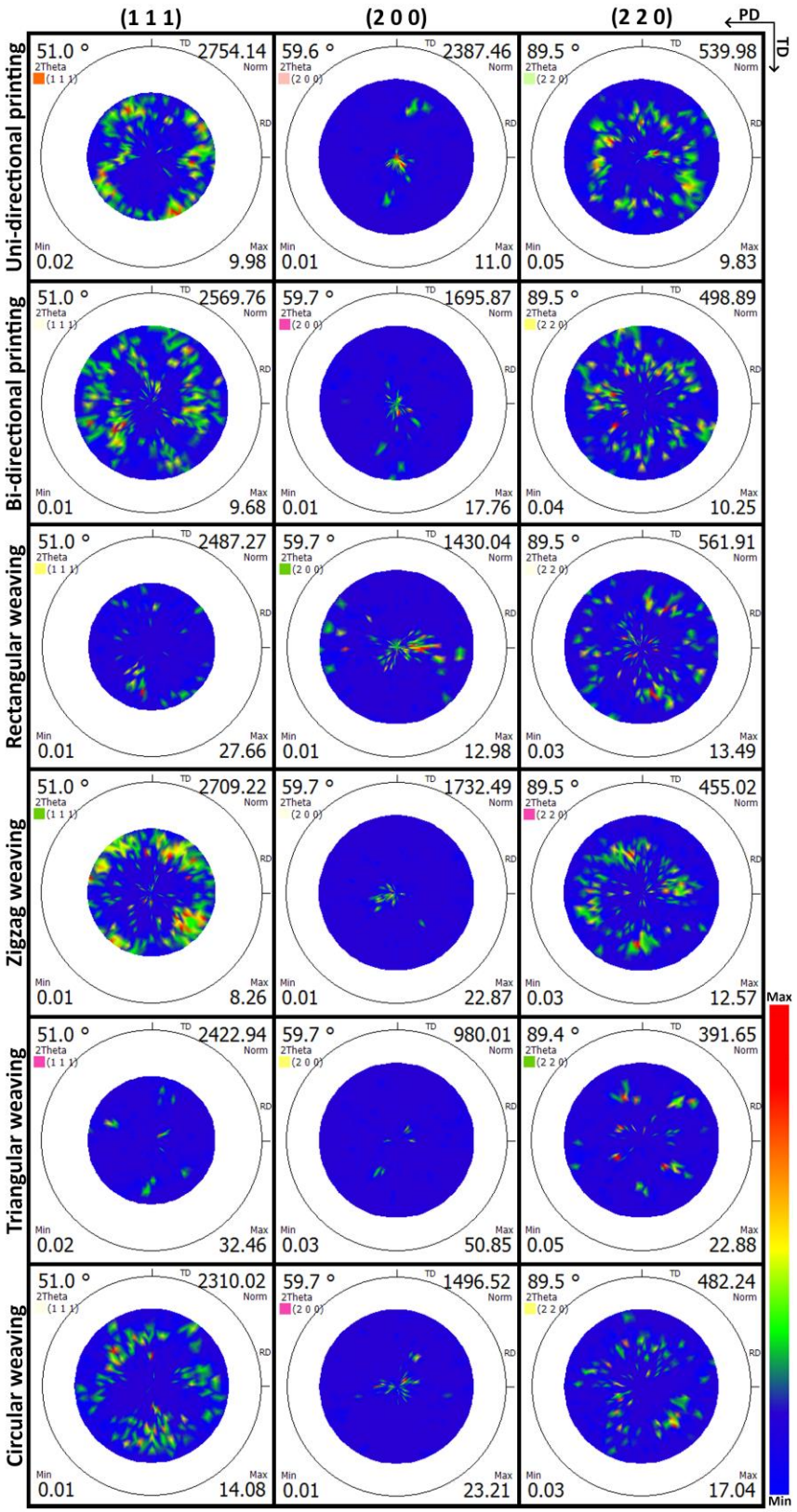

Figure 47 Pole figures of the center of XY samples. The rows represent the (1 1 1), (2 0 0), and (2 2 0) planes, and the columns are the six printing patterns.

For rectangular, zigzag, and circular weaving, the intensities in the (2 0 0) pole figures are much more scattered across the printing direction instead, with rectangular weaving having the most scattered (2 0 0) pole figure. This could be due to the excessive heat accumulation rotating the direction of the thermal gradient away from the depositing part of the layer, consequently changing the direction of solidification. Triangular weaving has the least scattered (2 0 0) pole figure, having a few poles with very high intensity all offset from the center. This could be an indication of highly aligned large grains, formed from repeated remelting. The poles are also offset to different locations from the center, which might be caused by the different directions of the temperature gradient between the sides and the base of the triangles.

The pole figures at the side of the samples are shown in Figure 48. As expected, the intensities in the (2 0 0) pole figure are rotated from the center due to the rotation of the thermal gradient at the side walls. The rotation of the thermal gradient is due to the uneven layer surface, especially at the sides where material has to be deposited onto a sloped surface [35].

In terms of (2 0 0) pole figures, unidirectional printing has two strong intensities rotated to the sides but remains on the vertical axis of the pole figure. Bidirectional has a more scattered intensity below the center, with its components spread out in the same pole figure. For rectangular and zigzag weaving, the intensities are rotated from the center, but less rotated than the pole figures of line printing patterns. This suggests the presence of a more uniform thermal gradient across the transverse direction, which agrees with the grains at the sides of the samples with limited rotation, as seen in optical microscopy. Triangular weaving shows a single spot of strong intensity, with even more limited offset from the center. Circular weaving also has intensities with small rotations from the center but is more scattered than triangular weaving. The reduction of intensity rotation from the center of the (2 0 0) pole figure could indicate that weaving with direct overlapping printing paths achieves an even more uniform thermal gradient direction across the transverse direction.

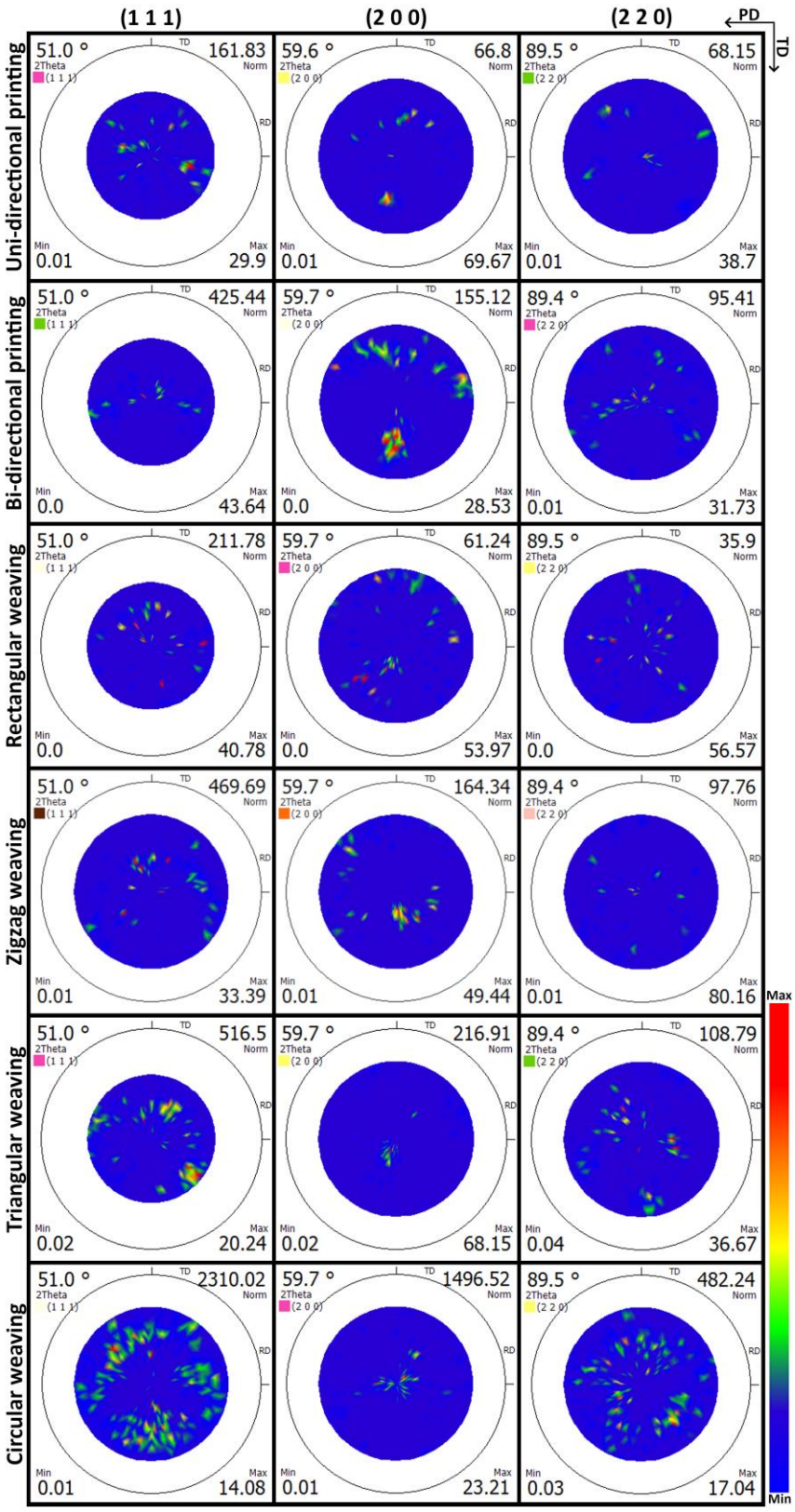

Figure 48 Pole figures of the side of XY samples. The rows represent the (1 1 1), (2 0 0), and (2 2 0) planes, and the columns are the six printing patterns.

6 Mechanical Properties

This Chapter discusses the results from microhardness and tensile testing to investigate the effect of printing patterns on mechanical properties. Microhardness testing is conducted in an attempt to show anisotropy in mechanical properties across different locations of the samples, while tensile testing is used to compare the performance of the printing patterns.

6.1 Microhardness

Microhardness testing is performed to evaluate the effect of printing patterns. It is expected that the different printing patterns affect the cooling rate, hence the grain size and the δ-ferrite content, causing differences in microhardness between the printing patterns. This is because grain size affects yield strength according to the Hall-Petch relation, and a higher δ-ferrite content or a smaller secondary dendrite arm spacing is known to increase hardness [74–76]. The Microhardness of six samples in the XZ samples is measured with a microhardness tester DuraScan. Due to the large grain size, a relatively higher load HV5 is used to cover a larger area of grains with the indent. According to ISO 6507-1 [77], to avoid the effect of work-hardening, a minimum distance of 2.5 × diameter between the indent is used. This is determined to be 0.7 mm after measuring the size of multiple indents.

Initially, a horizontal line scan of microhardness is conducted to investigate the local differences of microhardness across the weld bead in the form of a hardness profile. This is done on the TRI-XY sample, where an intersection between a horizontal weld bead from the base of the triangle and cross sections of weld beads from the sides of the triangle is observed, shown in the form of a non-continuous fusion line with multiple valleys. This is to investigate if there is a local difference in microhardness across different regions of the printing patterns and the fusion lines. Figure 49 shows the fusion line in TRI-XZ and its hardness profile. The hardness profile shows significant noise, and it is difficult to relate it to the intersections of weld beads. This could be because only a few grains are measured by each indent due to the coarse microstructure. Because of the limitation of minimum distance between measurements, a high-resolution hardness profile cannot be obtained. Lowering the force for the hardness measurements is also not ideal since the size of the indentation would decrease and even fewer grains would be covered due to the large grain size.

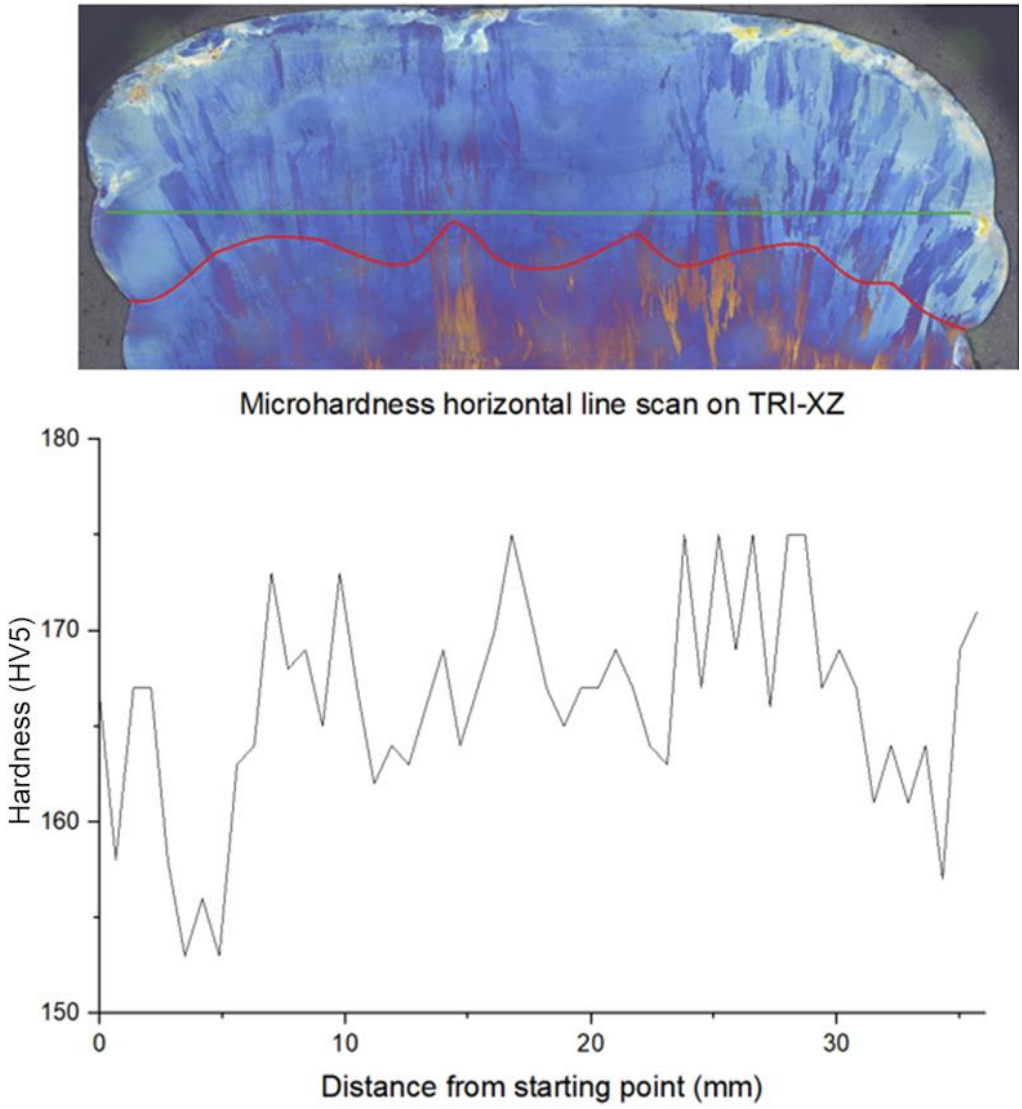

Figure 49 Microhardness line scan across the intersection of weld beads. Top: micrograph of TRI-XZ with the red line indicating the fusion line and the green line indicating the microhardness line scan. Bottom: microhardness plot of the depicted line scan on TRI-XZ.

To investigate the difference in hardness across the layers and between the sides and center of the samples, a hardness line scan across different layers and positions is conducted. For each sample, three horizontal and three vertical lines of indents are applied and measured. The first horizontal line is applied to the last layer, followed by two more with a spacing of two layers between the lines. Similar to the hardness profile in Figure 49, no distinct hardness profile that shows any sign of correlation to the printing path is observed.

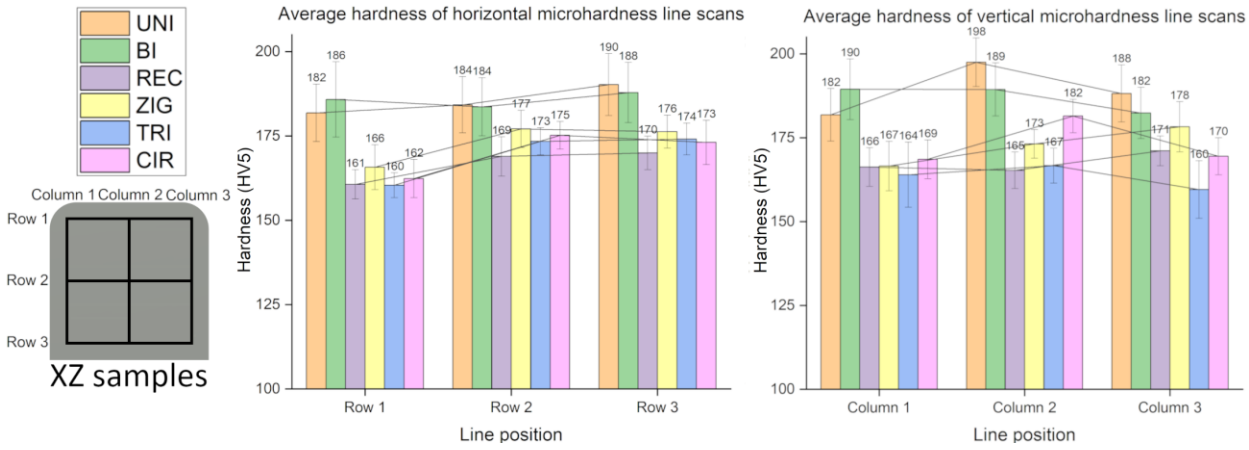

Figure 50 Average hardness value of horizontal (left graph) and vertical (right graph) microhardness line scan across layers. Positions of the line scans on the XZ samples are indicated on the left.

Figure 50 shows the average hardness values of the six samples across the layers. The average hardness value of the weaving patterns is lower than that of unidirectional and bidirectional samples across all three lines.

Notably, for all weaving patterns, the average hardness in the top layer is lower than in the lower layers. This could be due to the potential difference in δ-ferrite from remelting since the final layer does not experience remelting. To estimate the phase fraction of δ-ferrite, the software ImageJ with void content analysis plugin is used. Optical micrographs with vermicular dendrites in the center of the weld bead of each sample in the XZ plane are taken. Vermicular dendrite is chosen because it is the most commonly found dendritic structure in austenitic stainless steel welds, and it has a strong alignment with the direction of heat extraction [78].

The software then processes the image to increase the contrast between the austenite and the δ-ferrite phase, and a threshold of the color range is set manually until only δ-ferrite is selected, as shown in Figure 51. The software then calculates the volume fraction of the selected δ-ferrite. The δ-ferrite content in the top layer and the lower layer for all samples is calculated, and the area fraction is around 13% for all samples across different layers. This might suggest that the difference in hardness is not due to δ-ferrite content. However, the δ-ferrite phase fraction is only a rough estimation, and a more dedicated technique such as selective dissolution analysis is required to draw a definitive conclusion [74].

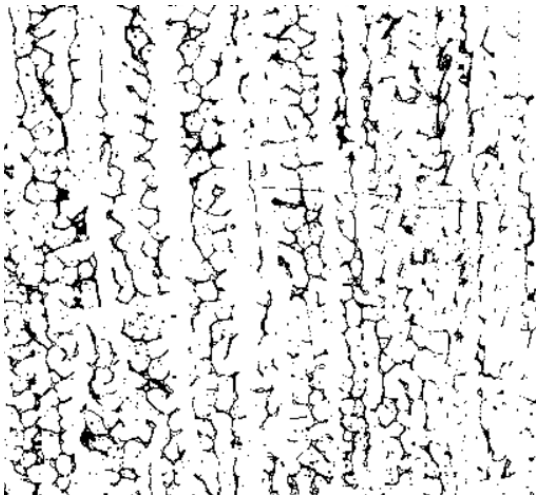

Figure 51 Estimation of δ-ferrite phase fraction by adjusting color threshold in software ImageJ.

For vertical line scans, shown in the right plot in Figure 50, the average hardness of line printing patterns remains higher than that of the weaving patterns, and no specific trend of average hardness value across the samples is observed. Average hardness values of all the hardness line scans are shown in Table 11.

Table 11 Average hardness (HV5) of all hardness line scans.

Sample	Row 1	Row 2	Row 3	Column 1	Column 2	Column 3
UNI	181.9 ± 8.5	184.3 ± 8.4	190.2 ± 9.2	181.8 ± 7.9	197.6 ± 7.2	188.2 ± 8.5
BI	185.9 ± 11.2	183.7 ± 8.6	187.9 ± 8.9	189.5 ± 9	189.4 ± 7.9	182.4 ± 7.6
REC	160.7 ± 4.4	168.9 ± 5.8	170 ± 5	166.3 ± 5.8	165.3 ± 5.4	171.1 ± 4.4
ZIG	165.8 ± 6.7	177.1 ± 5.5	176.3 ± 4.9	166.6 ± 7.4	173.2 ± 4.3	178.3 ± 7.5
TRI	160.4 ± 3.7	173.4 ± 4	174.1 ± 4.7	164 ± 9.7	166.7 ± 5.2	159.6 ± 8.6
CIR	162.4 ± 5.7	175.2 ± 4.1	173.1 ± 6.6	168.6 ± 5.8	181.5 ± 5	169.5 ± 5.5

6.2 Tensile testing

The tensile samples described in Chapter 3.5 are tested with Instron 5500R and with the tensile strain measured by extensometer. Figure 52 shows the tensile curves of all the samples parallel to the building direction. Note that sample BI-BD1 had issues during machining due to residual stress and cannot be used in testing. The variation of the tensile curves between sample 1 to sample 5 of all the printing patterns, which are the samples extracted across the transverse direction, is limited to the end of the curve that shows necking and failure strain. REC-BD5 and CIR-BD2 failed much earlier than the rest of the samples in their printing pattern, and the cause could be stress

concentration from imperfection during machining since they both failed at the shoulder that was milled. In terms of yield strength, ultimate tensile strength, and Young's modulus, samples 1 to 5 of each printing pattern show similar results. This shows that the anisotropy across the transverse direction is limited for all printing patterns.

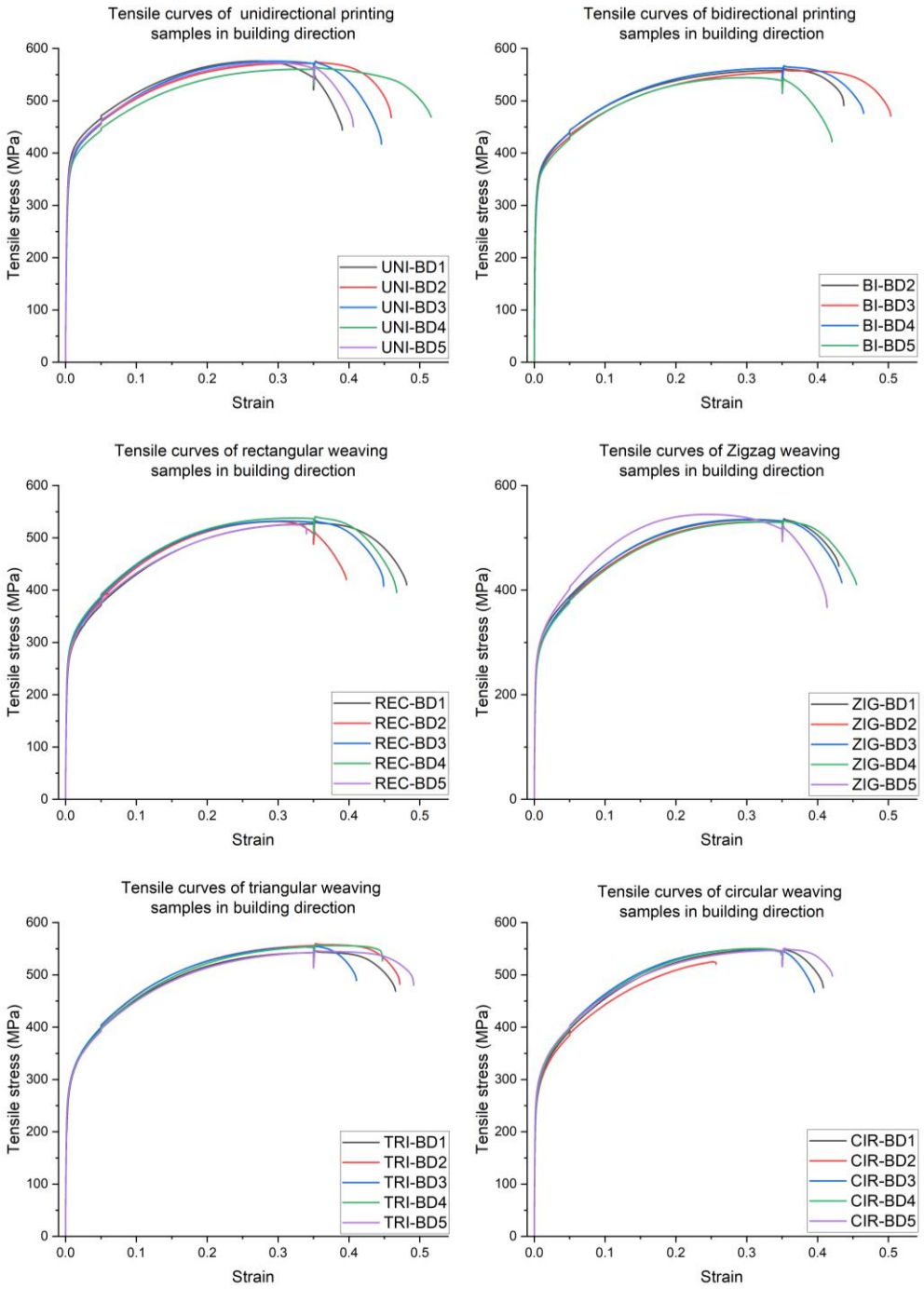

Figure 52 Tensile curves of all the building direction samples.

The averaged tensile curves of the building direction samples are shown in Figure 53, and the averaged tensile properties of the building direction samples are shown in Table 12. Overall, line printing patterns have superior yield strength and ultimate tensile strength than weaving patterns. The tensile properties of the weaving patterns are also similar. Despite having lower yield strength and ultimate tensile strength, the weaving patterns offer no increase in ductility.

Table 12 Averaged tensile properties of all the building direction samples.

	Strain at failure (%)	**Yield strength (MPa)**	**Ultimate tensile strength (MPa)**	**Area reduction (%)**
UNI-BD	44.4 ± 4.9	338.9 ± 7.7	573 ± 4.5	55.2 ± 3.0
BI-BD	45.7 ± 3.6	314.7 ± 7.1	558.1 ± 9.7	55.5 ± 3.2
REC-BD	44.9 ± 2.6	257.3 ± 6.3	533.6 ± 3.5	54.3 ± 2.5
ZIG-BD	43.3 ± 1.1	256.5 ± 7.0	536.1 ± 3.0	54.0 ± 2.5
TRI-BD	45.7 ± 3.1	263.3 ± 4.3	552.8 ± 6.5	46.9 ± 4.6
CIR-BD	40.9 ± 0.9	262.4 ± 7.6	544.2 ± 10.8	53.4 ± 2.3

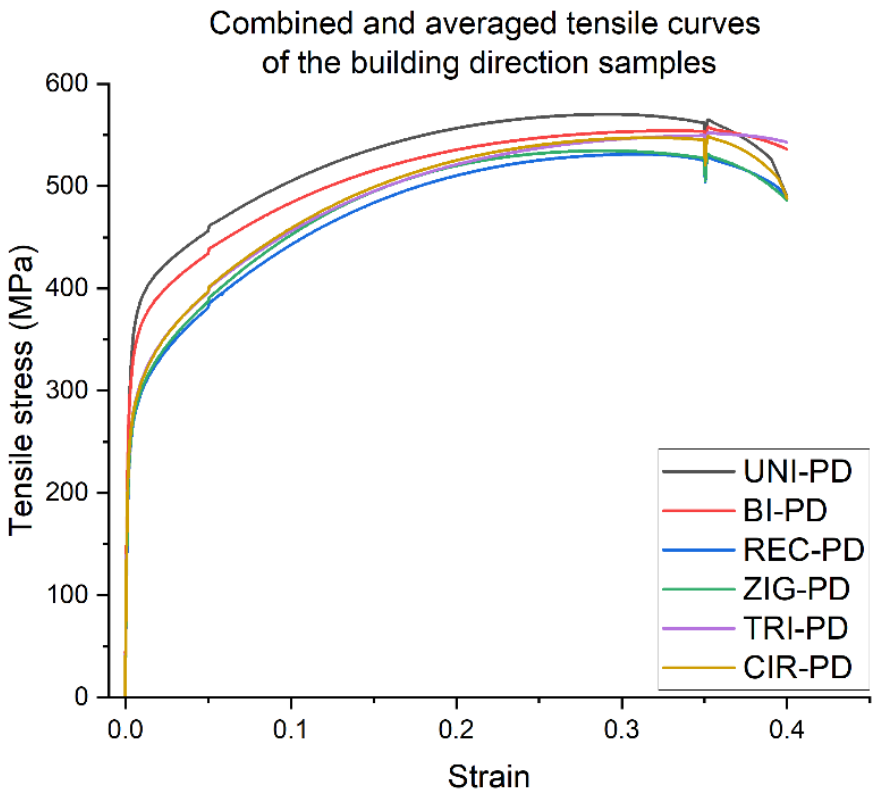

Figure 53 Combined and averaged tensile curves of the six printing patterns in the building direction.

7 Discussion

Six printing patterns were investigated in terms of characteristics, thermal profile, microstructure, and mechanical properties. In this Chapter, a comparison between the printing patterns, the effects of the unique thermal profiles on the microstructure, and the microstructure's influence on mechanical testing is discussed.

Optimization of the printing paths was required to minimize macroscopic and microscopic defects during printing. Optimization consists of finding the suitable printing parameters, followed by adjusting the geometrical variables of the printing path to achieve the optimal weld bead overlaps. However, adjustment of the printing path resulted in different surface quality, affecting the usable volume of the WAAM blocks. Unidirectional printing resulted in the smoothest side wall due to its simple and stable printing paths, but rectangular and circular weaving resulted in similar surface quality despite their intrinsic side wall waviness. For zigzag and triangular weaving, the geometry of the ends of their printing paths resulted in uneven layer thickness, leading to macro-defects such as side wall collapse and spattering, hence resulting in poor surface quality. Further printing path optimization is required to prevent these issues.

In terms of thermal profiles, the weaving patterns demonstrated higher peak temperatures, longer cooling time, lower cooling rates, and more uniform temperature gradients in the transverse direction than line printing. Due to the unique printing paths, weaving patterns have extended periods of local heating, leading to more heat accumulation, hence increasing the peak temperature and cooling time, and lowering the cooling rates. The weaving patterns also ensured that there were no lack-of-fusion defects with their large coverage of weld penetration, unlike line printing samples which have lack-of-fusion defects present at the weld beads near the side walls. Weaving patterns also have higher deposition rates, due to their continuous printing without having to pause between each weld.

The effect of thermal profiles can be seen in the results of microstructural characterization. Through optical microscopy and EBSD, it can be seen that the grains in the XZ samples of the weaving patterns are more uniformly aligned to the build direction, and even the grains at the sides are less rotated away from the building direction than the ones in the unidirectional and bidirectional samples.

However, aside from grain alignment and shapes of the fusion zones, the microstructure of the weaving patterns samples is similar to line printing samples, also in terms of dendritic structures and δ-ferrite phase fraction. The results in EBSD showed that the measured grain size still has a large standard deviation, due to the grains in the fusion zone boundary region and grains in columnar grain regions with different grain sizes. However, they have a similar grain size distribution, indicating the grains in the same regions between the two samples have similar grain sizes.

Therefore, instead of grain size, the inferior hardness and tensile strength of the weaving patterns should be caused by texture. Observed in XRD and EBSD, weaving patterns have a high degree of grain alignment that causes a strong <1 0 0> texture, due to the preferential growth direction of FCC crystals, and a strong <1 0 0> texture for FCC materials is known to reduce tensile properties [55,60,61], as discussed in Chapter 2.3. On the other hand, XRD showed line printing patterns have more scattered (2 0 0) pole figures, especially for the pole figure of the center of the unidirectional sample, where strong intensities are found at the center and 45º offset of the (2 0 0) pole figure, which indicates a mix of <1 0 0> and <1 1 0> texture. This is also seen in the IPF map in Figure 44. Overall, The tensile properties of the weaving patterns are lower than the samples in most studies, listed in Table 3, only comparable to a study that also used a high laser power of 4000W [45].

In terms of localized differences in hardness, the notable lower hardness values measured in the top layer could be due to the presence of residual stress. Figure 54 shows the effect of residual stress and residual stress ratio κ on percent error in hardness measurement, with the lines indicating the error in measured hardness. The error lines depend on the residual stress state, the ratio between residual stress and ultimate tensile strength, and residual stress ratio κ (defined as the ratio of minor and major residual stress components), leading to different degrees of error in the measured hardness value, either increasing or decreasing the measured hardness [79].

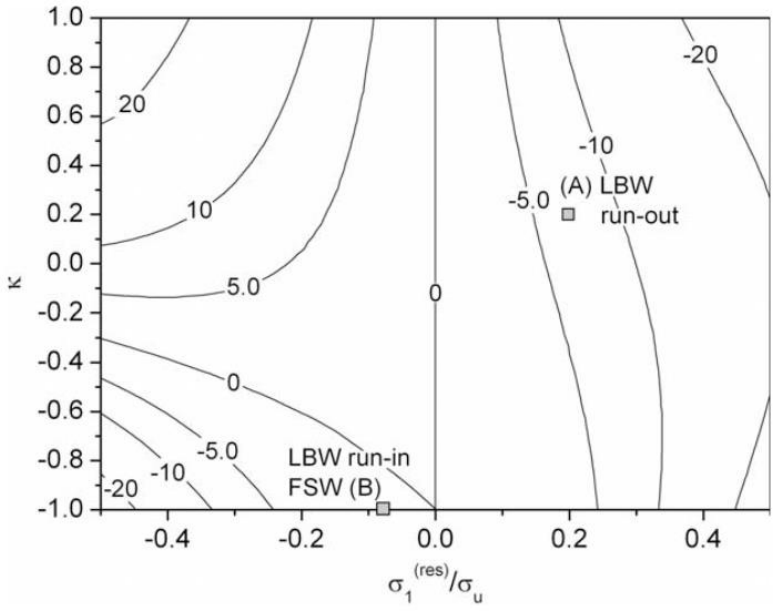

Figure 54 Prediction of percent error in hardness measurement of aluminum alloy welding in relation to residual stress [79].

However, the stress state of weaving patterns is unknown, and according to Figure 54, a reduction in measured hardness can occur with either compressive or tensile residual stress. Because the lower layers have been reheated and their residual stress relieved, there is less residual stress and less reduction in the measured hardness. This could explain why the variation in hardness across layers is not apparent for line printing patterns since they experience a lower degree of heat accumulation and stress relieving. However, the residual stress state can be complicated, and there have been contradicting results even for simpler printing patterns of single-line printing [69,80]. Therefore, further study of the residual stress state of weaving patterns is required.

Aside from inferior mechanical properties, the weaving patterns do offer advantages over line printing patterns. Rectangular weaving and circular weaving both have superior surface quality over the line printing patterns, and they have no lack-of-fusion defects, unlike the line printing patterns. They also offer an increased deposit rate. Because the weaving patterns perform similarly in microstructure and mechanical properties, one weaving pattern can be chosen to be the most stable pattern to be employed. Rectangular weaving has the best surface quality and the least macro-defects out of all the weaving patterns, making it the most applicable out of all weaving patterns.

8 Conclusion

Different weaving printing patterns in WAAM are characterized in terms of microstructure and mechanical properties. The main findings after conducting this study are:

1. Rectangular weaving and circular weaving can achieve improved surface quality and deposition rate when compared to line printing patterns. Through preliminary testing and pattern optimization, a stable printing path without macro-defects can be achieved.
2. The thermal gradients for weaving patterns are reduced, especially in the transverse direction. The weaving patterns also have extended and localized heating, which leads to excessive heat accumulation and a lower cooling rate. The weaving patterns also have higher deposition rates, due to their continuous printing paths.
3. The microstructure of line printing and weaving patterns remains similar, aside from grain alignment and texture. Weaving patterns have stronger grain alignment to the building direction, due to the reduced thermal gradient in the transverse direction. This also strengthens their <1 0 0> texture in the same direction of grain elongation.
4. The strong <1 0 0> texture of the weaving pattern samples led to inferior mechanical properties in terms of tensile strength, ultimate tensile strength, and microhardness when compared to the line printing patterns, which have a mixture of <1 0 0> and <1 1 0> texture. The weaving patterns have similar ductility to the line printing patterns.

9 Future research

Firstly, it could be useful to study weaving patterns with a similar methodology presented in this thesis, but with a lower heat input. The thermal gradient of weaving patterns for a lower heat input would be less homogeneous, due to less heat accumulation, and the effect of thermal profile on microstructure would be more apparent. Lower heat input also leads to thinner weld beads, which means the printing path would be altered. Printing a thick-walled WAAM block would require the pattern to have a more transverse printing path, further differentiating the thermal profile from the high heat input weaving patterns studied in this thesis.

Secondly, EBSD scans are by far superior to optical microscopy, providing far more information while being more reliable, without having issues with inconsistencies in color etching. A more extensive EBSD scans on all the printing patterns covering more layers, as well as on all cross sections would provide a more comprehensive view of microstructural evolution, grain morphology, and texture. This would also benefit from a lower heat input and narrower WAAM blocks, with smaller areas containing more grains to be efficiently examined.

This thesis also limited its scope to the equilibrium of the weld by only examining the top layers and neglecting any change throughout the layers. It would be useful to investigate the microstructural evolution throughout the layers from the substrate to the top, to examine the influence of the substrate in weaving, especially in terms of grain size and dendritic structure. The dendritic structure of the samples was also not thoroughly examined, and it could provide additional information.

Finally, fracture, fatigue, and creep behavior of the weaving samples were not investigated due to the scope of this thesis and should be studied. A combination of differences in grain size, grain alignment, yield strength, and fusion zone boundary shapes could potentially cause different behavior in fracture, fatigue, and creep behavior.

10 References

1. Herzog, D., Seyda, V., Wycisk, E., & Emmelmann, C. (2016). Additive manufacturing of metals. *Acta Materialia*, *117*, 371–392. https://doi.org/10.1016/j.actamat.2016.07.019

2. Sames, W. J., List, F. A., Pannala, S., Dehoff, R. R., & Babu, S. S. (2016). The metallurgy and processing science of metal additive manufacturing. *International Materials Reviews*, *61*(5), 315–360. https://doi.org/10.1080/09506608.2015.1116649

3. IvánTabernero, Paskual, A., Alvarez, P., & Suarez, A. (2018). Study on Arc Welding Processes for High Deposition Rate Additive Manufacturing. *Procedia CIRP*, *68*, 358–362. https://doi.org/10.1016/j.procir.2017.12.095

4. DebRoy, T., Wei, H. L., Zuback, J. S., Mukherjee, T., Elmer, J. W., Milewski, J. O., Beese, A. M., Wilson-Heid, A., De, A., & Zhang, W. (2018). Additive manufacturing of metallic components – Process, structure and properties. *Progress in Materials Science*, *92*, 112–224. https://doi.org/10.1016/j.pmatsci.2017.10.001

5. Rodrigues, T. A., Duarte, V., Miranda, R. M., Santos, T. G., & Oliveira, J. P. (2019). Current status and perspectives on wire and arc additive manufacturing (WAAM). *Materials*, *12*(7). https://doi.org/10.3390/ma12071121

6. Frazier, W. E. (2014). Metal Additive Manufacturing: A Review. *Journal of Materials Engineering and Performance*, *23*(6), 1917–1928. https://doi.org/10.1007/s11665-014-0958-z

7. Williams, S. W., Martina, F., Addison, A. C., Ding, J., Pardal, G., & Colegrove, P. (2016). Wire + Arc Additive Manufacturing. *Materials Science and Technology*, *32*(7), 641–647. https://doi.org/10.1179/1743284715Y.0000000073

8. *WAAM Systems. Quality. Automated*. (n.d.). RAMLAB. Retrieved November 27, 2023, from https://www.ramlab.com/

9. Wu, B., Pan, Z., Ding, D., Cuiuri, D., Li, H., Xu, J., & Norrish, J. (2018). A review of the wire arc additive manufacturing of metals: Properties, defects and quality improvement. *Journal of Manufacturing Processes*, *35*, 127–139. https://doi.org/10.1016/j.jmapro.2018.08.001

10. Li, J. Z., Alkahari, M. R., Rosli, N. A. B., Hasan, R., Sudin, M. N., Ramli, F. R., Faculty of Mechanical Engineering, Universiti Teknikal Malaysia Melaka Hang Tuah Jaya, Durian Tunggal, Melaka 76100, Malaysia, & Center of Advanced Research on Energy, Universiti Teknikal Malaysia Melaka, Melaka, Malaysia. (2019). Review of Wire Arc Additive Manufacturing for 3D Metal Printing. *International Journal of Automation Technology*, *13*(3), 346–353. https://doi.org/10.20965/ijat.2019.p0346

11. Xiong, J., Lei, Y., Chen, H., & Zhang, G. (2017). Fabrication of inclined thin-walled parts in multi-layer single-pass GMAW-based additive manufacturing with flat position deposition. *Journal of Materials Processing Technology*, *240*, 397–403. https://doi.org/10.1016/j.jmatprotec.2016.10.019

12. Ding, J., Colegrove, P., Mehnen, J., Ganguly, S., Sequeira Almeida, P. M., Wang, F., & Williams, S. (2011). Thermo-mechanical analysis of Wire and Arc Additive Layer Manufacturing process on large multi-layer parts. *Computational Materials Science*, *50*(12), 3315–3322. https://doi.org/10.1016/j.commatsci.2011.06.023

13. Ding, D., Pan, Z., Cuiuri, D., & Li, H. (2015). Wire-feed additive manufacturing of metal components: Technologies, developments and future interests. *The International Journal of Advanced Manufacturing Technology*, *81*(1–4), 465–481. https://doi.org/10.1007/s00170-015-7077-3

14. Dickens, P. M., Pridham, M. S., Cobb, R. C., Gibson, I., & Dixon, G. (1992). *Rapid Prototyping Using 3-D Welding*. http://hdl.handle.net/2152/64409

15. Spencer, J. D., Dickens, P. M., & Wykes, C. M. (1998). Rapid prototyping of metal parts by three-dimensional welding. *Proceedings of the Institution of Mechanical Engineers, Part B: Journal of Engineering Manufacture*, *212*(3), 175–182. https://doi.org/10.1243/0954405981515590

16. Tomar, B., Shiva, S., & Nath, T. (2022). A review on wire arc additive manufacturing: Processing parameters, defects, quality improvement and recent advances. *Materials Today Communications*, *31*, 103739. https://doi.org/10.1016/j.mtcomm.2022.103739

17. Colegrove, P. A., Coules, H. E., Fairman, J., Martina, F., Kashoob, T., Mamash, H., & Cozzolino, L. D. (2013). Microstructure and residual stress improvement in wire and arc additively manufactured parts through high-pressure rolling. *Journal of Materials Processing Technology*, *213*(10), 1782–1791. https://doi.org/10.1016/j.jmatprotec.2013.04.012

18. Gu, J., Ding, J., Williams, S. W., Gu, H., Ma, P., & Zhai, Y. (2016). The effect of inter-layer cold working and post-deposition heat treatment on porosity in additively manufactured aluminum alloys. *Journal of Materials Processing Technology*, *230*, 26–34. https://doi.org/10.1016/j.jmatprotec.2015.11.006

19. *Hot (Solidification) Cracking – Definition, Process and Tests*. (n.d.). Retrieved November 29, 2023, from https://theweldinginstitute.com/Hot-(Solidification)-Cracking-Definition-Process-and-Tests

20. Rodríguez-González, P., Ruiz-Navas, E. M., & Gordo, E. (2023). Wire Arc Additive Manufacturing (WAAM) for Aluminum-Lithium Alloys: A Review. *Materials*, *16*(4), Article 4. https://doi.org/10.3390/ma16041375

21. Shin, S.-J., Hong, S.-H., Jadhav, S., & Kim, D. B. (2023). Detecting balling defects using multisource transfer learning in wire arc additive manufacturing. *Journal of Computational Design and Engineering*, *10*(4), 1423–1442. https://doi.org/10.1093/jcde/qwad067

22. Yuan, L., Pan, Z., Ding, D., He, F., van Duin, S., Li, H., & Li, W. (2020). Investigation of humping phenomenon for the multi-directional robotic wire and arc additive manufacturing. *Robotics and Computer-Integrated Manufacturing*, *63*, 101916. https://doi.org/10.1016/j.rcim.2019.101916

23. Gunenthiram, V., Peyre, P., Schneider, M., Dal, M., Coste, F., & Fabbro, R. (2017). Analysis of laser–melt pool–powder bed interaction during the selective laser melting of a stainless steel. *Journal of Laser Applications*, *29*(2), 022303. https://doi.org/10.2351/1.4983259

24. Bajaj, P., Hariharan, A., Kini, A., Kürnsteiner, P., Raabe, D., & Jägle, E. A. (2020). Steels in additive manufacturing: A review of their microstructure and properties. *Materials Science and Engineering: A*, *772*, 138633. https://doi.org/10.1016/j.msea.2019.138633

25. Ziętala, M., Durejko, T., Polański, M., Kunce, I., Płociński, T., Zieliński, W., Łazińska, M., Stępniowski, W., Czujko, T., Kurzydłowski, K. J., & Bojar, Z. (2016). The microstructure, mechanical properties and corrosion resistance of 316L stainless steel fabricated using laser engineered net shaping. *Materials Science and Engineering: A*, *677*, 1–10. https://doi.org/10.1016/j.msea.2016.09.028

26. Schaeffler, A. L. (1949). Constitution Diagram for Stainless Steel Weld Metal. *Metal Progress*, *56*(11), 680.

27. Kou, S. (2003). *Welding metallurgy* (2nd ed). Wiley-Interscience.

28. Mishra, V., Ayas, C., & Langelaar, M. (2023). Design for material properties of additively manufactured metals using topology optimization. *Materials & Design*, *235*, 112388. https://doi.org/10.1016/j.matdes.2023.112388

29. Park, J., & Lee, S. H. (2021). Cmt-based wire arc additive manufacturing using 316l stainless steel (2): Solidification map of the multilayer deposit. *Metals*, *11*(11). https://doi.org/10.3390/met11111725

30. Yuan, D., Sun, X., Sun, L., Zhang, Z., Guo, C., Wang, J., & Jiang, F. (2021). Improvement of the grain structure and mechanical properties of austenitic stainless steel fabricated by laser and wire additive manufacturing assisted with ultrasonic vibration. *Materials Science and Engineering: A*, *813*, 141177. https://doi.org/10.1016/j.msea.2021.141177

31. Wang, D., Song, C., Yang, Y., & Bai, Y. (2016). Investigation of crystal growth mechanism during selective laser melting and mechanical property characterization of 316L stainless steel parts. *Materials & Design*, *100*, 291–299. https://doi.org/10.1016/j.matdes.2016.03.111

32. Yang, D., Yin, Y., Kan, X., Zhao, Y., Zhao, Z., & Sun, J. (2021). The mechanism of substructure formation and grain growth 316L stainless steel by selective laser melting. *Materials Research Express*, *8*(9). https://doi.org/10.1088/2053-1591/ac21ea

33. Hagenlocher, C., O'Toole, P., Xu, W., Brandt, M., Easton, M., & Molotnikov, A. (2022). The Effect of Heat Accumulation on the Local Grain Structure in Laser-Directed Energy Deposition of Aluminium. *Metals*, *12*(10), Article 10. https://doi.org/10.3390/met12101601

34. Miyata, Y., Okugawa, M., Koizumi, Y., & Nakano, T. (2021). Inverse Columnar-Equiaxed Transition (CET) in 304 and 316L Stainless Steels Melt by Electron Beam for Additive Manufacturing (AM). *Crystals*, *11*(8), Article 8. https://doi.org/10.3390/cryst11080856

35. Palmeira Belotti, L., van Dommelen, J. A. W., Geers, M. G. D., Goulas, C., Ya, W., & Hoefnagels, J. P. M. (2022). Microstructural characterisation of thick-walled wire arc additively manufactured stainless steel. *Journal of Materials Processing Technology*, *299*, 117373. https://doi.org/10.1016/j.jmatprotec.2021.117373

36. Dantzig, J. A., & Rappaz, M. (2016). *Solidification* (2th edition). EPFL Press English Imprint. https://www.epflpress.org/produit/501/9782940222971/solidification

37. Palmeira Belotti, L., Van Nuland, T. F. W., Geers, M. G. D., Hoefnagels, J. P. M., & Van Dommelen, J. A. W. (2023). On the anisotropy of thick-walled wire arc additively

manufactured stainless steel parts. *Materials Science and Engineering: A*, *863*, 144538. https://doi.org/10.1016/j.msea.2022.144538

38. Moradi, M., Hasani, A., Malekshahi Beiranvand, Z., & Ashoori, A. (2020). Additive manufacturing of stellite 6 superalloy by direct laser metal deposition – Part 2: Effects of scanning pattern and laser power reduction in differrent layers. *Optics & Laser Technology*, *131*, 106455. https://doi.org/10.1016/j.optlastec.2020.106455

39. Suryawanshi, J., Prashanth, K. G., & Ramamurty, U. (2017). Mechanical behavior of selective laser melted 316L stainless steel. *Materials Science and Engineering: A*, *696*, 113–121. https://doi.org/10.1016/j.msea.2017.04.058

40. Wang, Y. M., Voisin, T., McKeown, J. T., Ye, J., Calta, N. P., Li, Z., Zeng, Z., Zhang, Y., Chen, W., Roehling, T. T., Ott, R. T., Santala, M. K., Depond, P. J., Matthews, M. J., Hamza, A. V., & Zhu, T. (2018). Additively manufactured hierarchical stainless steels with high strength and ductility. *Nature Materials*, *17*(1), 63–70. https://doi.org/10.1038/NMAT5021

41. Shamsujjoha, Md., Agnew, S. R., Fitz-Gerald, J. M., Moore, W. R., & Newman, T. A. (2018). High Strength and Ductility of Additively Manufactured 316L Stainless Steel Explained. *Metallurgical and Materials Transactions A*, *49*(7), 3011–3027. https://doi.org/10.1007/s11661-018-4607-2

42. Zhong, Y., Liu, L., Wikman, S., Cui, D., & Shen, Z. (2016). Intragranular cellular segregation network structure strengthening 316L stainless steel prepared by selective laser melting. *Journal of Nuclear Materials*, *470*, 170–178. https://doi.org/10.1016/j.jnucmat.2015.12.034

43. Wang, L., Xue, J., & Wang, Q. (2019). Correlation between arc mode, microstructure, and mechanical properties during wire arc additive manufacturing of 316L stainless steel. *Materials Science and Engineering: A*, *751*, 183–190. https://doi.org/10.1016/j.msea.2019.02.078

44. Zuback, J. S., & DebRoy, T. (2018). The Hardness of Additively Manufactured Alloys. *Materials*, *11*(11), Article 11. https://doi.org/10.3390/ma11112070

45. Wang, Z., Palmer, T. A., & Beese, A. M. (2016). Effect of processing parameters on microstructure and tensile properties of austenitic stainless steel 304L made by directed energy deposition additive manufacturing. *Acta Materialia*, *110*, 226–235. https://doi.org/10.1016/j.actamat.2016.03.019

46. Kumar, D., Jhavar, S., Arya, A., Prashanth, K. G., & Suwas, S. (2022). Mechanisms controlling fracture toughness of additively manufactured stainless steel 316L. *International Journal of Fracture*, *235*(1), 61–78. https://doi.org/10.1007/s10704-021-00574-3

47. Blinn, B., Klein, M., Gläßner, C., Smaga, M., Aurich, J. C., & Beck, T. (2018). An Investigation of the Microstructure and Fatigue Behavior of Additively Manufactured AISI 316L Stainless Steel with Regard to the Influence of Heat Treatment. *Metals*, *8*(4), Article 4. https://doi.org/10.3390/met8040220

48. Xiong, L., You, Z. S., Qu, S. D., & Lu, L. (2018). Fracture behavior of heterogeneous nanostructured 316L austenitic stainless steel with nanotwin bundles. *Acta Materialia*, *150*, 130–138. https://doi.org/10.1016/j.actamat.2018.02.065

49. Karthik, G. M., Kim, E. S., Sathiyamoorthi, P., Zargaran, A., Jeong, S. G., Xiong, R., Kang, S. H., Cho, J.-W., & Kim, H. S. (2021). Delayed deformation-induced martensite transformation and enhanced cryogenic tensile properties in laser additive manufactured 316L austenitic stainless steel. *Additive Manufacturing*, *47*, 102314. https://doi.org/10.1016/j.addma.2021.102314

50. Zhang, S. Y., Compagnon, E., Godin, B., & Korsunsky, A. M. (2015). Investigation of Martensite Transformation in 316L Stainless Steel. *Materials Today: Proceedings*, *2*, S251–S260. https://doi.org/10.1016/j.matpr.2015.05.035

51. Grigorescu, A. C., Hilgendorff, P.-M., Zimmermann, M., Fritzen, C.-P., & Christ, H.-J. (2016). Cyclic deformation behavior of austenitic Cr–Ni-steels in the VHCF regime: Part I – Experimental study. *International Journal of Fatigue*, *93*, 250–260. https://doi.org/10.1016/j.ijfatigue.2016.05.005

52. Tapia, G., & Elwany, A. (2014). A Review on Process Monitoring and Control in Metal-Based Additive Manufacturing. *Journal of Manufacturing Science and Engineering*, *136*, 060801. https://doi.org/10.1115/1.4028540

53. Chen, Y., He, Y., Chen, H., Zhang, H., & Chen, S. (2014). Effect of weave frequency and amplitude on temperature field in weaving welding process. *The International Journal of Advanced Manufacturing Technology*, *75*(5–8), 803–813. https://doi.org/10.1007/s00170-014-6157-0

54. Akash, P., Puviyarasan, M., Senthil, T. S., Rathinasuriyan, C., & Sindhiya, S. (2023). Microstructural characterization and mechanical properties of Inconel 625 wall fabricated by GTAW-based WAAM using stringer bead and circular weave pattern. *Engineering Research Express*, *5*(3), 035020. https://doi.org/10.1088/2631-8695/ace58d

55. Gao, L., Bhattacharyya, J., Lin, W., Ren, Z., Chuang, A. C., Shevchenko, P. D., Nikitin, V., Ma, J., Agnew, S. R., & Sun, T. (2023). Tailoring material microstructure and property in wire-laser directed energy deposition through a wiggle deposition strategy. *Additive Manufacturing*, *77*, 103801. https://doi.org/10.1016/j.addma.2023.103801

56. Leicht, A., Yu, C. H., Luzin, V., Klement, U., & Hryha, E. (2020). Effect of scan rotation on the microstructure development and mechanical properties of 316L parts produced by laser powder bed fusion. *Materials Characterization*, *163*, 110309. https://doi.org/10.1016/j.matchar.2020.110309

57. Song, Y., Sun, Q., Guo, K., Wang, X., Liu, J., & Sun, J. (2020). Effect of scanning strategies on the microstructure and mechanical behavior of 316L stainless steel fabricated by selective laser melting. *Materials Science and Engineering: A*, *793*, 139879. https://doi.org/10.1016/j.msea.2020.139879

58. Wang, J., Zhang, J., Liu, G., Liang, L., Yang, G., Huang, A., & Pang, S. (2022). Effects of scanning strategies on residual stress and deformation by high-power direct energy deposition: Island size and laser jump strategy between islands. *Journal of Manufacturing Processes*, *75*, 23–40. https://doi.org/10.1016/j.jmapro.2021.12.054

59. Marlow, F. (2012). *Welding Know-How* (1st ed.). Metal Arts Press. https://www.metalartspress.com/books/welding-know-how

60. Niendorf, T., Leuders, S., Riemer, A., Brenne, F., Tröster, T., Richard, H. A., & Schwarze, D. (2014). Functionally Graded Alloys Obtained by Additive Manufacturing. *Advanced Engineering Materials*, *16*(7), 857–861. https://doi.org/10.1002/adem.201300579

61. Popovich, V. A., Borisov, E. V., Popovich, A. A., Sufiiarov, V. Sh., Masaylo, D. V., & Alzina, L. (2017). Functionally graded Inconel 718 processed by additive manufacturing: Crystallographic texture, anisotropy of microstructure and mechanical properties. *Materials & Design*, *114*, 441–449. https://doi.org/10.1016/j.matdes.2016.10.075

62. Pakkanen, J. A. (2018). *Designing for Additive Manufacturing-Product and Process Driven Design for Metals and Polymers* [PhD Thesis]. Polytechnic University of Turin.

63. Sun, Z., Tan, X., Tor, S. B., & Chua, C. K. (2018). Simultaneously enhanced strength and ductility for 3D-printed stainless steel 316L by selective laser melting. *NPG Asia Materials*, *10*(4), Article 4. https://doi.org/10.1038/s41427-018-0018-5

64. Zhang, X.-Y., Zha, X.-Q., Gao, L.-Q., Hei, P.-H., & Ren, Y.-F. (2021). Influence of Shielding Gas on Microstructure and Properties of GMAW DSS2205 Welded Joints. *Materials*, *14*, 2671. https://doi.org/10.3390/ma14102671

65. Sood, A., Schimmel, J., Ferreira, V. M., Bosman, M., Goulas, C., Popovich, V., & Hermans, M. J. M. (2023). Directed energy deposition of Invar 36 alloy using cold wire pulsed gas tungsten arc welding: Effect of heat input on the microstructure and functional behaviour. *Journal of Materials Research and Technology*, *25*, 6183–6197. https://doi.org/10.1016/j.jmrt.2023.06.280

66. Tan, H., Wang, Y., Wang, G., Zhang, F., Wei, F., Feng, Z., & Lin, X. (2020). Investigation on microstructure and properties of laser solid formed low expansion Invar 36 alloy. *Journal of Materials Research and Technology*, *9*. https://doi.org/10.1016/j.jmrt.2020.03.108

67. *ISO 6892-1:2019 Metallic materials—Tensile testing* (Version 3). (2019). International Organization for Standardization. https://www.iso.org/standard/78322.html

68. Sun, J., Hensel, J., Köhler, M., & Dilger, K. (2021). Residual stress in wire and arc additively manufactured aluminum components. *Journal of Manufacturing Processes*, *65*, 97–111. https://doi.org/10.1016/j.jmapro.2021.02.021

69. Vander Voort, G. (2004). Color Metallography. *Microscopy and Microanalysis*, *10*, 70–71. https://doi.org/10.1017/S1431927604883363

70. Aldalur, E., Veiga, F., Suarez, A., Bilbao, J., & Lamikiz, A. (2020). Analysis of the Wall Geometry with Different Strategies for High Deposition Wire Arc Additive Manufacturing of Mild Steel. *Metals*, *10*, 892. https://doi.org/10.3390/met10070892

71. Blattner, T., Keyrouz, W., Chalfoun, J., Stivalet, B., Brady, M., & Zhou, S. (2014). A Hybrid CPU-GPU System for Stitching Large Scale Optical Microscopy Images. *2014 43rd International Conference on Parallel Processing*, 1–9. https://doi.org/10.1109/ICPP.2014.9

72. Chalfoun, J., Majurski, M., Blattner, T., Bhadriraju, K., Keyrouz, W., Bajcsy, P., & Brady, M. (2017). MIST: Accurate and Scalable Microscopy Image Stitching Tool with Stage Modeling and Error Minimization. *Scientific Reports*, *7*(1), 4988. https://doi.org/10.1038/s41598-017-04567-y

73. de Souza Silva, E. M. F., da Fonseca, G. S., & Ferreira, E. A. (2021). Microstructural and selective dissolution analysis of 316L austenitic stainless steel. *Journal of Materials Research and Technology*, *15*, 4317–4329. https://doi.org/10.1016/j.jmrt.2021.10.009

74. Ghasemi, R., Fazel-Najafabadi, M., & Beidokhti, B. (2018). EFFECT OF DELTA FERRITE ON THE MECHANICAL PROPERTIES OF DISSIMILAR FERRITIC-AUSTENITIC STAINLESS STEEL WELDS. *Archives of Metallurgy and Materials; 2018; Vol. 63; No 1*. https://journals.pan.pl/dlibra/publication/118958/edition/103508

75. Mohammed, G. R., Ishak, M., Aqida, S. N., & Abdulhadi, H. A. (2017). Effects of Heat Input on Microstructure, Corrosion and Mechanical Characteristics of Welded Austenitic and Duplex Stainless Steels: A Review. *Metals*, *7*(2), Article 2. https://doi.org/10.3390/met7020039

76. David, S. A. (1981). Ferrite morphology and variations in ferrite content in austenitic stainless steel welds. *Weld. J. (Miami); (United States)*. https://www.osti.gov/biblio/6599765

77. Huber, N., & Heerens, J. (2008). On the effect of a general residual stress state on indentation and hardness testing. *Acta Materialia*, *56*(20), 6205–6213. https://doi.org/10.1016/j.actamat.2008.08.029

78. Huang, W., Wang, Q., Ma, N., & Kitano, H. (2022). Distribution characteristics of residual stresses in typical wall and pipe components built by wire arc additive manufacturing. *Journal of Manufacturing Processes*, *82*, 434–447. https://doi.org/10.1016/j.jmapro.2022.08.010